Alma Mater Studiorum – Università di Bologna

DOTTORATO DI RICERCA IN

INGEGNERIA ELETTRONICA, TELECOMUNICAZIONI E TECNOLOGIE DELL'INFORMAZIONE

Ciclo XXXI

Settore Concorsuale: 09/E3

Settore Scientifico Disciplinare: ING-INF/01

New Directions in Impedance Spectroscopy for High Accuracy, Augmented Information Extraction and Low Power Implementation

Presentata da: Luciani Giulia

Coordinatore Dottorato

Prof. Alessandra Costanzo

Supervisore

Prof. Marco Tartagni

Co-supervisore

Prof. Aldo Romani

Esame finale anno 2019

To my family and
to Matteo, who fills my life.

Abstract

This thesis provides new directions in the impedance spectroscopy, making it an interesting investigation technique for emerging smart sensors. Modern technologies increasingly require sensors capable of giving accurate measurements extracted among a lot of undesired surrounding information while maintaining low power consumptions.

In this scenario, the main focuses of this thesis are: 1) developing an accurate complex impedance system, 2) extracting the augmented information using multivariate statistical analysis and 3) implementing IS-based systems with low power consumptions. The first project shows the design of a miniaturized, low power and accurate vector analyser for multi-parameter measurements in real-time. It is a versatile platform well-suited to be interfaced with various impedance-based sensors (temperature, conductivity), and it can even be used to monitor the status of a tissue. The vector analyser is based on an accurate application specific integrated circuit, developed by a research group of the University of Bologna, and a digital interface driven by a microcontroller, both placed in a printed circuit board. The digital interface together with the printed circuit board have been designed and manufactured and the vector analyser has been statistically characterized in order to evaluate accuracy and resolution. The validation of the entire system was performing on two real-time biomedical applications.

The second project concerns the combination of powerful statistical methods inside moisture content sensors. The multivariate statistical approaches boost the prediction capability of the sensors exploiting the impedance mismatch between a transmitting and reflecting excitation on a soil. Two probe systems have been manufactured and associated with linear and non-linear models for being tested on three soil types.

The third project shows a low-power implementation of an impedance sensor based on a digital random excitation. The entire system is almost digital, made up by an ultra-low power platform with the aim to become a wearable device. The optimization of the impedance algorithm has been executed on the platform taking into consideration some strategies emerging from the technique chosen and some platform resources.

In future developments, these new investigated directions can be simultaneously applied in the design of IS based sensors which extract the desired information with high accuracy and reduced power budget. The potential of such improved system can be employed in a lot of smart sensors, involving electrochemical, environmental, food, biological applications and wearable devices.

Acknowledgments

First of all, I would like to express my sincere gratitude to prof. Marco Tartagni who introduced me into the world of scientific research. I appreciate the technical and moral support he has given me contributing immensely to my personal and professional growth. I am also thankful for his excellent ability to look to future research trends and for the great confidence in woman engineer, not obvious in electronic field.
It has been an honor to be his first woman PhD student.
I would also to thank my co-supervisor Aldo Romani who strengthens my knowledge in digital domain specially in microcontrollers. I am also grateful for all the academic collaborations during these years specially to Annachiara, prof. Luigi Ragni, prof. Marco Chiani and prof. Luca De Marchi.
A special thanks is due to prof. Luca Benini, he gave me the opportunity to take part in the PULP team at the Eidgenössische Technische Hochschule in Zürich, an amazing experience which encouraged me to focus into embedded systems.
I would also to thank my amazing group in Cesena: Marco for his precious support, my dear friend Cinzia, Pizzo, Davide, Roberta, Manuel, Paolo, Robi and Simo representing an excellent combination of collaboration and friendship.
I would like also to thank all my friends in Civitanova, my friend Nan and all the peoples around me, included Matteo's family.
Special thanks are due to my family for all their love and encouragement.
For my mum, for being there with unconditional love.
For my dad, for his way to encourage me, sometimes non-conventional, but he always did it.
For my brother, for his philosophical attitude in every situation.
And most of all for my true love Matteo. He has brought the happiness into my life and he patiently support me in all my choices.

Thank you.

Giulia

Table of Contents

Introduction

The impedance spectroscopy (IS) is a sensing technique aiming at characterizing a material based on the measurement of the response to a multifrequency excitation. It has a consolidated background since the earliest evidence dates from the mid of the 1890s by W. Nerst [1], when dielectric constant of aqueous electrolytes and organic fluids were measured. In the course of time, the applications substantially increased in the 1980s with the introduction of novel instruments controlled by the digital processing unit, which boosts the computing power, the accuracy of results and reduces the measurement times. Over the years, these requirements became more stringent following the technology trend, persisting to the present days. Modern sensing techniques are implemented in miniaturized sensors, typically powered by a battery and embedded in a sensor network. The potentialities of this new approach are as many as the application fields, from the corrosion monitoring to the human body analysis and even food product or soil assessments. However, when the IS meets modern technologies, it requires an effort to accommodate its standards to the modern architectures guarantying high accuracy of results, while maintaining low-power consumptions. Moreover, real applications are multi-variable systems where we need proper statistical tools with a high level of reliability to infer the information desired. For all these reasons, this thesis investigates new directions for the IS useful in modern sensor design, based on high-accuracy, augmented information extraction and reduced power consumptions.

The present work is divided into four main chapters, related respectively to an overview of the IS and to three projects representing the new directions suggested. Chapter 1 provides the impedance spectroscopy background showing various ways to interpret the "impedance" and a range of applications and techniques to extract it. Chapter 2 suggests how to reach high accurate complex impedances (absolute value and phase) through the development of a miniaturized, low-power vector analyser embedding a microcontroller and an accurate academic application specific integrated circuit (ASIC). The architecture description is associated with a statistical characterization of the accuracy successfully reaching 0.15 % (non-linearity error for absolute value) and 0.07 ° (non-linearity error for the phase) values, while the resolution is estimated at 13.8 bits. The validation of this device is carried out on two biomedical targets. Chapter 3 discusses how powerful statistical methods allow us to obtain an augmented information. The gained advantages are shown for two soil moisture sensors, where the combination with the linear and non-linear tools boosts the prediction capability in three types of soil. Both systems are developed on the comparison between transmitting and reflecting electromagnetic excitations addressed to the soil. The high reliability of the predictive models is supported by optimal coefficients of determination R^2 as high as 0.991 and root mean square errors less than 1% (moisture content expressed as %) as boundary case. Following, Chapter 4 describes how to reduce the power consumptions in implementing an IS-technique into an almost-digital architecture using a pseudo-random binary signal as excitation. This project deeply studies the suitable implementation technique used in an ultra-low power platform in order to obtain a fast measurement with a consumption less than 1 μW.

All these projects are strictly related to each other and they can be considered branches of a same path which is directed to the optimization of the IS into new sensing devices.

Chapter 1: Impedance spectroscopy: applications, fundamentals and thesis goal

1.1 Introduction

The impedance spectroscopy is an indirect method to assess the properties of a device under test (DUT) through the comparison between an excitation and the response produced. The measurement system can be represented as one-port, where the stimulus *x(t)* and the response *y(t)* are two quantities such as voltage and current or electric and magnetic fields. When these two signals are spread in a frequency range, the impedance is a frequency-dependent complex value given by the ratio of the signals obeying to the Ohm's law, as in Fig. 1.

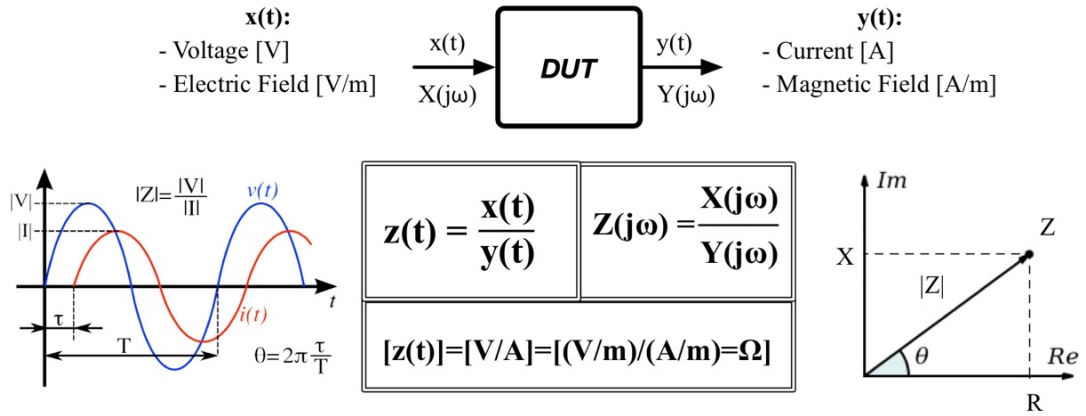

Fig. 1: Impedance representation in time and frequency domains.

The time-dependent impedance is the inverse Fourier transform of the complex spectrum in frequency $Z(j\omega)$ representable in real (R) and imaginary (X) parts or absolute value (|Z|) and phase (θ).

The IS technique has therefore a lot of applications, since any material can be investigated and different properties can be deducted. For these reasons, it perfectly fits in the sensor scenario where, from the beginning, it was integrated in the electrochemistry sensing system such as potentiostat or galvanostat. Both systems investigate reaction mechanisms respectively stimulating, in voltage or current, the electrochemical cell for corrosion studies, development of novel coatings, fuel cells analysis and biotechnology. The corrosion investigation is typically applied to metallic surfaces [2], such as in electrodes analysis or in biological environments to test dental alloys [3] and biodegradable implants [4]. Significant changing on impedance can be monitored also to evaluate the performance of coatings such as for a polymeric film on composite electrodes [5] or, for assessing the quality of paints in industrial processes. For non-biological context, the IS is also employed on the performance evaluation of fuel cells [2] and lithium-ion batteries [6] which cover an important role in electric vehicles as emerging application (smart battery management). In biotechnology, this technique is widely implemented to evaluate microscopic mechanisms, such as DNA damage detection [7],

antibody-antigen recognition [8], detection of bacteria [9] or other specific targets [10]. Anyway, the IS applications really grew substantially thanks to human tissue investigation with non-invasive measurements. In fact, different IS-based instrumentations were developed to capture some information from the skin such as for skin cancer [11], malignant prostatic tissue [12] or breast cancer [13] where the impedance imaging is included in the tomography technique [14]. The further miniaturization of the IS systems and the technology evolutions paved the way for embedding the IS in wearable devices. On the basis of this, the IS exploded in a lot of emerging applications ranging from medical, wellness, sports and many others, as shown in the Fig. 2.

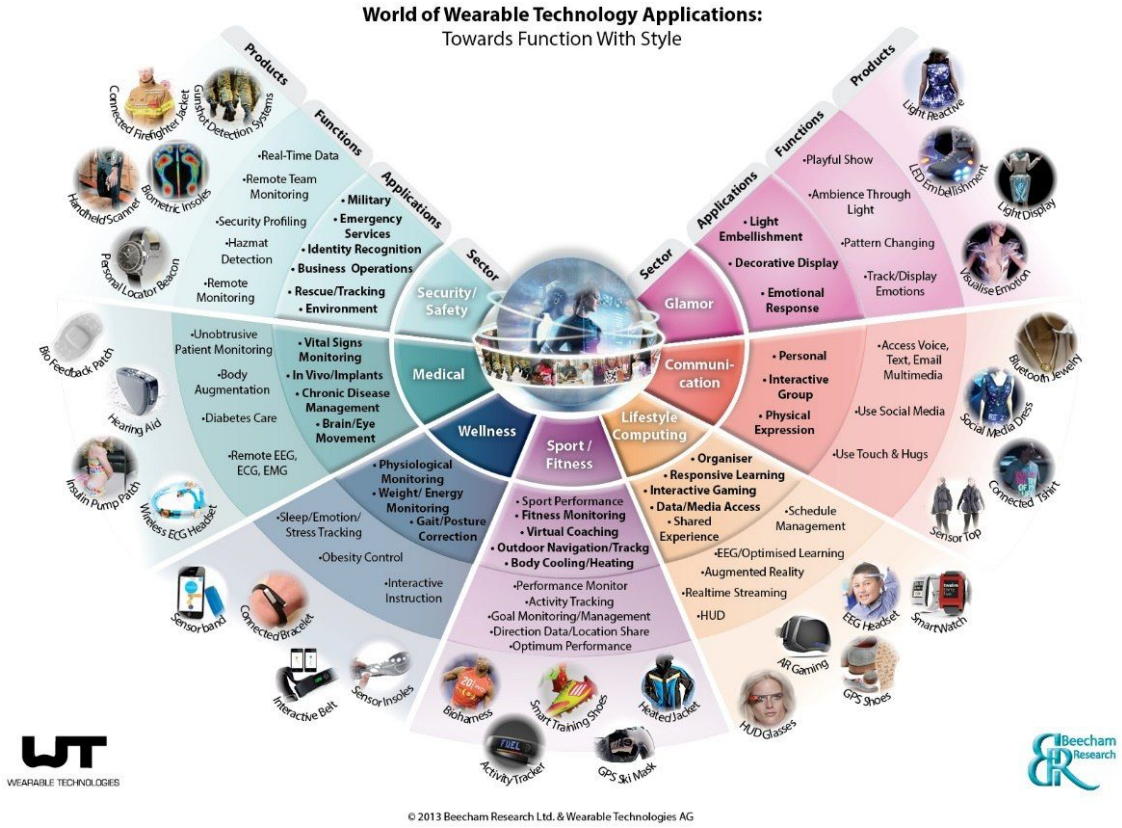

Fig. 2: Wearable technology applications.

The working principle of the IS wearable sensors is to excite the tissue with electrodes , which can be integrated in the measurement system such as a wrist device, headbands, patch, watch or tattoo printed directly on skin (Fig. 4). The theory, underlying these new approaches, refers to the Schwan's study on the electrical properties of a tissue [15]. He recognizes three regions attributed to different tissue constituents in the dielectric spectroscopy. For very low frequencies (<1 kHz), the α-dispersion represents the polarization and ionic effects surrounding the cells; for this reason, this region expresses the resistive capabilities of the extracellular environment. The β-dispersion (up to 100 MHz) returns information about cell shape, intra-cellular environment and capacitive properties of the cell membranes. Finally, the γ-dispersion (>100 MHz) is the responsible of the relaxation of water molecules.

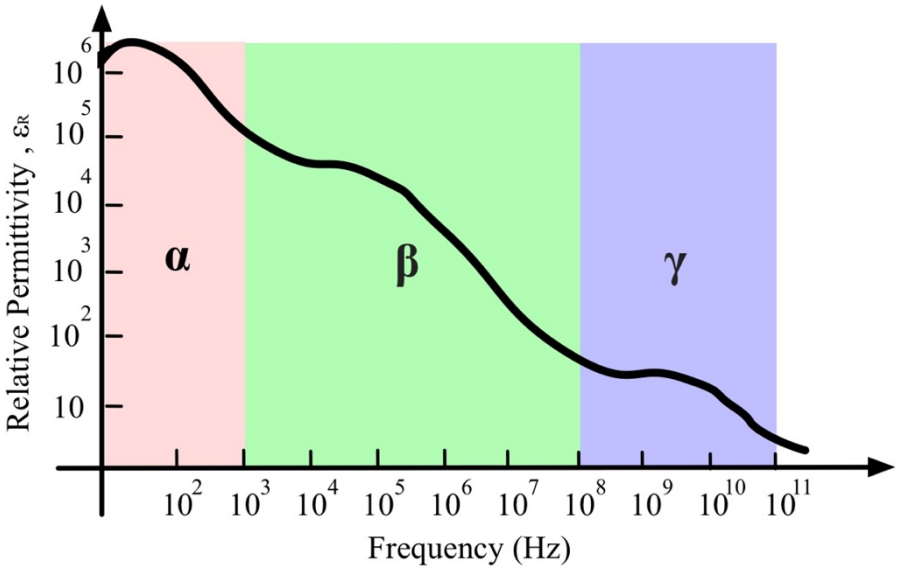

Fig. 3: Dispersion regions for human tissue [15].

On the basis of this study ,the IS technique can be used for monitoring:

- the body human analysis (BIA) [16];
- hydration status of skin [17];
- blood alcohol content [18];
- sweat ions and metabolites [19];
- glucose monitoring [20];
- aortic blood pressure curve [21];
- ulcer pressure in vivo [22];
- general tissue status with implantable devices [23].

Fig. 4: Types of wearable sensors available.

This novel sensor architecture can be classified into the Internet of Things domain (IoT), where sensors are part of a network working for giving the general status of biological systems. However, this concept can be applied in different environments where the IS can be incorporated; for example in liquid monitoring [24], where miniaturized devices can float measuring temperature, conductivity [25], pH [26] and salinity [27]. Also in food assessment, the state-of-the-art refers to novel IS-devices for the detection of plant/food defects, level of ripening [28], characterization of vegetable oil [29], dairy products [30] or salt level in food [31]. Combined with this topic, the IS can be integrated in the precision agriculture for soil moisture assessment [32] or fertilizer sensing. In conclusion, any passive sensors which transduces a physical quantity into a resistive, capacity or such behaviour modelled by an electric circuit can be interfaced with an impedance spectroscopy system.

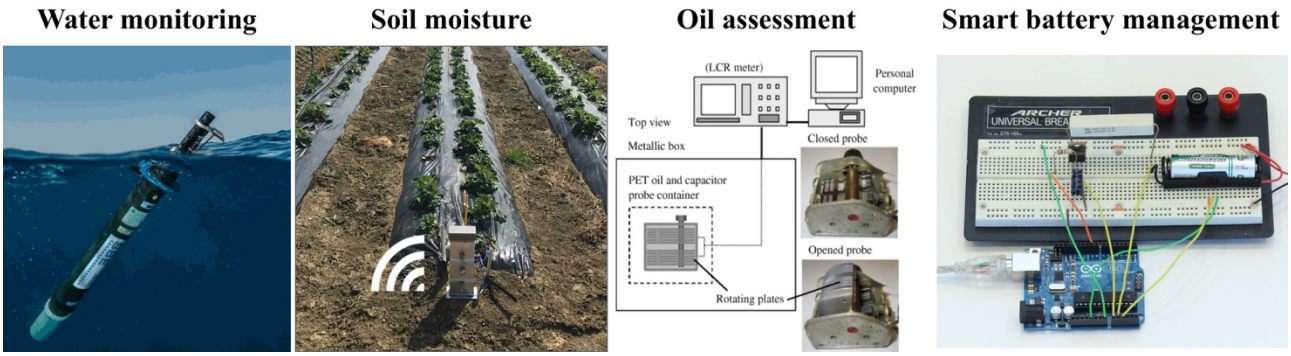

Fig. 5: IS-based systems in IoT applications.

1.2 Origin and meaning of the term "impedance"

The term "impedance" has etymological origins from the Latin verb "impedire", composed by the combination of the proposition "in" and the word "pedis", which means "feet". The significance of the expression "something between feet" refers to an obstacle or to a resistance situation. The extension of this Latin verb into the noun "impedance" is, therefore, associated with the ability to react to this impediment. The first appearance of this noun dates back to 1886 and is due to the British engineer Oliver Heaviside, (inventor of the Heaviside step, known also as Dirac delta) who said:

"Let us call the ratio of the impressed force to the current in a line, when electrostatic induction is ignorable, the Impedance of the line, from the verb impede" (London, "The Electrician" Pub. Co. 1893-1912).

Although Heaviside paved the way for the common impedance meaning, it was Arthur E. Kennelly (1893) who first represented the impedance as a complex number, through the Ohm's law in alternating current circuits as the ratio of voltage and current quantities. This last meaning, associated with electrical circuits, is more properly defined as "electrical impedance". However, this significance can be considered as sub-case of the more general meaning of the term. The impedance, in fact, is intended as the resistance of the material to

a generic excitation regardless of its nature. Therefore, we assume that a material can be also crossed by an energy carrier signal such as an electromagnetic excitation. In the present work, the term “impedance” will be employed with both meanings, corresponding to different discussion mainly about the interaction with the material. When the impedance data are collected in a range of frequency, the impedance term is affiliated with “spectroscopy”. This chapter wants to be an overview about the various aspects involved in the impedance spectroscopy, ranging from the physical interactions to measurement techniques and applications. The state of the art we are going to analyze is necessary to better understand the IS working principle and how this technique can be applied to a modern sensor architecture concept, where devices need to consume low-power since are embedded in wearable or portable devices as previously described. The requirements, imposed by emerging technologies, lead to revisit the classical approaches or introduce new implementation and processing techniques, summarizing the main topic described in this thesis.

1.2.1 Impedance meaning

We previously asserted that the impedance is the opposition of a material to an excitation, regardless of its nature. The common factor of these excitations, however, is the propagation of the stimulus which can be assumed as a wave. This means that also in mechanical context, the impedance of a material can be defined as the measurement of how much the structure resists motion when subjected to a force (32). For instance, if we propagate a mechanical impulse from the beginning of a rope characterized by different densities and joined in an intermediate point as in Fig. 6,

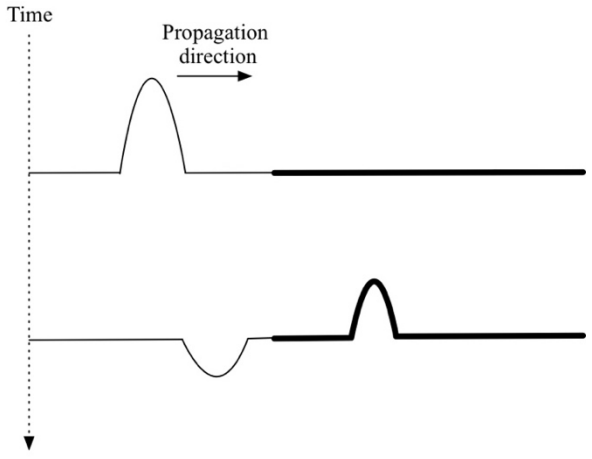

Fig. 6: Propagation of a mechanical impulse along inhomogeneous rope.

the impulse will travel at first with fixed velocity, while after the conjunction it will be partly reflected and partly transmitted. When the excitation is a force, the specific impedance of a portion of the rope is defined as the ratio between the force impressed and the wave velocity as:

$$Z = \frac{F}{v} \tag{1.1}$$

When a harmonic stimulus of amplitude A is applied, the propagating sinusoidal oscillation is a function of the space and time (null phase hypothesis):

$$y(x,t) = A\sin(\omega t - kx) \tag{1.2}$$

where ω is the angular velocity and k is the wave number equals to ω/v, with v velocity of the wave. The external force impressed in a specific point is balanced by the transversal component of the tension with the following formula:

$$F(x,t) = -T\frac{\partial y}{\partial x} \tag{1.3}$$

By calculating the partial derivative and substituting its result in the above equation, the function of the force becomes:

$$F(x,t) = kTA\cos(\omega t - kx) \tag{1.4}$$

On the other hand, with the time derivative of the force we obtain the wave velocity function:

$$v(x,t) = \omega A\cos(\omega t - kx) \tag{1.5}$$

By the ratio between force and voltage functions, we get the impedance as:

$$Z = \frac{F(x,y)}{v(x,y)} = \frac{kT}{\omega} \tag{1.6}$$

It can be shown that the rope density depends on the tension and the wave velocity through the formula:

$$\rho = \frac{T}{c^2} \tag{1.7}$$

Therefore, the mechanical impedance can be expressed as:

$$Z = \frac{T}{c} = \sqrt{\rho T} \tag{1.8}$$

which is a constant value influenced only by the properties of the rope, respectively density and tension. The unit of the obtained mechanical impedance is kg/s or N-s/m.

For the Maxwell analogies, we can translate this mechanical problem into an electric one where the analogies are between the force-voltage and the velocity-current. With respect to the Ohm's law (Fig. 7), the electrical impedance is expressed as:

$$Z = \frac{V}{I} \tag{1.9}$$

where the measurement unit is V/A defined as Ohm (Ω).

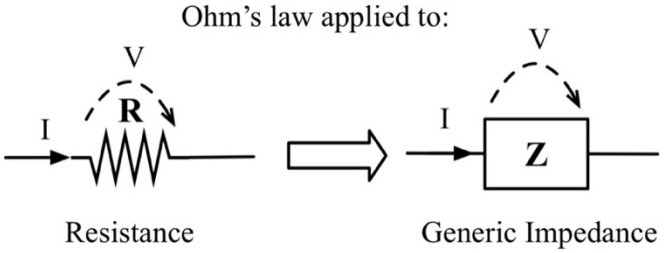

Fig. 7: Ohm's law applied to a resistance and a generic impedance.

From this we can infer that the impedance can be defined also for transmission lines, since the line can be modelled with lumped-element equivalent circuits [33]. The ratio of voltage to current for such travelling waves is defined uniquely by the TEM (transverse electrical and magnetic) mode where the electric and magnetic fields are perpendicular (Fig. 8).

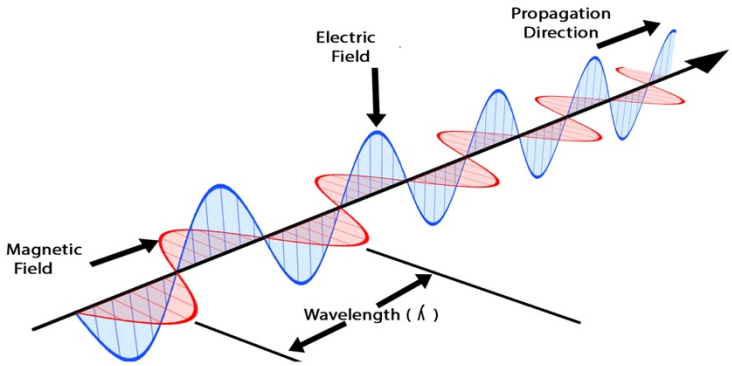

Fig. 8: Electromagnetic wave representation.

Therefore, the characteristic impedance Z_0 of a TEM wave is unique and can be calculated by applying Eq. (1.9). The other modes TE (transverse electric) and TM (transverse magnetic) exist but they not have a uniquely defined voltage and current, so the characteristic impedance for such waves may be defined in different ways [33]. The impedance meaning can be also extended to electromagnetic (EM) signals, where two impedance notations can be used. Considering plane waves, an intrinsic impedance η of a medium can be defined depending only on material parameters permeability μ and permittivity ε as follows:

$$\eta = \sqrt{\frac{\mu}{\varepsilon}} \tag{1.10}$$

On the other hand, an impedance as characteristic of the particular wave TEM, TE and TM can be assumed calculated as the ratio between the electric and magnetic fields. By defining Z_w as the general wave impedance, which can become Z_{TEM}, Z_{TE} and Z_{TM} for the specific mode, it can be expressed as:

$$Z_w = \frac{E}{H} = \left[\frac{V/m}{A/m} = \Omega\right] \tag{1.11}$$

Let us now consider a microwave *N*-port network, shown in the following figure, where equivalent voltages and currents related to incident (V_n^+, I_n^+) and reflected (V_n^-, I_n^-) waves are depicted.

At the *n*th terminal plane, the total voltage and current are given by:

$$\begin{aligned} V_n &= V_n^+ - V_n^- \\ I_n &= I_n^+ - I_n^- \end{aligned} \tag{1.12}$$

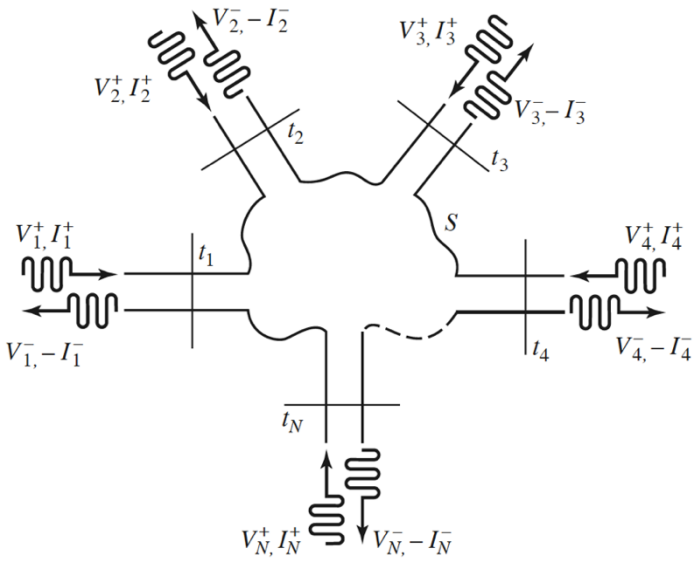

Fig. 9: Electromagnetic waves on the N-port network [33].

The relationship among voltage and current quantities of the above network can be collected using an impedance matrix:

$$\begin{bmatrix} V_1 \\ .. \\ .. \\ V_N \end{bmatrix} = \begin{bmatrix} Z_{11} & Z_{12} & .. & Z_{1N} \\ Z_{21} & & & .. \\ .. & & & .. \\ Z_{N1} & .. & .. & Z_{NN} \end{bmatrix} = \begin{bmatrix} I_1 \\ .. \\ .. \\ I_N \end{bmatrix} \tag{1.13}$$

Where each matrix element is obtained by driving the j port with current I_j and open-circuiting all the other ports:

$$Z_{ij} = \left. \frac{V_i}{I_j} \right|_{I_k=0, k\neq j} \tag{1.14}$$

Similarly to the impedance matrix, the scattering one describes the network in term of incident and reflected waves defined as power quantities. Considering the i_{th} port and assuming a reference impedance Z_0 equal for all ports, the incident power a and the reflected b are:

$$a = \frac{V_i + Z_0 I_i}{2\sqrt{Z_0}} \qquad b = \frac{V_i - Z_0 I_i}{2\sqrt{Z_0}} \tag{1.15}$$

The scattering matrix is related to the above powers as:

$$\begin{bmatrix} b_1 \\ b_2 \\ .. \\ b_n \end{bmatrix} = \begin{bmatrix} S_{11} & S_{12} & .. & S_{1n} \\ S_{21} & & & .. \\ .. & & & .. \\ S_{n1} & .. & .. & S_{nn} \end{bmatrix} \begin{bmatrix} a_1 \\ a_2 \\ .. \\ a_n \end{bmatrix} \tag{1.16}$$

For a 2-port network, the S matrix is 2x2 where the S_{11} and S_{22} are the forward and reverse reflection coefficients while S_{12} and S_{21} are the forward and reverse gains related to the transmission.

1.3 Classification of impedance spectroscopy techniques

Impedance spectroscopy (IS) techniques can be classified on the basis of various parameters involved in the measurement of a material. The five classification criteria, proposed in Fig. 10, include the excitation frequency of the material under test, the corresponding physical interaction, the type of excitation waveform, which is combined with the response analysis, and the applications described before.

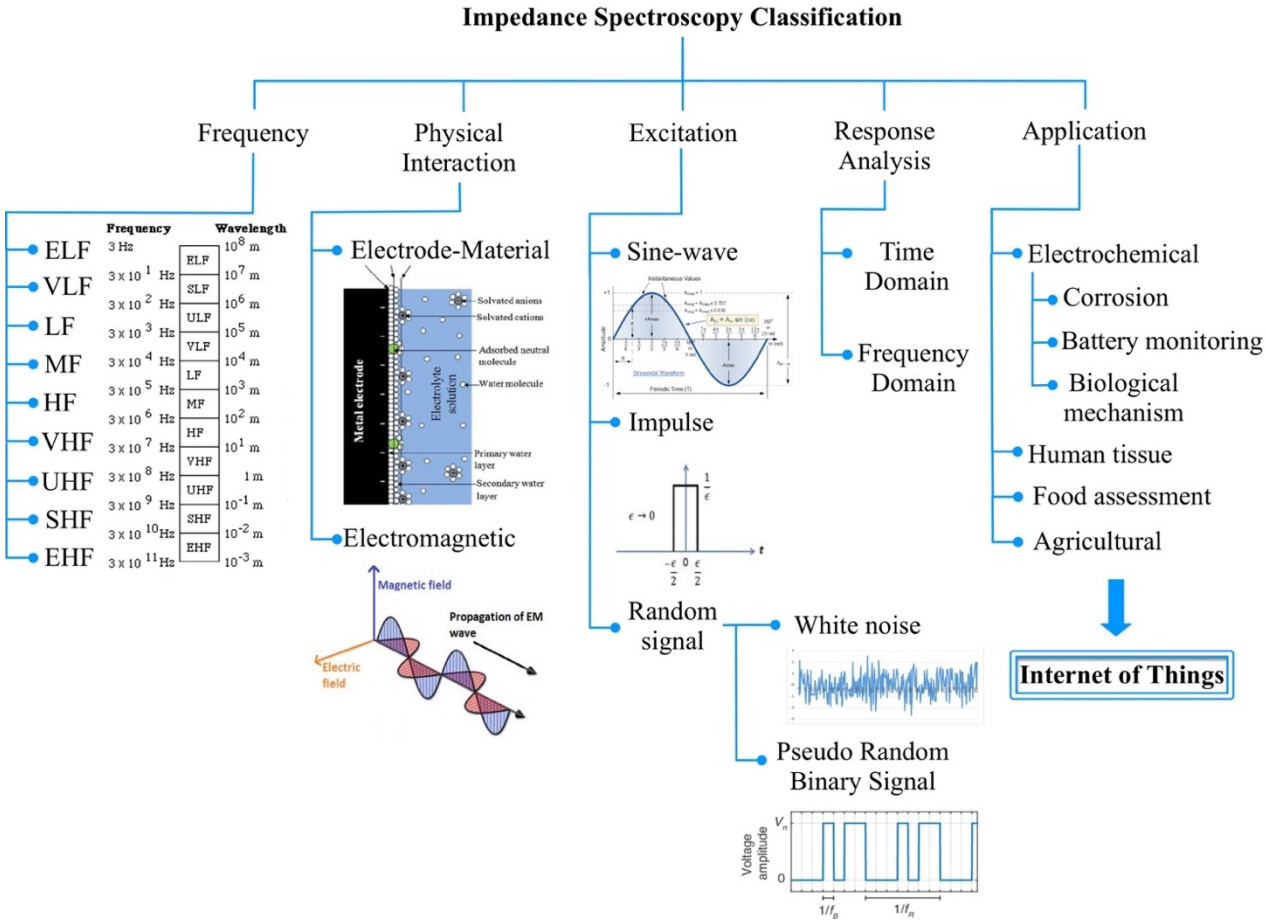

Fig. 10: Classification of the impedance spectroscopy techniques.

Since the IS approach is an indirect method to investigate some physical or chemical features of a material as attested by the application described previously, the device under test should be stimulated with an excitation, or a combination of excitations, covering a range of frequencies. Such range is chosen, in accordance with the electromagnetic spectrum (Fig. 10), depending on what we are investigating and on which material, therefore, the state of the art about the application should be previously considered. The frequency range also influences how we can stimulate the material in term of physical interaction. At lower frequencies, metallic electrodes are

typically used as stimulation and receiving means. In this context, the interface between material and electrode is fundamental to understand how the stimulus (current or voltage) is propagating and the phenomena occurring. On the other side, for high frequencies involved, the excitation can be an electromagnetic wave, which propagates in space-time though an electric and magnetic field (refer to section 1.2.1) through an irradiation by an antenna. Regardless of frequency and type of interaction, the excitation could assume any waveform (sine-wave, impulse, random signal) known by the signal theory, where the mathematical discussion is consolidated. Such stimulus applied also affects the response of the material, which can be investigated in time or frequency. Consequently, the impedance could be represented in both the domains, but commonly used in frequency, where the behaviour is known with the name of impedance spectrum. All the described criteria should be combined to investigate some properties of a material in different applications, such as monitoring electrochemical or biological reactions, evaluating the status of a human tissue, food or soil. The next sections will study in deep the mentioned criteria to depict a complete overview of the impedance spectroscopy.

1.4 Impedance as a model for a physical phenomena

1.4.1 Theory of dielectrics

The physical interactions occurring with a pure electric excitation (transmission with electrodes) or an electromagnetic wave (transmission with an antenna) are used to investigate the electrical properties of a material and infer indirectly, from these, some chemical or physical characteristics.

The electrodes can be defined as conductors used to propagate or receive an electrical stimulus (current or voltage). We assume that the excitation is applied to a material under test, which produces a polarization effect, due to the molecule orientation, and the translation motion of charge carriers by the conductor [34] as in Fig. 11.

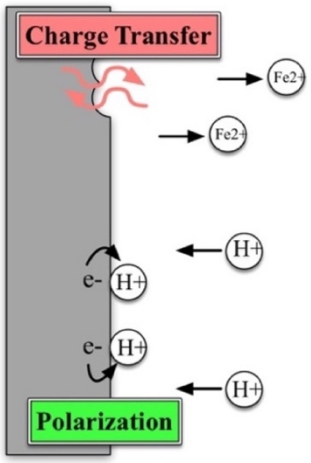

Fig. 11: Polarization and charge transfer effects.

The polarization phenomenon, related to the electrolyte redistribution of charges (dipoles) under an electric field, is described involving the displacement vector D, which is an index of the total charge at the electrodes:

$$D = \varepsilon_0 E + P \tag{1.17}$$

where P is the polarization effect and ε_0 is the permittivity constant in free space. The above equation describes the behaviour of a capacitor with parallel plates, where metallic surfaces are the electrodes and the intermediate region is the vacuum. However, in a real application, the material with relative dielectric constant ε_R should be interposed between plates and a conductance in parallel to the capacitor should be introduced (Fig. 12) to consider also the material conductivity σ_0. Therefore, the polarization vector assumes the form:

$$P = \varepsilon_0(\varepsilon_R - 1)E \tag{1.18}$$

Consequently, the Eq. (1.17) becomes:

$$D = \varepsilon_0 \varepsilon_R E \tag{1.19}$$

By approximating the capacitive behaviour as linear and ignoring fringing field and parasitic effects, the capacitance can be now expressed as a function of the electrode area A and distance d, as follows:

$$C = \frac{\varepsilon_R \varepsilon_0 A}{d} \tag{1.20}$$

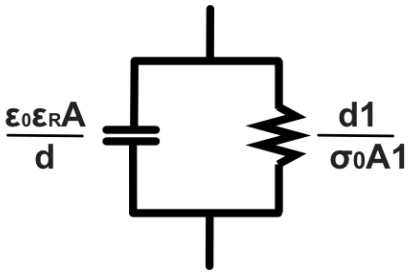

Fig. 12: Circuit model representing polarization and conductive effects of electrodes into a material.

On the other side, the conductive effect is represented by the second Ohm's law with the conductance $G = \sigma_0 A / d$ in parallel to the capacitance (Fig. 12). Therefore, for sinusoidally oscillating fields, the complex admittance of the circuit, in Fig. 12, can be calculated as:

$$Y^* = G + j\omega C = \frac{A}{d}(\sigma_0 + j\omega\varepsilon_0\varepsilon_R) = \frac{A}{d}\sigma^* \tag{1.21}$$

where σ^* is the complex conductivity of the material, while the complex permittivity ε^* is expressed as:

$$\varepsilon^* = \varepsilon_0\varepsilon_R - j\frac{\sigma_0}{\omega} = \varepsilon' - j\varepsilon'' \tag{1.22}$$

The dependence of the complex dielectric constant on the frequency is justified by the material microscopic molecules that react to the polarization with a time constant. This discussion, called dielectric dispersion or relaxation, can be drawn by defining the permittivity at high frequency ε_∞, the static permittivity ε_S at low frequency and the relaxation time of the medium τ. With a first order approximation, the relative dielectric constant can be expressed as:

$$\varepsilon_R = \varepsilon_\infty + \frac{\varepsilon_S - \varepsilon_\infty}{1 + j\omega\tau} \tag{1.23}$$

By substituting the above equation into the Eq.(1.22), the real and imaginary (or dielectric loss) parts can be expressed, with the Debye formulation, as [34]:

$$\varepsilon' = \varepsilon_\infty \varepsilon_0 + \varepsilon_0 \frac{\varepsilon_S - \varepsilon_\infty}{1 + \omega^2\tau^2} \qquad \varepsilon'' = \varepsilon_0 \frac{(\varepsilon_S - \varepsilon_\infty)\omega\tau}{1 + \omega^2\tau^2} \tag{1.24}$$

From the graphic in Fig. 13, representing the real and imaginary parts of the dielectric constant respect to the frequency domain, we can infer that the loss peak, corresponding to the inflection point of the real part, gives information about the relaxation time.

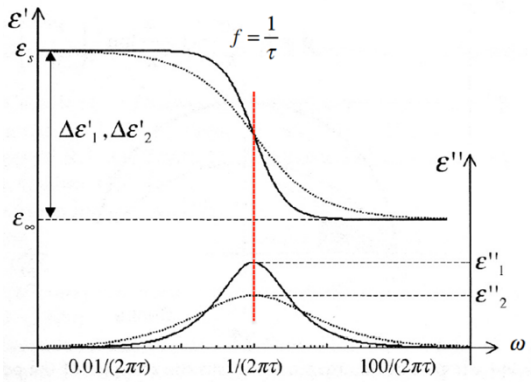

Fig. 13: Real and imaginary parts of two complex dielectric constants in frequency.

Since dielectric behaviours of the most materials are more complicated than a single relaxation model, an extension of the previous discussion involves different relaxation constants due to the response of different microscopic elements (ion, dipole, atom,..) of the material. The combination of these effects is called dielectric spectroscopy and it is shown in Fig. 14. The same spectroscopy behaviour can be also applied to the impedance term. In fact, from the relation of the complex admittance with the complex dielectric constant and reminding that the complex impedance is the inverse of the admittance we obtain:

$$Z^* = \frac{1}{Y^*} = \frac{1}{\frac{A}{d}\omega(j\varepsilon' + \varepsilon'')} \tag{1.25}$$

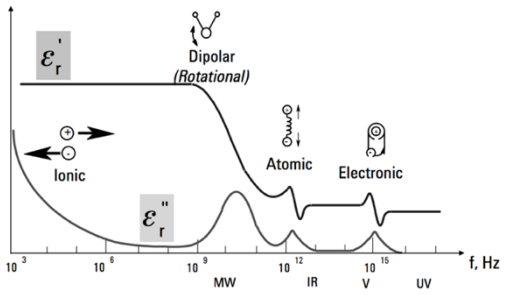

Fig. 14: Dielectric spectroscopy due to different relaxation time constants

The analysis of the complex dielectric permittivity is not in relation with the use of electrodes since it is typical of the material under a general excitation. For this reason, the dielectric behaviour in frequency can be investigated also if the stimulus is an electromagnetic wave generated by an antenna. In this specific case, we should consider that the dielectric properties influence the penetration depths of the electromagnetic energy. According to the Lambert's law, in fact, the power exponentially decreases with the depth of the crossed material as in Fig. 15. The penetration depth, defined as the distance at which the power decreases of a factor 1/e (e=2.718), can be calculated as:

$$d_p = \frac{C}{2\pi f \sqrt{2\varepsilon' \left[\sqrt{1+\left(\frac{\varepsilon''}{\varepsilon'}\right)^2} - 1 \right]}} \tag{1.26}$$

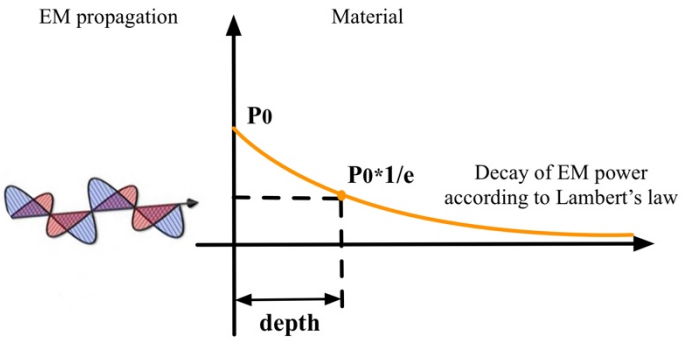

Fig. 15: Depth penetration of an electromagnetic wave into a material.

For the purpose of this thesis, we should take into consideration the previous theory of dielectrics, since different sensors are based on the difference among dielectric constants of the materials. In this way, the frequency excitation is focused on the specific molecules we want to investigate regardless of the application. A typical example is the soil moisture sensors, exciting the water molecules, based on the fact that water dielectric constant is quite different from the other soil constituents and air.

1.4.2 Electrode interface model

We explained how a material reacts to an electrical or electromagnetic excitation. However, the presence of the electrode as a transmission medium requires more details. Let us assume we are investigating the properties of an electrolyte solution, where a metal electrode is plunged into. In this way, a voltage drop occurs between the metal interface and a layer of charges belonging to the electrolyte [35]. This behaviour was first modelled by Helmholtz as a double-layer capacitor C_{DL}, which is combined with a charge transfer faradaic phenomenon due to the reaction occurring at the electrode-electrolyte interface (resistance R_{CT}) (Fig. 16).

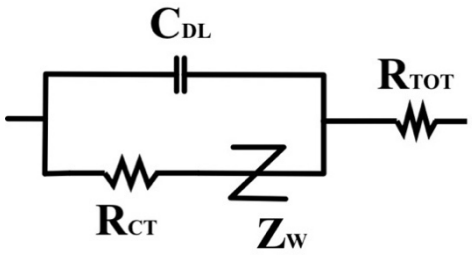

Fig. 16: Equivalent circuit at the interface.

To complete the phenomenon description, we need to consider also another faradic process due to the diffusion represented by the Warburg impedance Z_W as:

$$Z_W = (1-j)\sigma\omega^{-0.5} \tag{1.27}$$

where ω is the angular frequency (s^{-1}) and σ the diffusion constant (Ωs) [35]. Finally, R_{TOT} is the resistance of the solution, which is the desired information. The impedance behaviour of the total circuit model is shown in the following figure, from which some circuital parameters can be inferred.

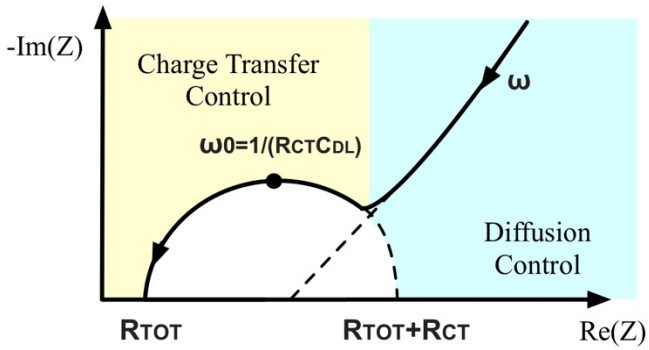

Fig. 17: Impedance behaviour (Real versus Imaginary) at the interface.

2

At very high frequencies, the previous model can be represented as a series of the solution resistance with a constant phase angle impedance (Fig. 18).

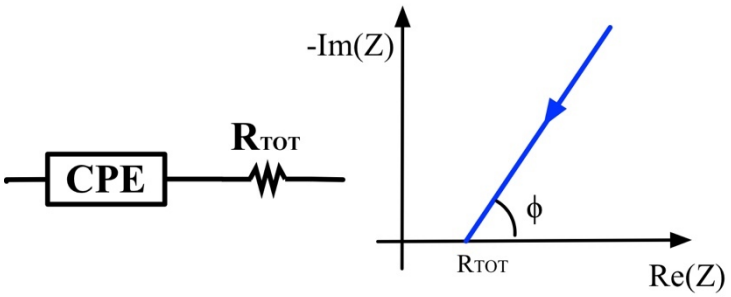

Fig. 18: Model with Constant Phase Angle (CPE) at high frequencies.

In this way, the total impedance at the interface [35] becomes:

$$Z_I = \frac{K}{j\omega^{\beta}} \tag{1.28}$$

where β can be a value between 0 and 1 (typically 0.8 for many biomedical electrodes) and depends on the roughness of the electrode surface. This model should be taken in consideration when an electrode is applied into a material to carefully model the phenomenon and extract only the desired information, which is typically in the solution resistance for sensor application.

1.5 Review of mathematical relationships

As regards the different types of excitation that can be involved in the impedance investigation, they are discussed, in the following sections, in combination with the response analysis. For a specific excitation, we propose the mathematical treatment assuming time-continuous signals, however the discussion can be extended to the discrete-time domain.

1.5.1 The impedance as LTI system

Let us assume a linear time-invariant system (LTI) where $x(t)$ is the excitation signal and $y(t)$ the response as in Fig. 19. Assuming that the system has zero initial energy when the excitation is applied, the output can be expressed only as a function ($F[\cdot]$) of the input $x(t)$ as follows:

$$y(t) = F[x(t)] \tag{1.29}$$

The linearity property of the system guarantees the principle of superposition, therefore if a linear combination of signals is applied:

$$x(t) = \sum_j a_j x_j(t) \tag{1.30}$$

where a_j are constants, the same deduction can be drawn for the output:

$$y(t) = \sum_j a_j F[x_j(t)] \tag{1.31}$$

On the other side, the time invariance means that there are no changes to the system in time and it is expressed as follows:

$$F[x(t-t_d)] = y(t-t_d) \tag{1.32}$$

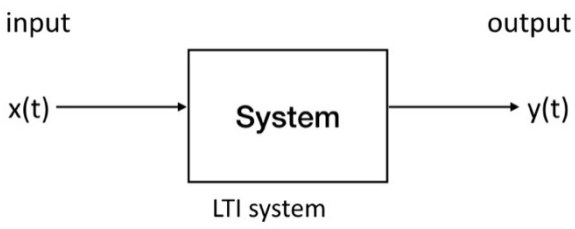

Fig. 19: LTI system representation.

LTI systems are useful to represent circuital behaviours, such as impedance models, where electrical components such as resistance, capacitors or inductors are included. These are called lumped-parameter elements, represented by characteristic equations, and they differ from the spatially distributed phenomena [36]. Introducing these representations for the system elements, the general relation between the input and output assumes this form:

$$b_0\frac{d^n y(t)}{dt^n}+b_1\frac{d^{n-1}y(t)}{dt^{n-1}}+\ldots+b_n y(t)=a_0\frac{d^m x(t)}{dt^m}+a_1\frac{d^{m-1}x(t)}{dt^{m-1}}+\ldots+a_m x(t) \tag{1.33}$$

where differential equations, and related coefficients b_j, a_i ($j=0,\ldots n$ and $i=0,\ldots m$), are involved. This notation is too complex to investigate the direct relation between input and output, for this reason, we introduce the definition of the impulse response $h(t)$ of the system. It is defined as the response when a system is excited by a Dirac-like impulse $\delta(t)$:

$$h(t)=F[\delta(t)] \tag{1.34}$$

The Dirac-like impulse has the property that any continuous signal can be expressed as the convolution between itself and the impulse as follows:

$$x(t)*\delta(t)=x(t) \tag{1.35}$$

Therefore, in continuous domain, the Eq. (1.29) becomes [36]:

$$y(t)=F[\int_{-\infty}^{+\infty}x(\tau)\delta(t-\tau)d\tau]=\int_{-\infty}^{+\infty}x(\tau)F[\delta(t-\tau)]d\tau=\int_{-\infty}^{+\infty}x(\tau)h(t-\tau)d\tau=\int_{-\infty}^{+\infty}x(t-\tau)h(t)d\tau \tag{1.36}$$

The above representation can be summarized using the convolution operation $*$ and simplifying the form into:

$$y(t)=h(t)*x(t) \tag{1.37}$$

If we consider a current excitation as input and the output as a voltage quantity $v(t)$, the above equation is an extension of the Ohm's law where the impulse response coincides with the time-dependent impedance $z(t)$:

$$v(t)=z(t)*i(t) \tag{1.38}$$

By moving in the frequency domain, where the convolution becomes a multiplication, the above equation can be represented as:

$$V(f)=Z(f)I(f) \tag{1.39}$$

where the voltage and current signals in frequency are involved ($V(f), I(f)$) together with the impedance spectrum $Z(f)$. This is a specific case of the more general Fourier transform applied on the Eq. (1.37):

$$Y(f)=H(f)X(f) \tag{1.40}$$

where $X(f)$ and $Y(f)$ are, respectively, the input and output signals in frequency (or spectra) and $H(f)$ is defined as the general transfer function of the system. The analogies between the LTI system parameters and the electrical impedance signals involved are shown in Fig. 20.

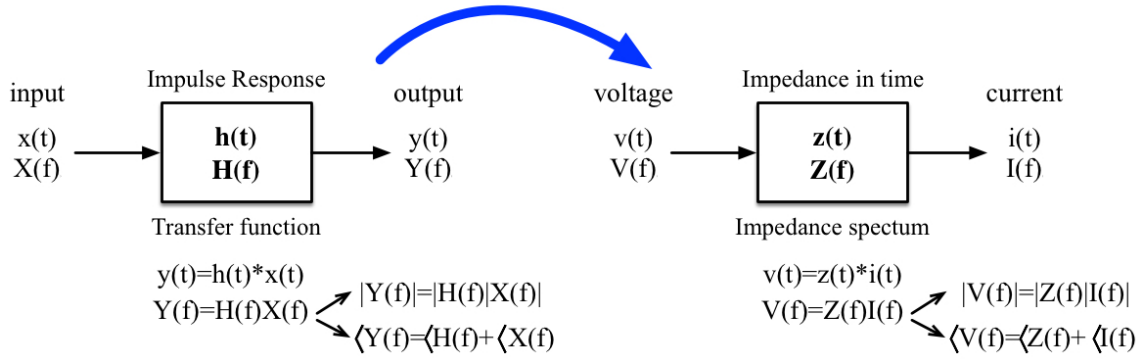

Fig. 20: Analogies between general LTI system parameters and impedance signals.

In the frequency domain all the signals involved are complex values which can be represented by the real and imaginary parts or absolute ($|\ |$ symbol) and phase ($\angle$ symbol) as in Fig. 12. Since $H(f)$ is the Fourier transform of $h(t)$, therefore:

$$H(f) = \int_{-\infty}^{+\infty} h(t) e^{-j2\pi ft}\, dt \tag{1.41}$$

If the time version is real, the transfer function has the Hermitian symmetry [36] expressed as:

$$H(-f) = H^{*}(f) = \begin{cases} |H(-f)| = H(f) \\ \langle H(-f) = -\langle H(f) \end{cases} or \begin{cases} \mathrm{Re}(H(-f)) = \mathrm{Re}(H(f)) \\ \mathrm{Im}(H(-f)) = -\mathrm{Im}(H(f)) \end{cases} \tag{1.42}$$

Imagining to graph the Eq. (1.42), the frequency spectrum of the absolute or magnitude is symmetric, while the phase spectrum is antisymmetric with respect to the origin of the frequency axis.

The previous discussion can be also extended to power quantities. For example, if the excitation is a finite length sequence in the electromagnetic space, an estimation of the resistance offered by the system can be assumed as impedance information. In this new shade of the impedance term, we can consider the power spectral density or energies, respectively, in the following relations [36]:

$$|Y(f)|^2 = |H(f)|^2 |X(f)|^2 \tag{1.43}$$

$$E_y = \int_{-\infty}^{+\infty} |H(f)|^2 |X(f)|^2\, df \tag{1.44}$$

1.5.2 Sine Wave

In support of the above description, we can choose sinusoidal signal $A_x \cos(2\pi f_0 t + \varphi_x)$ as the syem excitation depicted in Fig. 21.

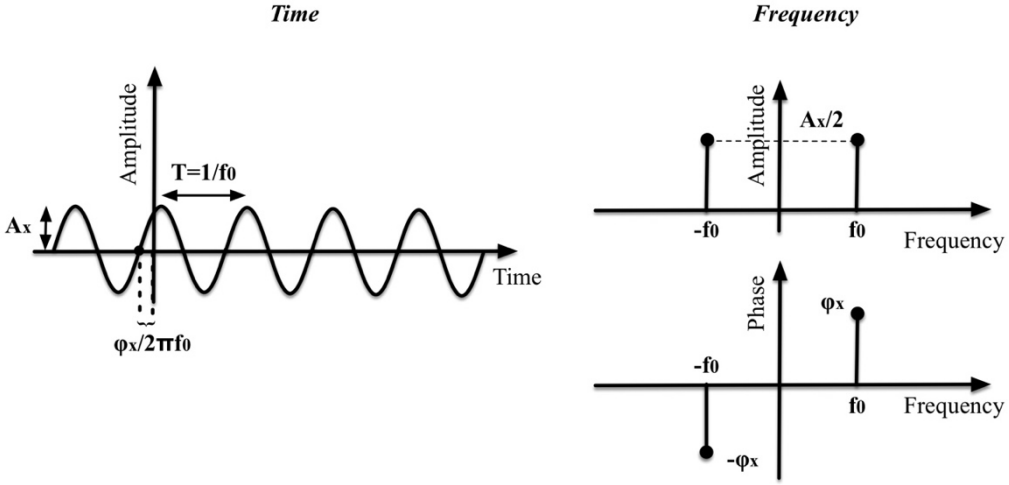

Fig. 21: Representation of a sine wave in time and frequency domain.

Moving into the phasor representation and considering only one side of the spectrum, the input can be described as:

$$x(t) = A_x e^{j\varphi_x} e^{j2\pi ft} \qquad -\infty < t < +\infty \tag{1.45}$$

which corresponds to the following output:

$$y(t) = \int_{-\infty}^{+\infty} h(\tau) A_x e^{j\varphi_x} e^{j2\pi f(t-\tau)}\, d\tau = \left[\int_{-\infty}^{+\infty} h(\tau) e^{j2\pi f\tau}\, d\tau\right] A_x e^{j\varphi_x} e^{j2\pi ft} = H(f) A_x e^{j\varphi_x} e^{j2\pi ft} \tag{1.46}$$

The above equation says that the output can be still expressed as a sinusoidal function with different amplitude and phase shift $A_y \cos(2\pi f_0 t + \varphi_x)$. By comparing the result of Eq. (1.46) with the following polar form of the output:

$$y(t) = A_y e^{j\varphi_y} e^{j2\pi ft} \tag{1.47}$$

it emerges that the relationship between the amplitudes and phase of the two signals are:

$$A_y = |H(f)| A_x \qquad \varphi_y = \langle H(f) + \varphi_x \tag{1.48}$$

This equation explains that applying a sine wave with fixed amplitude and phase, the output is still a sine wave, at the same frequency, but with a displacement in amplitude and a phase shift given by the influence of the transfer function of the system. Therefore, the comparison of signal amplitudes and phases reconstructs the transfer function (or impedance spectrum) information. Such comparison can be entrusted to different known hardware techniques, which make this approach the most used in commercial impedance analysers.
We can note that the spectrum is also collected frequency by frequency (as we can see in the frequency domain of Fig. 21), meaning that the technique for generating the sine wave can be optimized for the specific frequency,

and different sine wave cycles can be applied to improve the signal to noise ratio (SNR). The main drawback of this approach is related to the measurement time, which is proportional to the number and the values of the frequency points involved. It implies that for covering a wide spectrum, specially at low frequencies (time is inversely proportional to the frequency), the system could take a lot of time. This problem should be considered especially when the environment to monitor is subject to rapid changings, therefore the measurement system can fail if it is not fast enough to capture the impedance variations.

1.5.3 Rectangular impulse

The most intuitive approach to investigate the impulse response of a system is to apply an impulse signal in input (Fig. 19) and acquire the output corresponding to $h(t)$ for Eq. (1.35):

$$y(t) = h(t) * x(t) = h(t) * \delta(t) = h(t) \tag{1.49}$$

However, this approach assumes that an ideal Dirac-delta signal is applied, which is almost impossible to perform experimentally, since it has infinite amplitude concentrated in a very short time. To overcome this problem, we can choose to apply a rectangular impulse with finite amplitude (A) and fixed time length τ, represented in Fig. 22.

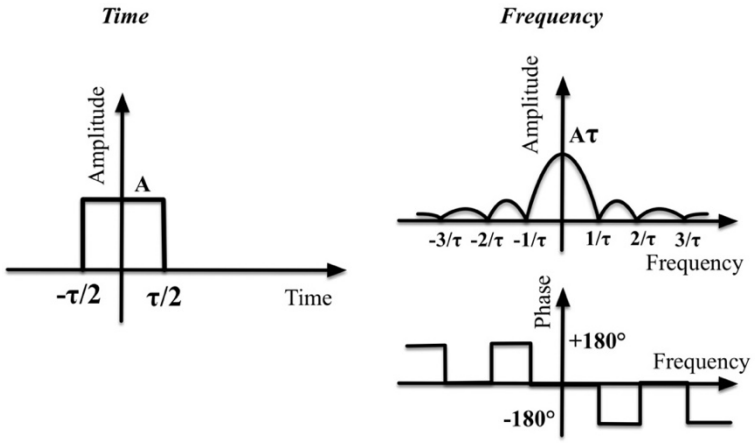

Fig. 22: Representation of a rectangular impulse in time and frequency domain.

Moving for simplicity in the frequency domain, we can express the system output as the product between the transfer function and the Fourier transform of the input. The frequency representation of the rectangular impulse is the following function:

$$X(f) = \frac{A\tau \sin(\pi f \tau)}{\pi f \tau} \tag{1.50}$$

Expanding the above formulation [36], the output is calculated as:

$$Y(f) = H(f)X(f) = \left|H(f)\right| e^{j\langle H(f)} A\tau \frac{sen(\pi f \tau)}{\pi f \tau} = \left|H(f)\right| A \frac{sen(\pi f \tau)}{\pi f} e^{j\langle H(f)} = \left|H'(f)\right| e^{j\langle H(f)} \tag{1.51}$$

Remembering that the Fourier transform of the Dirac impulse in amplitude is the unit ($\left|\mathcal{F}\left(\delta(t)\right)\right|=1$), the above equation can be interpreted as multiplied for the $\left|\mathcal{F}\left(\delta(t)\right)\right|$ [36]. In this way, the response of the system to a rectangular impulse is the response to an ideal Dirac impulse shaped with a different amplitude:

$$Y(f)=\left|H'(f)\right|\mathcal{F}(\delta(t)) \tag{1.52}$$

Although this technique is immediate and efficient, we have to consider that the rectangular impulse should be as short in time as possible and it should collect the necessary energy to excite the system. This implies a suitable wide amplitude of the impulse, which has the disadvantage to force the system to work in a non-linear regime, where the LTI hypothesis collapses. For this reason, the impedance techniques based on rectangular impulse are quite unused.

1.5.4 Random signal

Another interesting approach is to stimulate the system with a wide spectrum involving a random signal. This new approach overcomes the problem related to the measurement time of the classical sine wave, since the excitation of the whole frequency spectrum is performed with a single signal in one shot. To clarify the nature of the random functions, we introduce the stochastic process $\left\{X_t(\zeta)\right\}_{t\in T}\, T\in[a,b]$ as the collection of random variables over an interval $[a,b]$ mapping from the same set of events ζ. Each process is a function both of time t and of the event space ζ. At a fixed time $X_t(\zeta)$ is a random variable, while for a fixed event, $X_t(\zeta)$ is a function of time (random function). One of this function is a realization of the random process and the collections of all realizations is an ensemble (Fig. 23).

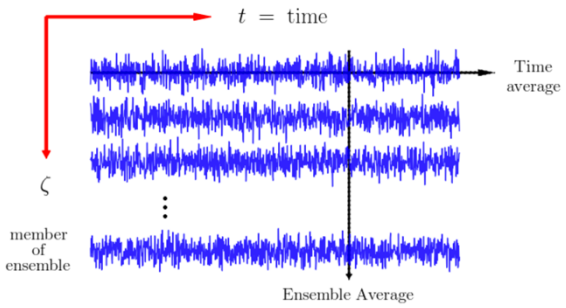

Fig. 23. Representation of random process.

The stochastic process can be characterized using statistical properties such as the average, variance and autocorrelation which can be applied to both parameters producing properties in time or related to the ensembles (Fig. 23) as for the averages properties. In general such averages do not coincide, but when this happens the process is said to be ergodic with stationary statistics. Let us assume a realization $x(t)$ of the ergodic process with mean zero and an autocorrelation function $R_x(\tau)$, the power spectral density of the random function $S(f)$ can be calculated by applying a Fourier Transform. The described statistical properties

can be formulated for any random signal for which we suggest reference [36]. For a specific band-limited white noise (Fig. 24), the power spectral density is:

$$S(f)=\begin{cases}\dfrac{N}{2} & -W<f<W\\ 0 & elsewhere\end{cases} \tag{1.53}$$

while the autocorrelation function is expressed as:

$$R_x(\tau)=\frac{NW\sin(2\pi W\tau)}{2\pi W\tau} \tag{1.54}$$

If the white noise is ideal ($W\to\infty$), with infinite band at constant value, the previous functions are simplified as follows:

$$S_x(f)=\frac{N}{2}\qquad R_x(\tau)=\frac{N}{2}\delta(t) \tag{1.55}$$

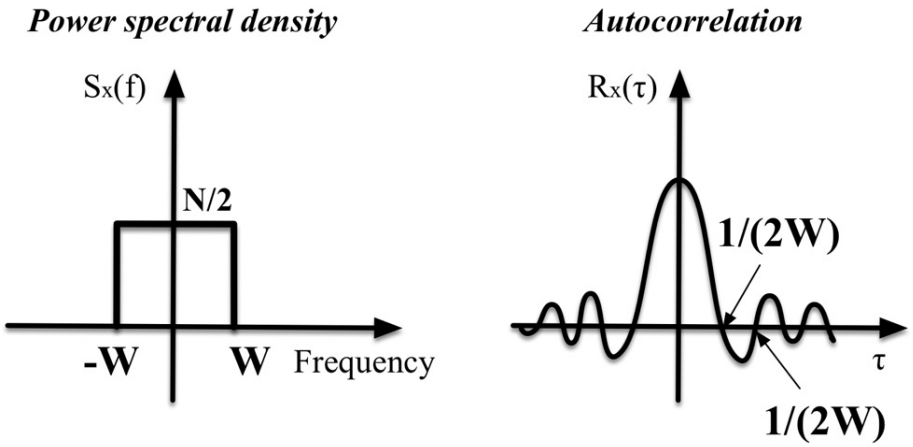

Fig. 24: Band-limited white noise representation.

Let us assume that this random signal is applied to the LTI system, the output $y(t)$ is related to the input through the cross-correlation function:

$$R_{xy}(\tau)=\int_{-\infty}^{+\infty}x(t)y(t+\tau)\,dt \tag{1.56}$$

The relation between the autocorrelation and the cross-correlation depends on the impulse response which can be extracted by a deconvolution:

$$R_{xy}(\tau)=h(-\tau)*R_x(\tau) \tag{1.57}$$

$$R_y(\tau) = h(\tau) * R_{xy}(\tau) \tag{1.58}$$

Focusing in the frequency domain, the above relations are expressed with power spectral densities as:

$$S_{xy}(f) = H^*(f) S_x(f) \tag{1.59}$$

$$S_y(f) = H(f) S_{xy}(f) = |H(f)|^2 S_x(f) \tag{1.60}$$

The ratio between the output cross-spectral density $S_{xy}(f)$ and the $S_x(f)$ gives the complex transfer function or complex impedance when current and voltage are involved. In conclusion, this family of signals can be used to investigate the impedance spectroscopy with the big advantage to stimulate a wide range of frequencies employing a unique signal. Moreover, it is possible to approximate the white noise with a pseudo random binary signal (PRBS) with the additional advantage to work in digital domain where modern hardware and software architectures are easily implementable. A complete discussion about the PRBS is reported in Chapter 4.

1.6 Demand of IS in the internet of things domain

The research of the suitable excitation is related to the architecture of the system we are implementing since some signals allow advantages even in term of hardware design, such as for the cited PRBS easily represented in the digital domain. These novelties paved the way for the Internet-of-Things (IoT) applications. The IoT is an extension of the internet to the things embedding sensors and communicating to each other to return an overview of the environment (agricultural, food, biological). According to this, the Impedance Spectroscopy is a candidate technique to be implemented but it requires new approaches to align with the IoT requirements. In fact, the architecture of the sensors employed should satisfy some strict points. First of all, sensors in IoT are defined as autonomous nodes which collect information, for the application desired, and share results into a sensor network. Regardless of the application, sensor nodes are made up by four parts [37] relative to the sensing, processing unit, the transceiver and the power source (Fig. 25).

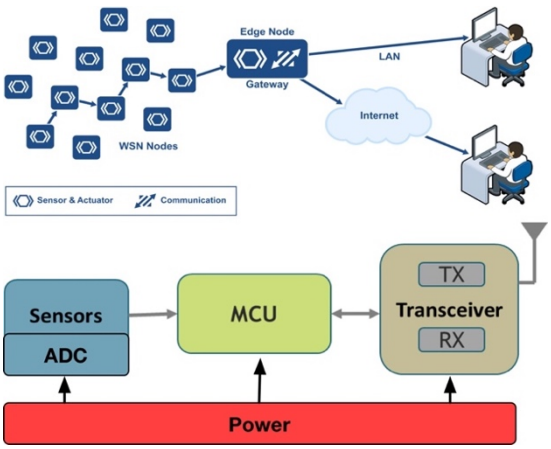

Fig. 25: IoT sensor node architecture.

The sensing part includes the transducer from a physical quantity to another, which will be converted by an analog-to-digital converter (ADC) and fed into the processing unit. Here, raw data are pre-processes by a CPU and stored or transmitted to an transceiver, typically wireless, for connecting the node to the network [37]. One of the most important and crucial component of a sensor node is the power source supported by scavenging unit, like solar cells, or alternative harvesting sources.

As being part of a network, the node must satisfy the following requirements [37]:

- Low power consumption
- High density computing
- Low production cost
- Being autonomous (operating unattended)
- Adaptive to the environment

Such points influence the choice of sensing technique and the implementation, reason why this thesis work proposes new directions for the impedance spectroscopy. The most strict constrains, which lead to new strategies about the technique and the implementation, are the reduced power consumption and the capability of elaborating a huge number of data. These requirements are also linked together, since the elaborating speed and the number of instructions performed by the CPU, due to the algorithm implemented, weight on the overall power budget. This can be divided into the three branches related to the sensing, data processing and communication parts. Among these three domains, more energy is needed in communication compared to the others since it involves a wireless transmission. The consumption of this part depends on the transceiver efficiency and the output power. On the other side, data processing also influences the total power consumption for the architecture of the processing unit chosen (operating frequency, instruction fetching, memory transfers, …) and the algorithm for data processing. Sensor nodes, besides, typically manage a huge amount of data, which further weight on the computational complexity and power budget [37]. For these reasons, ultra-low power microcontrollers are commonly implemented to locally perform a complex elaboration before transmission. Moreover, efficient algorithms should be elaborated to avoid wasting of instructions.

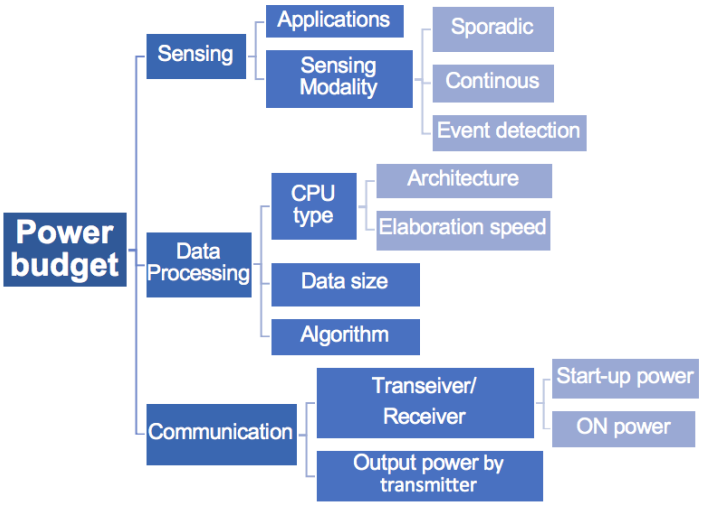

Fig. 26: Parameters influencing the power budget of a sensor node.

1.7 Thesis goal

As widely described in this chapter, the impedance spectroscopy is a consolidated technique involving different physical interactions with the material, types of excitation, impedance analysis and a lot of applications. Focusing on the emerging sensor technology, it seems reasonable to revisit the classical IS measurement systems and to introduce new approaches to follow the evolving needs of this new trend. On the basis of the IS theory previously illustrated, the goal of this thesis is to offer new directions to:

- Reach high accuracy of results.
- Extract augmented impedance information.
- Show new strategies for implementing IS in low-power architecture.

Such points are three directions for boosting the impedance spectroscopy technique in the emerging sensors, therefore, they should not be considered separately but, employable also together, to improve the efficiency and quality of a sensor.

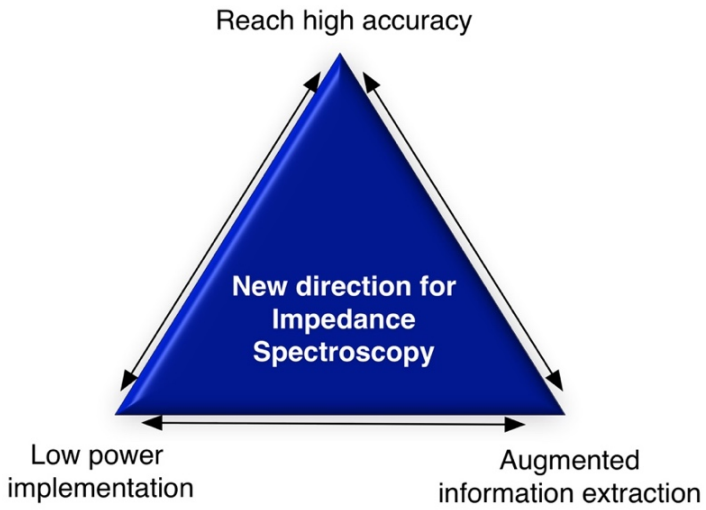

Fig. 27: Research topics.

As regards the personal research activity according to these aspects, three projects are associated as shown in Fig. 28. The first, starts from an integrated circuit ASIC (designed by a research group of the University of Bologna) for impedance sensing based on the classical approach. With regard to this, I worked in developing a miniaturized, low-power impedance analyser, based on ASIC, for environmental and biomedical application where high accuracy is required. In fact, the device developed evidenced accuracy up to 160 ppm. The second project deals with two developed probes, invasive and a non-invasive, for moisture content. The non-invasive approach is based on a waveguide probe (patented by a research group of the University of Bologna), for which I contributed building a vector analyser for soil moisture sensing, with a laboratory set-up first and then implementing a compact device. The same system is applied to the alternative invasive probe.

Both probes are used to predict the moisture content of the soil when powerful statistical linear and non-linear tools are combined. The augmented impedance extraction is, therefore, fundamental to build a predictive

models of both system. The last project has the purpose to implement an optimized IS technique in a low-power architecture, in particular for wearable sensor applications. The optimization relies on the choice of the excitation technique, the impedance algorithm and on the implementation in an ultra-low power platform for which I acquired the right knowledges during the period at the ETH (Eidgenössische Technische Hochschule) in Zurich.

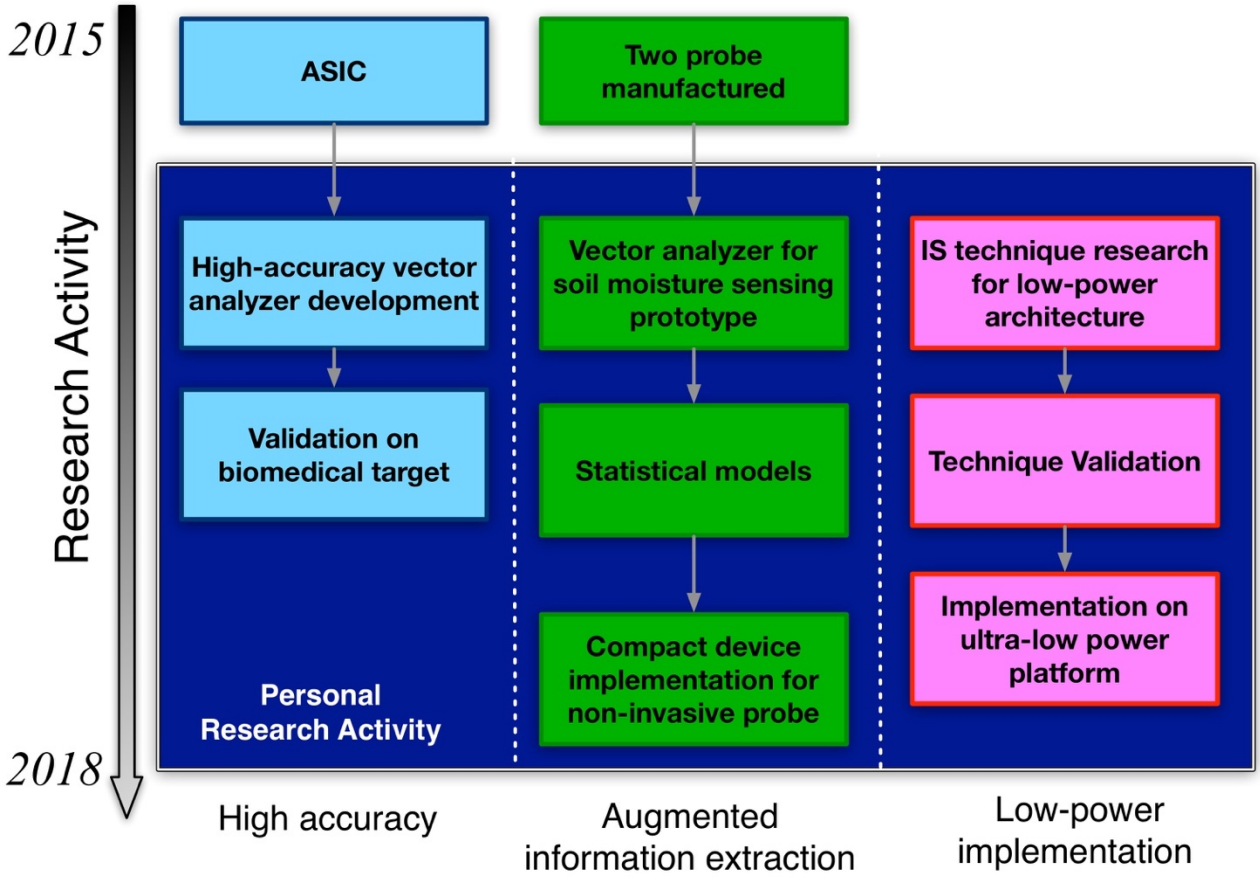

Fig. 28: Personal research activity.

Chapter 2: Miniaturized vector analyser for high-accuracy measurement

Accuracy is of foremost importance in any kind of measurements, IS included. Emerging IS applications in the IoT context, such as wearable or smart devices, require high accuracy together with low-power consumption. Producing very accurate measurements can strengthen the discriminative power of such devices, avoid misunderstanding, while the reduced power consumptions improve the lifetime of the embedded batteries feeding the systems.

As an example of these demands, the current chapter describes a miniaturized, low-power, accurate vector analyser for multi-parameter measurement. The vector analyser extracts the absolute and phase values of a complex impedance by exciting the material under test through a sine wave at fixed frequency. Various architectures can be integrated in the design of such system; among these, the band pass ΔΣ (BPDS) modulation satisfies the high accuracy and reduced power consumption requirements. A BPDS-based application specific integrated circuit (ASIC), designed by a research group of the University of Bologna, is used as analog interface of the developed device. To correctly manage this ASIC, we interfaced a microcontroller (μC) and placed both into a miniaturized PCB (Printed Circuit Board). The obtained prototype, consisting of an analog part driven by the ASIC and a digital one managed by the μC, can be connected to a lot of passive sensors based on impedance variations (temperature, conductivity, tissue monitoring). Since the ASIC has also a multi-core nature, it can be interfaced with even four parallel sensors becoming a small sensor network sharing the same system. Therefore, this project shows a possible solution to reach very accurate impedance acquisitions while consuming low-power when compared to similar devices. This goal is achieved thanks to the chosen architecture of the ASIC and some implementation strategies on the μC tasks. This chapter at first describes the architecture of the vector analyser prototype followed by a statistical characterization for evaluating its accuracy and resolution. Finally, we calibrated and validated the system for two biomedical targets involving the real-time monitoring of a bacterial growth and the tracking of the dynamic of a mechanical heart valve.

2.1 Vector analyser architecture

The developed vector analyser is a combination of two main units: the ASIC and the microcontroller. They cooperate in order to send a current stimulus to a sensor and process the generated voltage drop to return real and imaginary data of the complex impedance under test. The stimulus is a narrowband signal which takes origin from a digitally coded sine wave stored into the ROM of the µC (Fig. 29). Such bit stream (DAC_{IN}) has a limited length of N bits and encodes an integer number M of sine waves. The ratio M/N multiplied for the frequency by which the sine is shot outside the µC (f_{CK}), fixes the excitation frequency of the sensor as follows:

$$f_{IN} = \frac{M}{N} f_{CK} \tag{2.1}$$

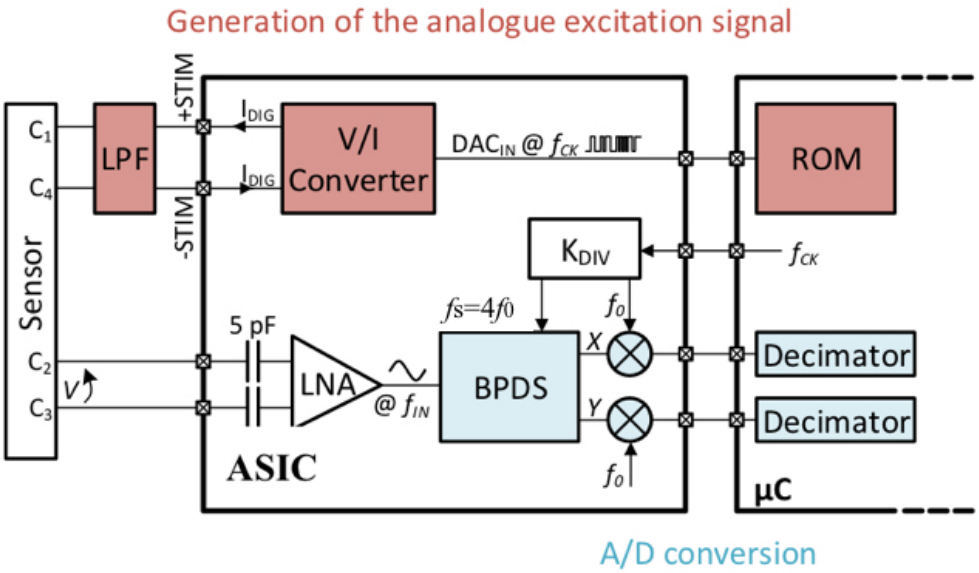

Fig. 29: Block scheme of the vector analyser which includes the ASIC and the µC.

Since the µC generates the sine wave as voltage values, we need a voltage-to-current converter to transform the voltage stream into a current signal (I_{DIG}) maintaining the digital nature. This task is entrusted to a V/I block designed and embedded in the ASIC. The output current I_{DIG} (Fig. 29) is low-pass (LP) filtered with an external LPF for smoothing the sine wave and removing high frequency noise. The excitation is now ready to be interfaced with an impedance-based sensor through a pair of electrodes (C_1, C_4). The ASIC, in fact, arranges a 4-wire Kelvin sensing where two electrodes are associated with the stimulation and C_2 and C_3 to the voltage drop (V). This electrode configuration is preferred for low-impedance measurements.

Since the sensed voltage drop can be very small in amplityde, a programmable low-noise variable amplifier (LNA) is combined on the analog front to magnify signal variations. The LNA is AC coupled to the sensor through two 5pF capacitors producing an input impedance higher than 1 MΩ (for $f_{IN} < 50kHz$) and, therefore, leading to negligible burden voltage. The conversion of the amplified analog signal into the digital

domain is handed over to a band-pass ΔΣ modulator (BPDS), representing the heart of the ASIC, deeply described in [38]. The main blocks of this converter include the BPDS, a quadrature digital mixer and a decimation filter. The underlying principle of the converter is shown in Fig. 30.

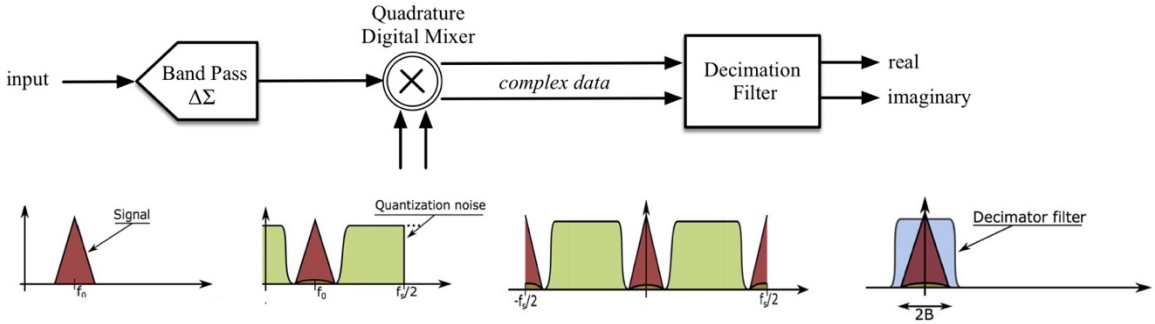

Fig. 30: Bandpass ΔΣ ADC system.

The BPDS oversamples the input signal at frequency $f_s \gg f_0$ and transforms the obtained analog signal into a 1-bit digital stream. As we can appreciate from the lower part of Fig. 30, the output of the converter contains the desired signal surrounded by shaped quantization noise. The nature of the band pass converter, as opposed to a low pass, produces a quantization noise stopband that is centered at f_0 [39]. The digital output of the modulator is then mixed with digital signal at frequency f_0 to down-convert the signal to baseband (2B). Following, the data is decimated and filtered by a digital low-pass filter in order to remove out-of-band signals. From Fig. 30 we can also see that complex components are separated, by sampling the signal twice at $f_s/2$ with a fixed phase lag ($\pi/2$), to set the quadrature, from which real and imaginary parts of the signal will be inferred. This architecture has the advantage to inherently provide full vector information without using noisy and non-linear analogue mixers.

The designed converter is a 4th-order pseudo two-path BPDS chosen for minimizing the chip area and reducing the power consumptions, since less active elements are implemented [38]. The working frequency of the converter is f_0 (Fig. 30) which is synchronized with the f_{CK} through the relation (Fig. 29):

$$f_0 = \frac{f_{CK}}{K_{DIV}} \tag{2.2}$$

where K_{DIV} is a frequency scale factor defined during the ASIC design. To assure high synchronization between excitation signal and BPDS modulation, f_0 is matched to the excitation frequency f_{IN} by setting:

$$K_{DIV} = \frac{N}{M} \tag{2.3}$$

The converter oversamples the signal thorugh the following formulation:

$$f_s = 4 f_0 \tag{2.4}$$

where the oversampling ratio (OSR) is defined as ratio between the BPDS sampling frequency and the signal baseband (2B):

$$OSR = \frac{f_s}{2B} \tag{2.5}$$

The above equation asserts that for $OSR = 1$ we obtain the Nyquist sampling theorem. Typically, the BPDS conversion exploits the bandpass nature of the signal to obtain a high OSR without sampling at very high frequencies, achieving low in-band noise and reduced power consumptions. By de-multiplexing and down-converting the output samples from the BPDS we can observe the two quadrature components which can be codified using a decimator filter, digitally implemented in the μC, and described in the following section.
We can assume that the described architecture of the ASIC in Fig. 29 represents one measurement core. The developed integrated circuit, in 0.35μm CMOS technology, replicates this core obtaining a multi-core platform with 4 identical acquisition systems (Fig. 31) with the V/I, LNA and BPDS blocks sharing two band gap reference voltages (BGR) [38].

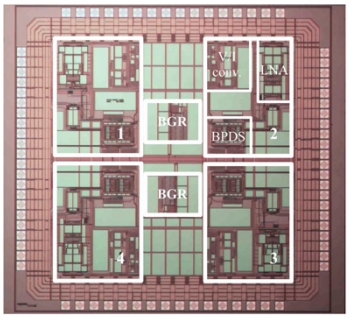

Fig. 31: Microphotograph of the impedance ASIC designed by a research group of the University of Bologna [38].

However, it is possible to clone the architecture for obtaining a desired n number of cores. This will guarantee a vector analyser equipped for multi-parameter measurements representing an innovation in the vector analyser category. This is very interesting when multiple sensors describe the status of a material, for example in water monitoring where temperature, conductivity, pH and others impedance-based sensors can be connected to a unique ASIC. The combination of the ASIC and the μC is implemented in a miniaturized (6 cm × 3 cm) 4-layer PCB self-powered by a USB connection (Fig. 32) which also allows the communication with a PC where the complex impedance can be displayed.

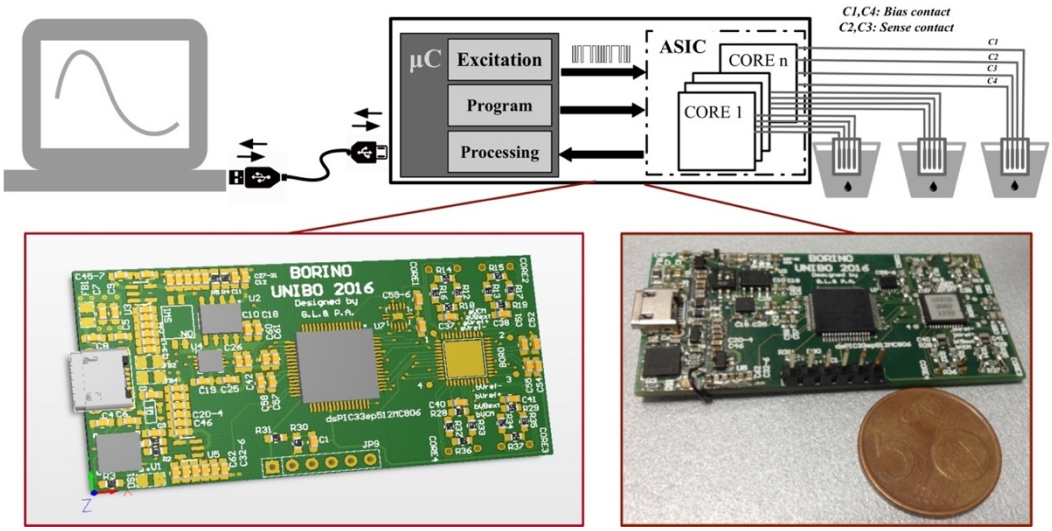

Fig. 32: Miniaturized vector analyser system.

The manufactured device is a very flexible platform since many parameters can be changed such as core activations, current amplitude, LNA gain and BGR voltages. We previously stated (Eq. (2.1)) that the coded sine wave is sent out through a frequency clock depending on the μC. It follows that the stimulating frequency can be tuned up to 45 kHz by properly programming the frequency clock register f_{CK} of the μC. As regards the amplitude of the current stimulus, it can be set among 4 values (10 μA. 150 μA. 300 μA and 1 mA) by a programming configuration to the ASIC. Moreover, for improving the accuracy of the results, the programmable LNA allows the selection of 8 various gain factors (0.5, 1, 2, 5, 10, 20, 50, 100), which should be chosen with reference to the expected impedance.
The developed device shows a total consumption of 500 mW when all cores are switched-on, mainly due to the μC while the ASIC consumes only 5.8 mW. The consumption of the entire device is reasonable when compared to commercial vector analysers that consume more than 1 W with only one or two channels [40] [41] [42]. The miniaturization, the low power consumption and the high accuracy, characterized in the following sections, makes the developed vector analyser a valid competitor among academical and commercial products.

2.1.1 Digital implementation strategies

The digital unit of the vector analyser is implemented through the commercial μC dsPIC33ep512MC806 produced by Microchip. The μC offers the best trade-off between flexibility/power-consumption with respect to other digital platforms (e.g. FPGA). The specific μC is selected since it is fast (working frequency at 70MIPS) and powerful enough to excite the sensor up to 45 kHz and for capturing and processing the external data in real-time. The triple tasks executed by the μC are related to:

- Stimulus generation
- Data sample
- Elaboration

The generation of the stimulus, as previously explained, is calculated offline and stored in the μC ROM for not weighting on the computation budget. However, it needs to be continuously sent during the measurement time and it should be synchronized with the frequency clock f_{CK} provided directly to the ASIC (Fig. 29). To reach this goal without using all the CPU resources, we can exploit the SPI module of the μC with Direct memory Access (DMA), where the serial clock (SCK) matches the f_{CK} and the Serial Data Output (SDO) corresponds to the DAC_{IN} (Fig. 29). The DMA strategy makes the continuous signal generation transparent for the CPU, which can be employed for other processes. With the same approach we can also send a programming stream to the ASIC in order to set the current amplitude, LNA gain and other features. In parallel with this generation, the voltage drop, converted by the BPDS, has to be correctly captured. The ASIC serializes on the same output node the information of the real and imaginary parts of the voltage. The

discrimination between these two components is assured through a synchronization signal (SYNC) by which a real data of OUT can be sampled on the rising edge and the imaginary part on the falling one (Fig. 33).

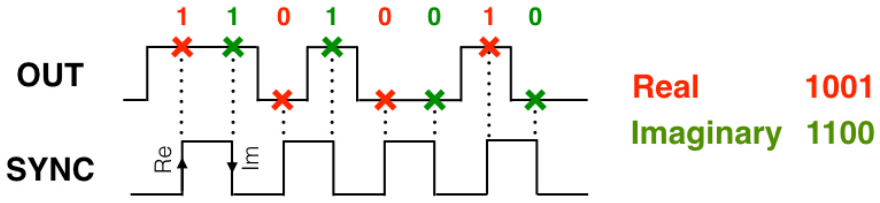

Fig. 33: Extraction of real and imaginary parts of the output based on synchronization signal.

To perform this task, the SYNC signal is attributed to an edge-sensitive interrupt which generates a trigger when a rising or falling edge occurs. The trigger implies that the OUT is read on a digital pin. At this point, real and imaginary values should be elaborated by two decimation filters. A simple solution for implementing this stage is a third order *sinc* filter (SINC^3) made up by a series of three accumulator stages and as many differential stages working at f_S/OSR. By assuming that the real or the imaginary part is the *data*, the filter is implemented with the following algorithm steps, where *data* is either the real or the imaginary part:

Algorithm 1 SINC^3 Filter

1: **input** data
2: **cn$_0$** ←cn$_0$+data,
3: **cn$_1$**←cn$_1$+cn$_0$, **Accumulators**
4: **cn$_2$**←cn$_2$+cn$_1$
5: count←count+1,
6: **if** *count*=*OSR* **do**
7: **cn$_3$**←cn$_2$-cn$_{2d}$,
8: **cn$_4$**←cn$_3$-cn$_{3d}$, **Differentiations**
9: **out**←cn$_4$-cn$_{4d}$,
10: count←0, {cn$_{2d}$, cn$_{3d}$, cn$_{4d}$ are previous data}
11:**else** *go to line 2*
12: **end if**
13: **return out**

Fig. 34: Algorithm description of the SINC^3 filter in pseudo-code.

Finally, the transmission of the filtered data is carried out by the UART module embedded in the μC, which communicates with an FTDI chip (FT232R) for a conversion from UART-to-USB. The real and imaginary parts of the complex voltage drop are then transformed into impedance values by the previous knowledge of the current applied and obeying the Ohm's law. The flow chart, summarizing the tasks executed by the μC for a correct working of the ASIC, is shown in Fig. 35.

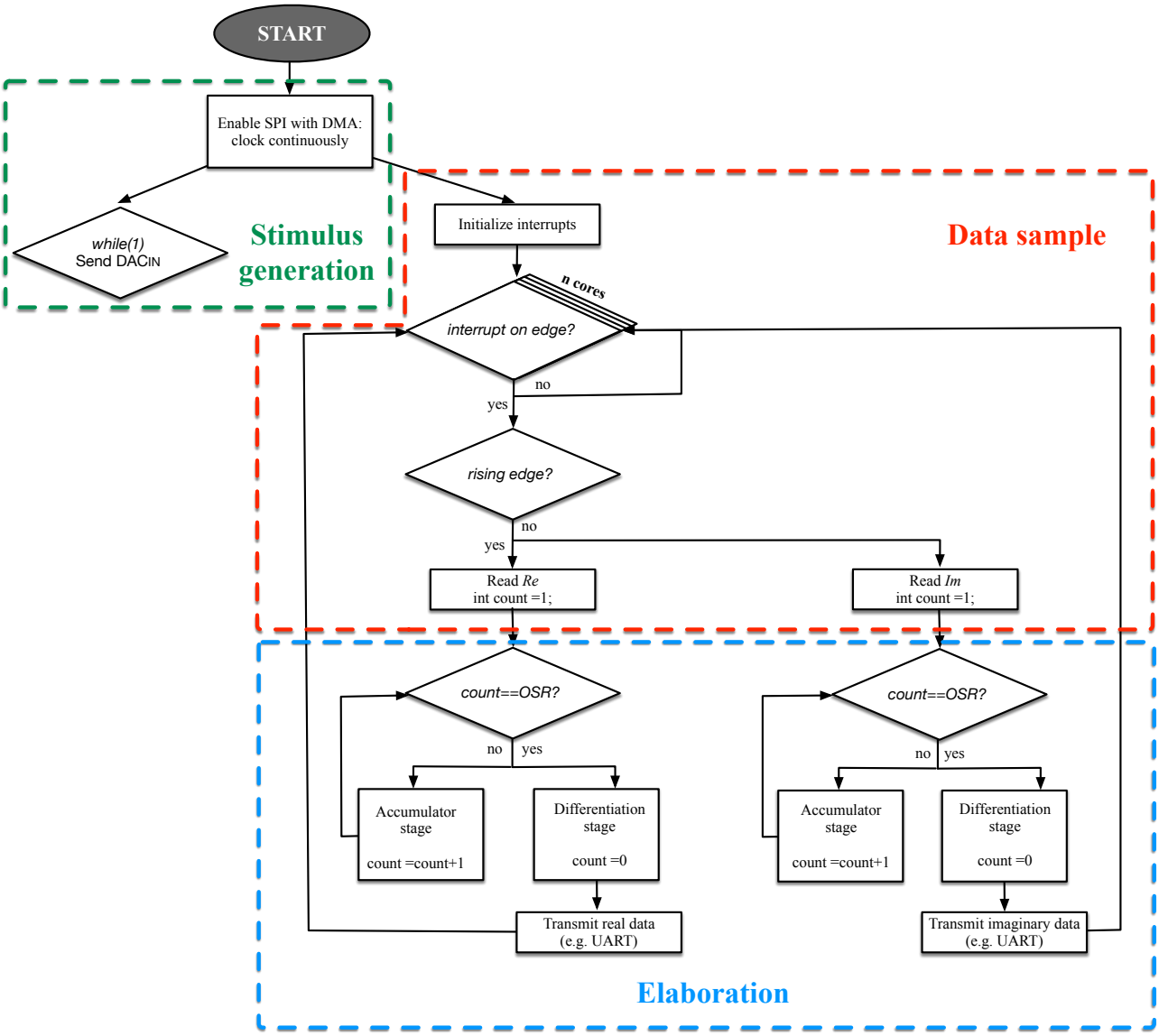

Fig. 35: Flow chart of the algorithm implemented in the μC.

2.2 Device characterization

The performances of the ASIC alone are measured and reported in [38]. The ASIC provides high resolution up to 15.3 bit and an excellent integral non-linearity error (INL) as low as 166 ppm (or 0.0166%). However, such performances reflect only the quality of the ASIC while many other circuital elements are required to develop the complete vector impedance analyser (e.g. the microcontroller), as discussed in the previous section. The general system, described in this chapter, involving also many impedance ranges and excitation frequencies up to 45 kHz, has further sources of noise and non-idealities that affect the global accuracy; thus, a characterization of the entire device is required. The first procedure applied for the evaluation of the accuracy indexes is a device calibration. This is executed under specific conditions of the ASIC, which generates a current stimulus of amplitude 150 μA, sets the LNA gain equal to 5 and performs measurements on the square complex plane bounded by the real and imaginary values ±800Ω. The system calibration is therefore carried out frequency-by-frequency through the impedance evaluation of ten various RC parallel circuits, whose reference values are calculated using an LCR meter E7980A by Agilent (accuracy of 0.3% for magnitude and 0.2° for phase).

The parallel RC samples, assembled with passive components, are chosen so as to cover the complex plane target:

Table 1: Nominal values of the primary parameters of the parallel RC samples used for calibration.

47Ω 47nF	100Ω 47nF	150Ω 47nF	220Ω 47nF	330Ω 47nF	470Ω 47nF	680Ω 47nF	47Ω 1μF	100Ω 470nF	470Ω 470nF

The plot of the reference and measured impedance for the collected samples shows a behaviour which can be described by a smoothing spline interpolation as in Fig. 36.

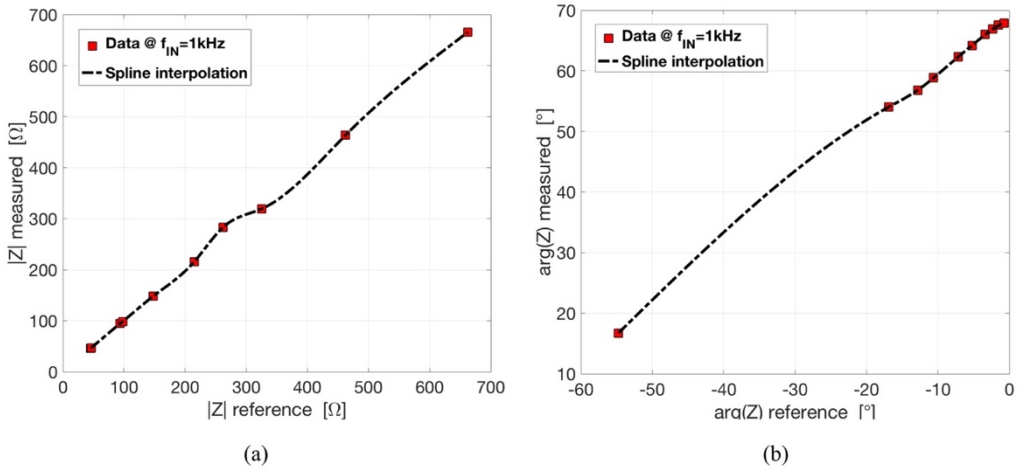

Fig. 36: Vector analyser calibration on absolute (a) and phase (b) at f_{in}=1kHz for ten RC samples.

We note that Fig. 36(b) has negative values for the reference and positive ones for the measured phase. This annotation is justified by the fact that measured phases has a remarkable offset included in the spline interpolation. Such offset is due to the ASIC architecture designed.

The figure also shows that the spline interpolation is the most suitable to calibrate the system. The residuals obtained by this method are depicted in Fig. 37, and they influence the formulation of the root mean square errors (RMSE). Since the RMSEs are calculated for a sample set under fixed frequency excitation, Table 2 collects the errors for various frequency points.

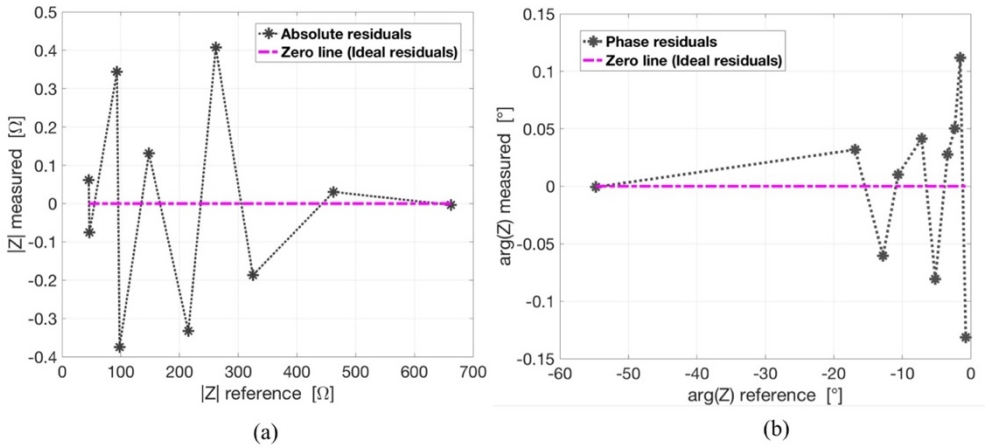

Fig. 37: Residual of absolute (a) and phase (b) obtained by the spline interpolation when the excitation frequency is 1 kHz.

Table 2: Spline interpolation RMS errors relative to absolute and phase

Frequency	1kHz	2 kHz	4 kHz	8 kHz	11 kHz	17 kHz	19 kHz	22 kHz	27 kHz	34 kHz	45 kHz
Absolute value RMSE	0.5797Ω	7.235Ω	3.501Ω	1.852Ω	1.48Ω	1.154Ω	1.431Ω	1.405Ω	1.448Ω	1.676Ω	1.508Ω
Phase RMSE	0.1162°	0.1649°	0.3087°	0.4745°	0.4642°	1.117°	0.6235°	0.6694°	1.918°	4.936°	5.895°

Observing the Table 2, we can appreciate an increasing of the RMSE in phase for high frequencies, although the relation is not perfectly linear. On the other hand, the relation between the RMSE of absolute value and the frequency is not clearly classified.

We must point out that, when calibration is applied under specific conditions, a compensation of the result is significant if the specifications are still the same. Such specifications are not only related to the impedance value and the frequency excitation, but also, as an example, to the chosen LPF. During the characterization of the ASIC in [38], it was demonstrated that the INL value of the ASIC strongly depends on the cut-off frequency of the external LPF filter, whose dependence is shown in the Fig. 38. The same relation is reflected in the evaluation of the accuracy of the entire vector analyser and it should be considered in the system calibration.

Therefore, by assuming a fixed LPF with cut-off frequency of 72.38 kHz, a calibration can be performed at fixed frequency on various samples covering the chosen absolute range and the phase interval [-90°,0°]. The

calibration returns some parameters used to compensate measurement results increasing the accuracy of the system. The compensation applied to the previously described sample set is shown in Fig. 39.
When the calibration is applied, the accuracy of the device should be evaluated on the basis of some parameters which will be described in the following section.

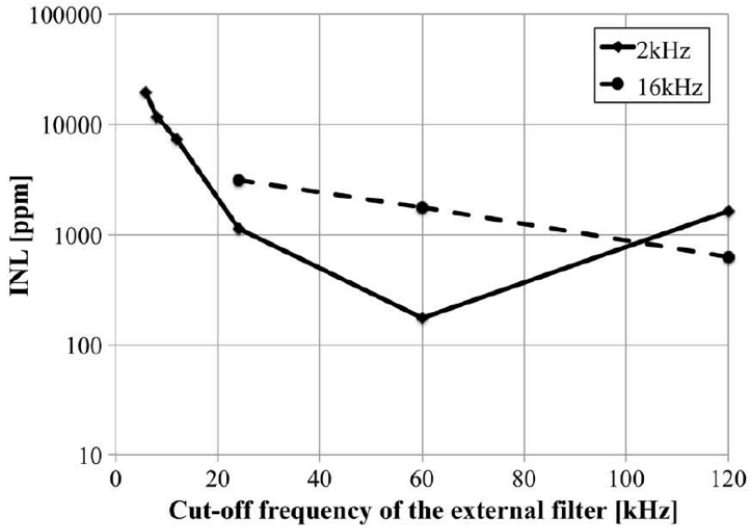

Fig. 38: Dependency of the INL error by the cut-off frequency of the LPF filter.

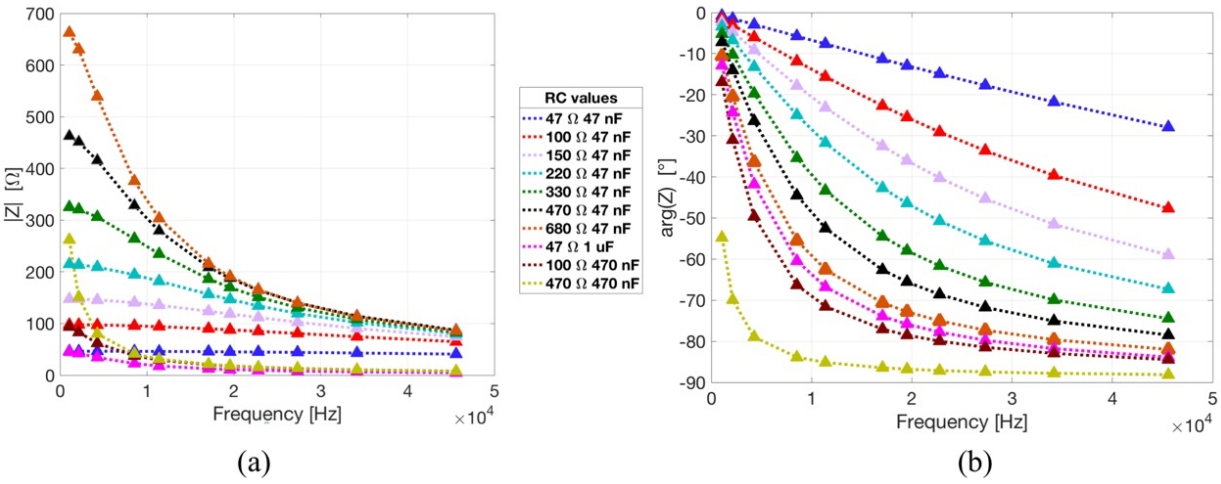

Fig. 39: Calibration result on the vector analyser.

2.2.1 Accuracy and resolution

The first accuracy criterion we are investigating is the non-linearity error. Let us assume that the system is calibrated with the procedure described before. After the calibration, the points related to the reference impedance Z_{ref} and the estimated ones $\hat{Z}$ belong to a straight line representing a data fitting with a 1[th]-order polynomial. We define the impedance points obtained by this interpolation as $Z_{1th-fit}$. We can evaluate the non-linearity errors of absolute and phase values with the following formulations:

$$\%e_{NL-abs} = \left| \frac{|\hat{Z}| - |Z_{1th-fit}|}{|Z_{ref}|} \right| \qquad e_{NL-ph} = \arg(\hat{Z}) - \arg(Z_{1th-fit}) \tag{2.6}$$

Both errors are calculated on the calibrated system with the previous sample set at a specific frequency. In Fig. 40, we show the results obtained for $f_{IN} = 1kHz$.

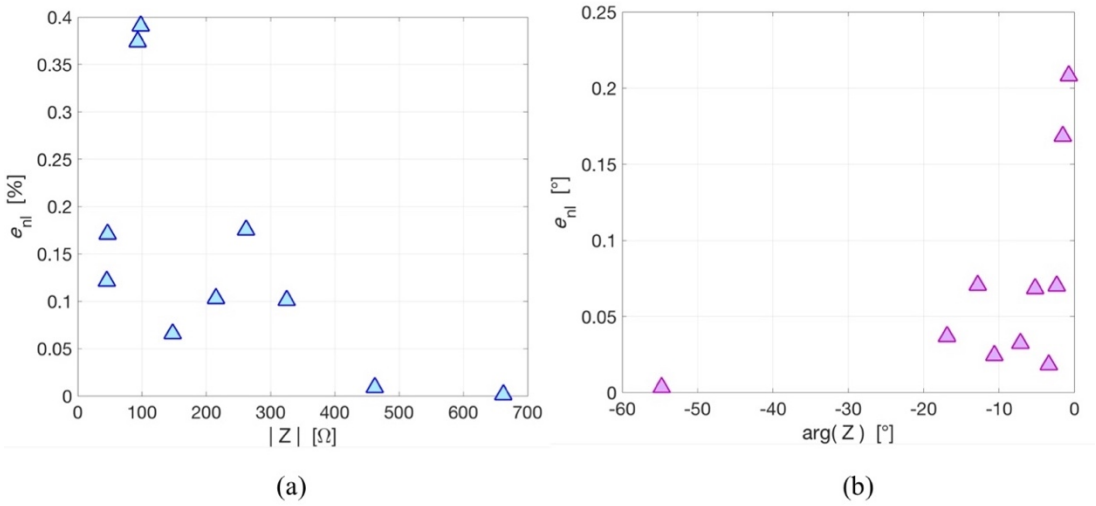

Fig. 40: Non-linearity errors for absolute value in % (a) and phase in degree (b)

From Fig. 40 we can observe that the error of the absolute value decreases when the frequency increases around an average value of 0.15%; while the phase error increases getting closer to zero. Since the non-linearity errors depend on the excitation frequencies, the averages of ten errors, associated with the samples, are calculated and compared to other frequencies in Table 3:

Table 3: Non-linearity errors of the absolute and phase value of the complex impedance.

Frequency	1kHz	2 kHz	4 kHz	8 kHz	11 kHz	17 kHz	19 kHz	22 kHz	27 kHz	34 kHz	45 kHz
$\%e_{NL-abs}$	0.15%	1.07%	1.57%	1%	0.7%	0.76%	1.22%	1.4%	2.49%	3.8%	0.19%
e_{NL-ph}	0.07°	0.09°	0.17°	0.22°	0.22°	0.35°	0.19°	0.17°	0.26°	0.23°	0.3°

Observing Table 3, it emerges that there isn't a fixed behaviour between the errors and the excitation frequencies; however, both are very small in amplitude regardless of the frequency points. We have also to consider that the reference measurements are performed using the LCR meters which has a non-linearity error in absolute of 0.3% and 0.2° in phase. If we compare these values with the ones estimated at 1 kHz, we can deduct that the vector analyser under test could potentially be more accurate than the LCR meter. Therefore, for a correct accuracy evaluation, we should employ a more accurate instrument than the LCR meter chosen. However, the E7980A by Agilent is the best instrument available in laboratory and, moreover, other bench LCR meters have similar non-linearity errors. For these reasons, we can suggest that, for specific frequencies, the vector analyser is more accurate than the LCR by Agilent but, to fully validate this sentence, we should acquire the errors with a more accurate impedance analyser.

A second parameter for judging the accuracy of the developed device is the random noise. We consider that the complex impedance is representable by real and imaginary parts. By assuming the two components collected from different samples, therefore considered uncorrelated, the random noise σ_n can be calculated as the sum of the two quantities as:

$$\sigma_n = \sqrt{\sigma_{n,\mathrm{Re}}^2 + \sigma_{n,\mathrm{Im}}^2} \tag{2.7}$$

In the specific case that the current amplitude is 150μA, the LNA gain is 10, the cut-off frequency of the LPF is 72.38 kHz and the OSR is set every time on the basis of the ratio $f_{in}/2B$, the behaviour of the random noise can be observed as a function of the input impedance by varying f_{in} (Fig. 41). We can deduct that the random noise decreases with the growth of the excitation frequency because f_{in} becomes more similar to the cut-off frequency of the LPF, as assessed before. The distribution of repeated acquisitions for a specific sample is proposed in the zoom (Fig. 41) where the value distribution for the real and imaginary parts are gaussian curves.

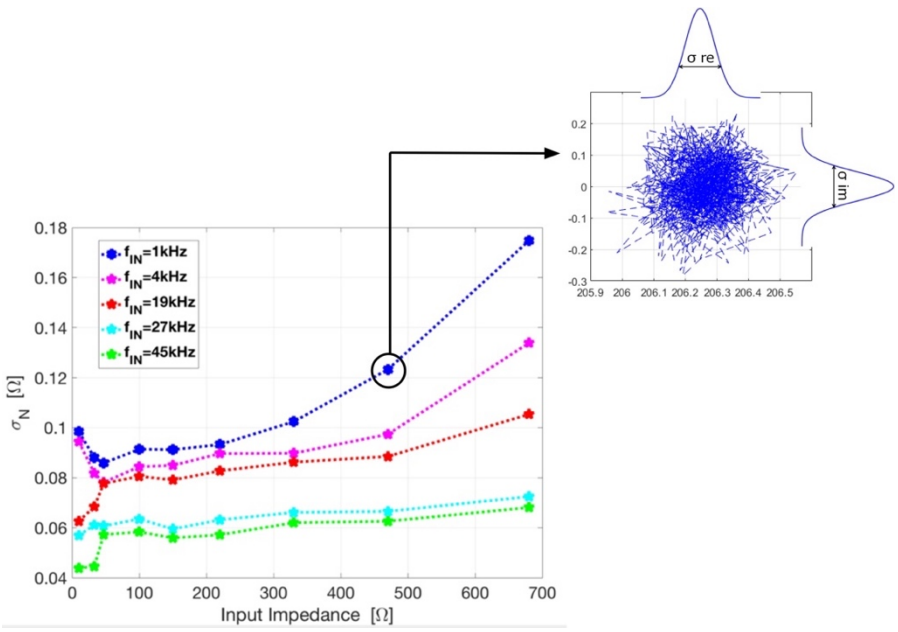

Fig. 41: Random noise associated with the complex measurement.

Another way for characterizing the vector analyser is to evaluate the resolution in bit as for an ADC. To reach this goal we have to assume that the developed device is an ADC receiving impedance data in input. Under this hypothesis, the effective number of bits (ENOB) can be inferred by involving sums of various uncertainties. These are related to: i) quantization (u_q^2), ii) random noise (u_n^2), iii) non-linearity (u_{NL}^2). These all should have also to be considered in the total uncertainty budget as:

$$u_{tot}^2 = u_q^2 + u_n^2 + u_{NL}^2 + u_{offset}^2 + u_{gain}^2 \tag{2.8}$$

On the other hand, an ADC quantization noise can be assumed as a continuous random variable $p(a)$ uniformly distributed between $-q/2$ and $+q/2$ (Fig. 42).

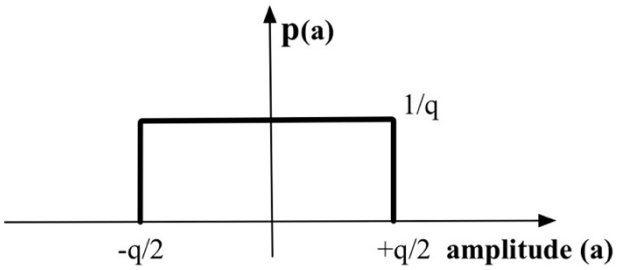

Fig. 42: Total uncertainty distribution uniformly distributed.

By defining the average value of the above variable as μ, the variance or uncertainty can be obtained as:

$$u_{tot}^2 = \int_{-\infty}^{+\infty} (a-\mu)p(a)\,da = \frac{q^2}{12} \tag{2.9}$$

We can highlight that this value, as other uncertainties, can be equally calculated for impedance data or the voltage since they differ for a proportional factor. By choosing voltage quantities, having a full-scale range equal to V_{FS}, the resolution of the impedance analyser depends on the q value as follows:

$$ENOB = \log_2\left(\frac{V_{FS}}{q}\right) \tag{2.10}$$

On the basis of the uncertainties in Table 4, the effective number of bits for the developed impedance analyser is 13.8, which corresponds to 14,263 quantization levels. This is considered a high resolution compared to other impedimetric sensing interfaces which have resolutions typically between 8 and 12 bits [38].

Table 4: Uncertainties associated with the vector analyser.

Frequency	1kHz	2 kHz	4 kHz	8 kHz	11 kHz	17 kHz	19 kHz	22 kHz	27 kHz	34 kHz	45 kHz
u_q	0.0264	0.0264	0.0264	0.0264	0.0264	0.0264	0.0264	0.0264	0.0264	0.0264	0.0264
u_n	0.1054	0.0933	0.0927	0.0929	0.0913	0.0835	0.0812	0.0711	0.0633	0.0589	0.0566
u_{NL}	0.02024	1.4271	1.1938	0.4163	0.2161	0.1788	0.282	0.3476	0.7238	0.8394	0.1466

2.3 Validation

A first validation of the vector analyser developed is performed by depicting the Cole-Cole plot (Fig. 43) of a parallel RC circuit out of the training set used for calibration. The impedance spectroscopy collects data for the frequency points used before.

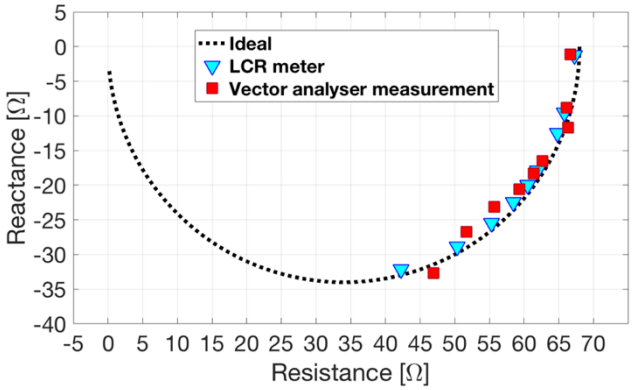

Fig. 43: System validation with a new parallel RC circuit (R=68Ω and C=45nF).

We can appreciate that the behaviour of the impedance of the selected circuit is well reconstructed. By separating the absolute and phase values of the above plot, they can be studied with all the uncertainties which contribute to the ENOB characterization. Moreover, we can introduce also the errors affected by the measurement repeatability, taking also into consideration that the previous tests are not executed at fixed conditions (such as fixed temperature), therefore also the noise of the environment contributes to the measurement. If the purpose is to provide an interval of values with a high level of confidence that the true value is inside that interval, then the expanded uncertainty concept is more suitable; it can be computed as $k \cdot u$, where $k = 2$ approximates the 95% of coverage for a Gaussian distributed random variable. For these reasons, the following absolute and phase plots are associated with the error bars of both measurements and the LCR references.

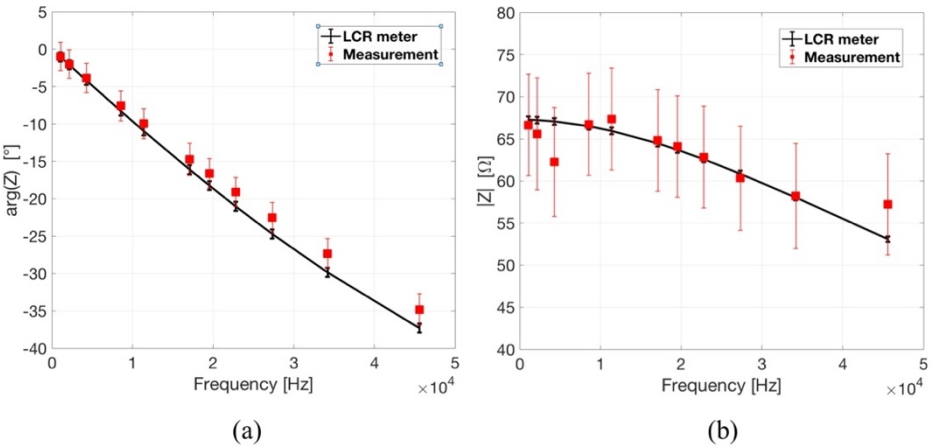

Fig. 44: Absolute and phase in validation with error bars for k=2 (a) and k=3 (b) as coverage factors.

The amplitude of the error bars, compared to the uncertainties described previously (Table 4), are wider because of the uncertainty associated with the measurement repeatability. This decline in the accuracy is caused by the ASIC that uses some voltage references (BGR) that are not stable. In this regard, we are currently working for improving the BGR stability and quality.

However, the fact that the error bars of the measurements, performed with the vector analyser, are crossing the error bar produced by the LCR meter acquisitions means that the calibration is well executed. In the following sections two real applications of the calibrated vector analyser will be proposed, strengthening the importance of the high accuracy and resolution in two biomedical applications for impedance microbiology and for the tracking of the dynamic of a mechanical heart valve.

2.3.1 Impedance microbiology

Food- and water-borne bacterial outbreaks cause diseases and mortality throughout the world. The detection of the bacterial contamination should be performed in real-time with portable devices to prevent undesired consequences. However, the most common procedures for bacterial detection relies on microbiology laboratory tests such as biochemical kits, enzyme-linked immunosorbent assays (ELISA) and polymerase chain reaction (PCR) assays. All these techniques require much time for obtaining results and specific laboratory equipment. For these reasons, new techniques came to light mainly based on optical sensors to discriminate the bacterial presence; however, they are typically complex systems with a high-price. A very interesting approach to overcome these problems is to employ the impedance technique for bacterial detection, since the main advantages are portability, rapidity, low cost and above-all on-spot measurements. This application field of the impedance spectroscopy is called "impedance microbiology" and it is based on impedance variations occurring in culture mediums due to bacterial growth [43]. When bacteria are into a culture medium, they convert their large molecules (polysaccharides, lipids, nucleic acids and proteins) into smaller units (monosaccharides, fatty acids, nucleotides and amino acids) to release energy [43]. This mechanism reflects a change of the ionic composition of the growth media and, therefore, on the conductivity σ, which is related to the impedance Z through the relation:

$$\sigma = \frac{K}{Z} \tag{2.11}$$

where K is the conductimetric cell obtained by the electrode geometry and assembly as the ratio of the distance between electrodes and the area of a single (d/A). Since only live bacterial cells have metabolic activity, they are the only able to produce changes in the conductivity of the medium. For this reason, the impedance microbiology is used to discriminate live and dead cells and to monitor the growing in the culture. The bacterial growth can be represented by a typical impedance curve, shown in Fig. 45.

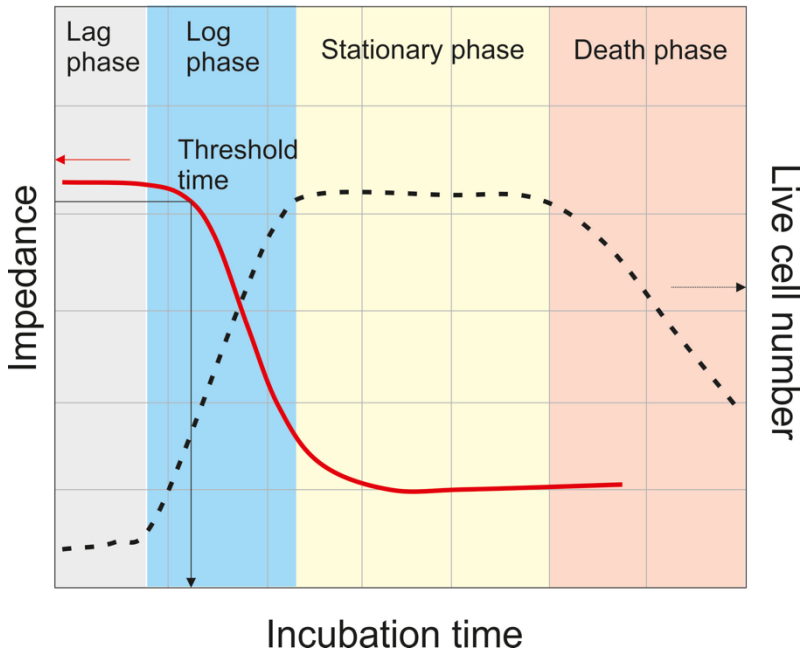

Fig. 45: Microbial impedance growth curve [43].

We can observe that microorganisms have to reach a minimum number to be detectable by impedance changes, whose trigger is represented by the threshold in *Log* phase. Then the impedance decreases because of the bacterial replication producing ions and, finally, becomes flat in the stationary phase where the growth is full and cells start to die (*death phase*). The target of this validation set is to reproduce the behaviour described in Fig. 45 using the developed vector analyser combined with a conductivity sensor and a spectrophotometer as reference. The working principle of such instrument is based on a monochromatic light hitting the sample, which partially reflects the excitation captured by an optic sensor. The comparison between the emitted light and the one absorbed by the sensor is expressed as a transmittance value, proportional to the bacterial growth and to the sample conductivity. The reference index used is the absorbance A related to the transmittance T with relation $A = \ln(t)$. For this reason, we can transform the data obtained by the vector analyser into conductivity values for a clearer matching.

Tests are performed using the developed vector analyser and a commercial conductivity sensor (LFS 1505 by Innovative Sensor Technology). The sample under test is the bacterial E. Coli, plunged into a Lauria-Bertani culture, placed into an incubator, with oscillating plate, reaching 37° C of temperature. The temperature behaviour is sampled by a thermocouple and used to compensate the conductivity measurement to further improve the accuracy of the system.

A user-friendly interface is also produced in Matlab for a real-time acquisition of the growth in term of conductivity. The results obtained with the vector analyser and the spectrophotometer in time are shown in Fig. 46.

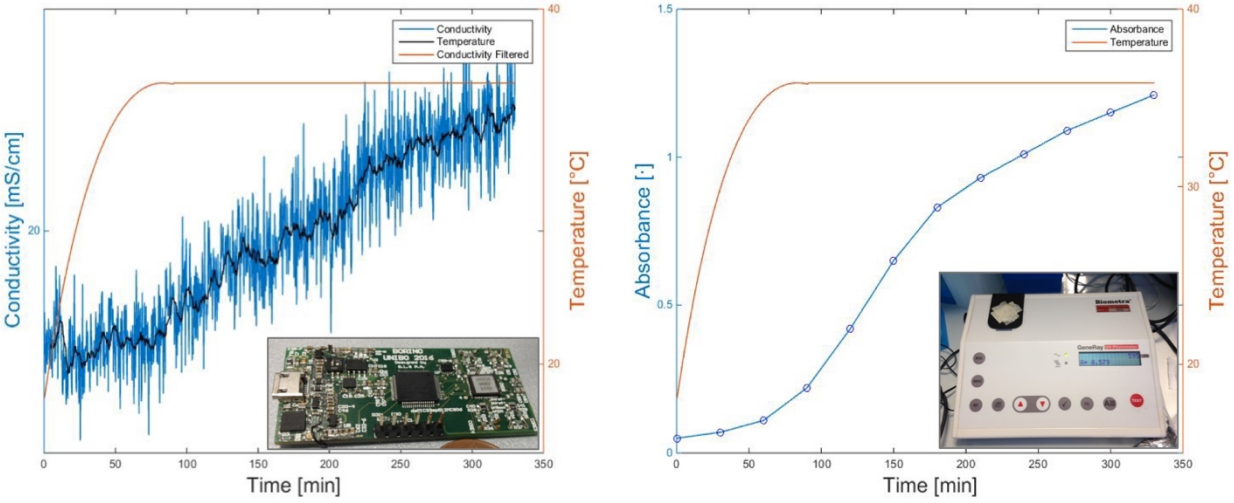

Fig. 46: Conductivity measurement performed with the vector analyser (a) and absorbance behaviour captured by the spectrophotometer used for validation.

From the above figure we can infer that both conductivity and absorbance increase, in particular a linear behaviour can be detected when temperature is firm at 37° C. As regards the phases described in Fig. 45, the Fig. 46 represents the linearity of the curve between *Lag* and *Log* phases where the angular coefficient is opposed in sign to the one in Fig. 45 because of the inverse proportionality between impedance and conductivity. In conclusion, the vector analyser can be successfully used for the bacterial detection and monitoring also for on-spot measurements due to the miniaturization and portability of the device.

2.3.2 Dynamic monitoring on mechanical heart valve

Serious diseases on heart valves are treated by surgical procedures involving the substitution of the diseased valve with a new mechanical (pyrolytic carbon) or biological (animal origin) one. All these prosthesis, however, can have problems related to the formation of thrombi or fibrous tissue (pannus) undermining the heart valve functioning. In particular, the blockage due to the presence of undesired material reduces the movements of the valve leaflets causing deterioration. Currently, the tracking of the dynamics of the implanted valves is performed by transesophageal eco or 3D TAC, which are expensive tests. For this reason, new emerging techniques are introduced to evaluate the open/close status of the leaflets on the basis of intra-valvular impedance (IVI). In this case, the mechanical valve embeds some electrodes generating a local electric field which senses the electrical potential variations produced by the leaflet movements. This "smart valve" is able to prematurely detect malfunctions based on impedance variations without involving imaging techniques [44]. We exploited the vector analyser for investigating the dynamic of the mechanical CarboMedics standard mitral valve (31 mm size) where four robber electrodes are glued on the internal diameter for a 4-wire Kelvin

measurement (Fig. 47). The valve is combined with a mock-loop machine, which is a hydraulic system simulating the opening and closing movements through an adjustable continuous current pump.

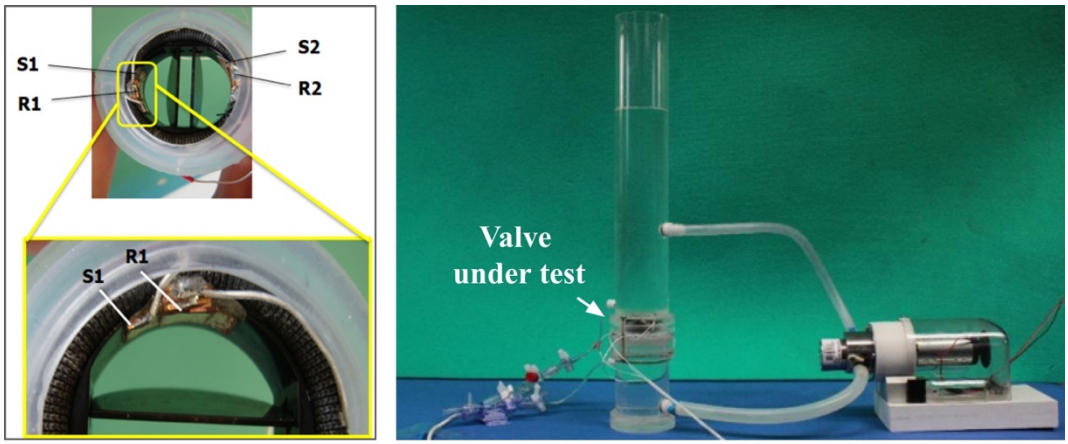

Fig. 47: Mechanical valve with electrodes (a) and mock-loop system (b).

The tests are performed with the above instrumentation and also with a commercial impedimetric system by Medtronic (Model2326) as reference, which excites the valve under test with a square biphasic wave at a fixed frequency of 4 kHz. The results obtained by testing the valve with the vector analyser (150 μA and LNA gain equal to 10) at various frequencies are shown in the next figure. From this, we can clearly identify the status of the valve thanks to the high resolution of the developed vector analyser. The absolute variations, in fact, are around few Ohms, while the smallest phase displacement is of few degrees. We can infer also that for those frequencies where the absolute value is reduced, the phase displacement is higher and vice versa.

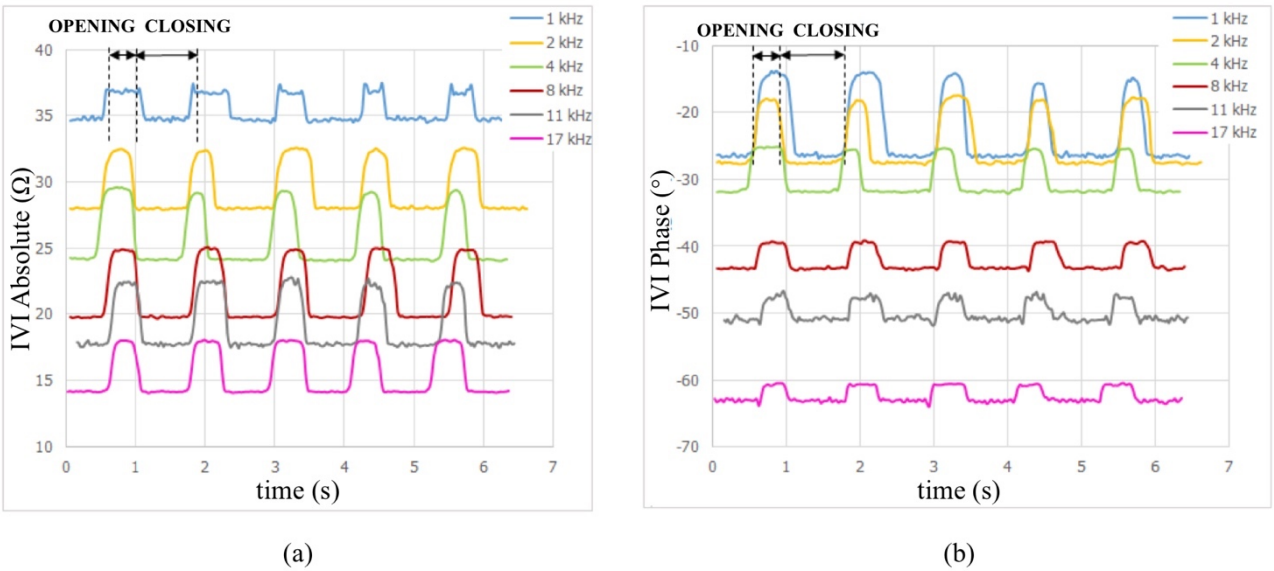

Fig. 48: Absolute and phase IVI of mechanical valve measured by the vector analyser.

In order to test the influence of the undesired material on the mechanical valve dynamic, a preliminary test is performed to select the frequency with the highest discriminative power. The test analyses the absolute and

phase impedance values for various frequencies when the valve is plunged into a physiological solution with different materials blocking the dynamic. We preliminarily used a rubber O-ring simulating the valve embedding four electrodes and sponge, flesh and robber samples, of the same fixed dimensions, simulating the thrombi.

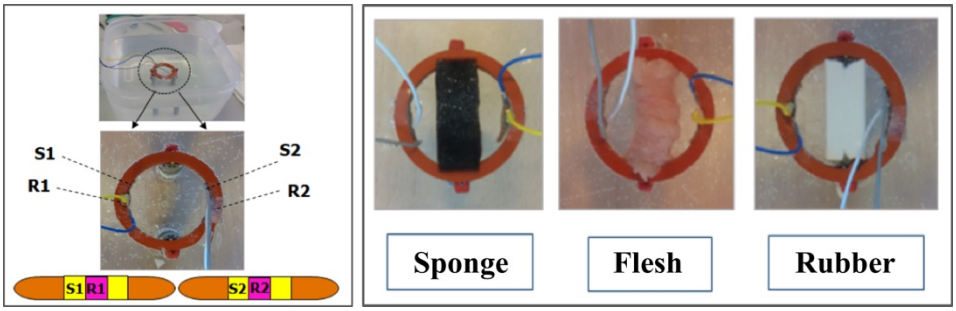

Fig. 49: Samples of various materials simulating thrombi.

The IVI impedance measured by the vector analyser (150μA and LNA gain equal to 10) is shown in Fig. 50 for absolute value and phase. It emerges that the frequency that better discriminates the difference among the various materials is 4 kHz. This is the frequency chosen for the test involving the mechanical valve Carbomedics when it is dipped into the physiological solution and its dynamic is blocked with sponge, flesh and rubber samples. The absolute and phase in Fig. 51 show small differences among the materials less than 2Ω and 1°. Therefore, the high resolution and accuracy of the developed device are essential for investigating how various materials interfere with the open/close status of the valve. By assuming only the rubber material and creating samples at different dimensions, the device is also able to detect the sample sizes through a variation both in amplitude and phase when the valve is open (Fig. 52).

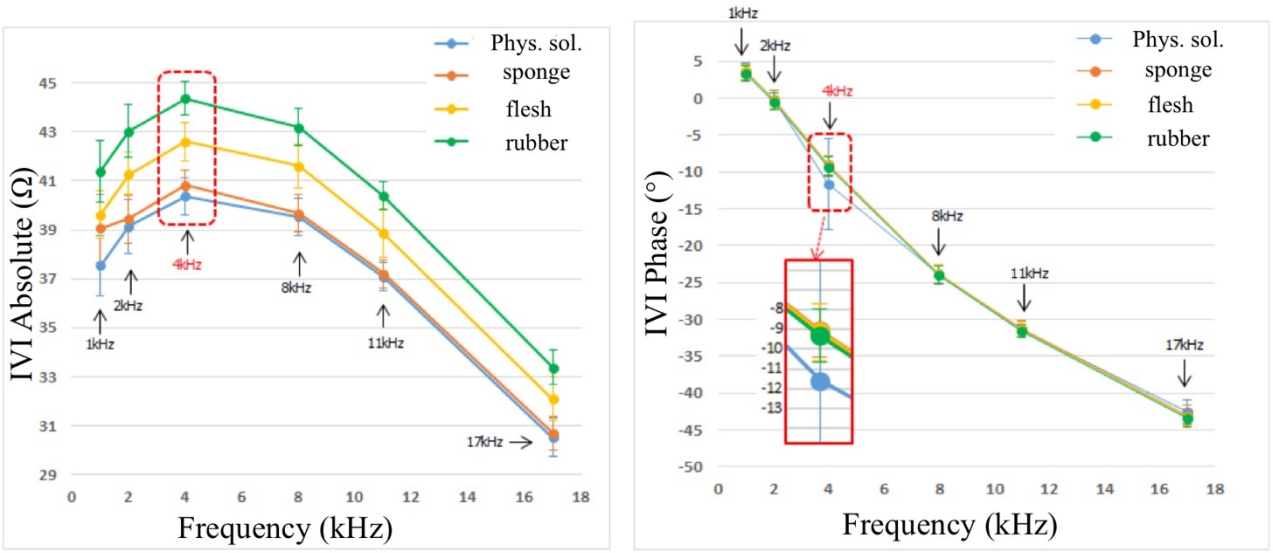

Fig. 50: Rubber valve test in physiological solution with various materials (sponge, flesh, rubber).

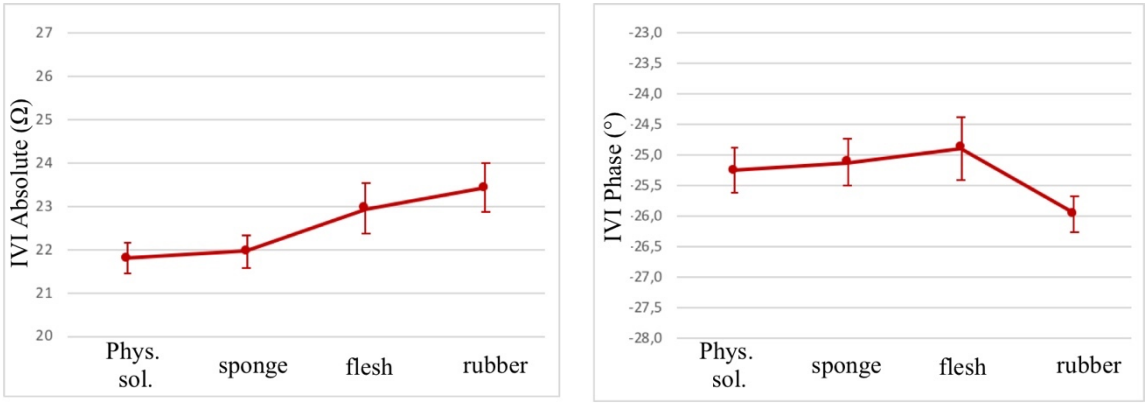

Fig. 51: IVI in absolute and phase for various material blocking the valve dynamic (4kHz).

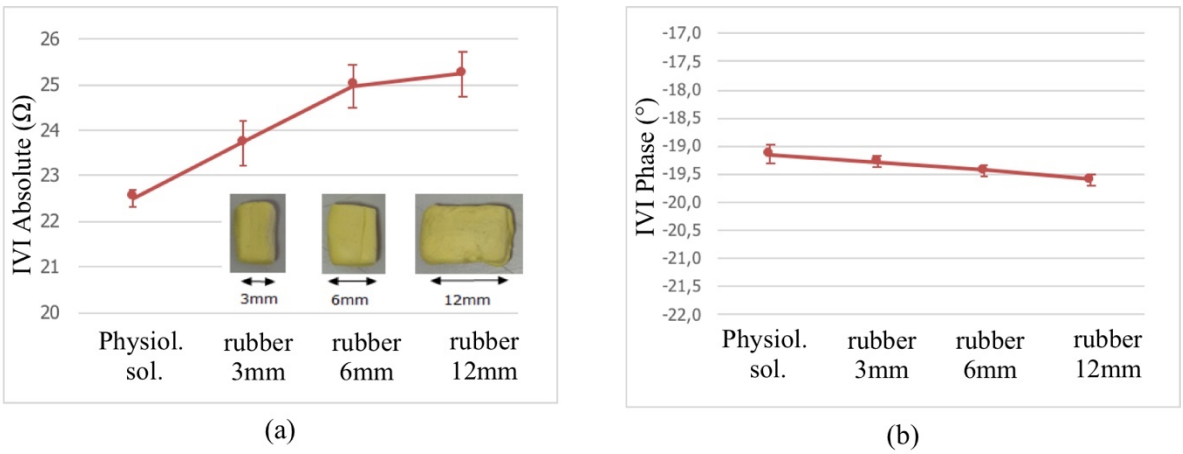

Fig. 52: Mechanical valve in open status when rubber samples (different sizes) block the dynamic.

These tests pave the way for a smart valve able to monitor changes in its working to prevent valve failure and dire situations. The high resolution of the vector analyser has a key role in the evaluation of the open/close status but also in the detection of some materials compromising the valve dynamic. The absolute and phase values are both significant in this application but they are considered separately. A further improvement of this system is to combine both information to predict the status of the material. In this perspective, the statistical analysis in Chapter 3 should be applied to boost the device performance.

2.4 Project relevance for thesis topic

The new direction proposed in this chapter is the high accuracy of the developed impedance analyser. This property is reached by the architecture of the chosen ASIC and by some strategies in the design of the entire device, ranging from the algorithm implementation to the choice of some external components. All these aspects should be taken into consideration specially for a desired application involving specific investigation frequencies. For example, we can observe that the result accuracy depends on the relation between the excitation frequency and the cut-off one of the external LPF filter. Therefore, the LP elements should be chosen on the basis of the material under test. Moreover, the LNA gain, as well as the OSR factor in the digital filter implementation, affect the quality of the measurement. If the application is known, therefore, a preliminary research of these parameters should be conducted on the basis of the above description. Moreover, a calibration should be applied to improve the result performance. This approach, based on some parameter investigation and on the calibration specific to the application, is a further optimization step for improve the accuracy of the device, whose architecture should be also studied to pursue the accuracy target.

The results obtained show reduced non-linearity errors specially at low frequencies (less than 22 kHz) where absolute value error is less than 1.5 % with a best case of 0.15 % at 1 kHz. For high frequencies, the error tends to increase up to 3.8 % (34 kHz). The same deductions can be drawn for the non-linearity error in phase where the best case is 0.07 ° (1 kHz) and the worst one is 0.26 ° (27 kHz). Also the device resolution is remarkable since the ENOB is equal to 13.8 bits. Such performances are successful also when compared with the commercial product LCR meter used as reference instrument.

As validation of this measurement approach, the calibrated vector analyser is used in biomedical applications for studying the bacterial growing in time and the dynamic of a mechanical heart valve. The accuracy is necessary in the impedance microbiology to detect the growing phases of microorganism in a culture mean. In this implementation result quality is also improved by compensating the conductivity measurement using the temperature information from which it strongly depends. Another performance of the vector analyser appreciated is the high resolution, which allows the discrimination of small displacement in amplitude and phase of the complex impedance. This is very precious in various applications such as for the tracking of the open/close status of the heart valve or to identify the presence of materials obstructing the valve functioning.

Since in real medical applications tissues present various impedance values, high accuracy and resolution of the sensing instruments can be decisive specially for diagnostic purposes.

Chapter 3: Boost on statistical tools for augmented impedance extraction

The impedance spectroscopy is a collection of data spread into a range of frequencies. It is used to investigate a material under test and indirectly assesses some characteristics, which are distributed in the spectrum even with complex relations. In this way, the impedance behaviour becomes a signature of the interaction between the excitation and the material, gathering a lot of information also related to specific properties of the material under investigation. The inference of these specific parameters among data, influenced by multiple variables, can be difficult unless powerful statistical tools are involved. The ability of such processing relies on the discriminative power to detect linear and non-linear behaviours and to isolate the information from undesired contributions. To reach this goal, we applied well-known statistical models (PCA, PLS, N-PLS , K-OPLS) not yet associated with the impedance extraction. In order to illustrate the application of the statistical model on impedance data, we proposed the elaboration for two moisture sensors, realized with a non-invasive probe and one in contact with the soil. Both sensors are based on the same working principle which relies on the excitation of a material through an electromagnetic wave generated by an antenna. When the stimulus is propagated to the soil, this partly reflects the wave also on the basis of the water content. The comparison between incident and reflected waves are studied in term of gain and phase, which respectively are defined as how much power contains the reflected wave compared to the transmitting one (scattering coefficients S_{21} (Section 1.2.1)) and how many angular degrees one is delayed or in advance to respect to the other. The statistical implemented model allows us to recognize the moisture content exploiting the double information of the impedance (gain and phase) and also modelling non-linear behaviours. The powerful statistical models, combined with both proposed probes, makes this system an innovative device usable as a sensor node in precision farming applications. In particular, the developed probes overcome some problems of the commercial devices which need to be installed in the soil with issues referring to the soil-electrode adherence. In fact, the first non-invasive probe we describe does not involve any contact with the soil, while the alternative probe proposed is installed into the soil but the propagation through an antenna avoid adherence problems. The manufactured portable sensor device is designed to be connected to other sensing nodes to return an accurate overview of the soil status aligning with the IoT trend. The next sections are divided according to the state of the art for commercial devices and the novelties introduced; then the system architecture and the results obtained by multivariate statistical analysis will be deeply studied. Evolutions and variations in the device manufacture will complete the current chapter.

3.1 State-of-art and novelties introduced

The first approach we are proposing is new in investigating soil parameters and it makes use of a waveguide for a non-invasive measurement and a powerful statistical tool to carefully predict the moisture content. Both novelties overcome two main problems of the commercially available moisture sensor; they are, respectively, the invasiveness and the application of a calibration model specific of the soil type. In fact, most of commercial devices have a probe installed in the soil as sensing part, which needs to be perfectly in contact with the measuring soil avoiding air gaps, which can negatively influence the moisture content information and, therefore, can require periodic maintenance. Moreover, such probe requires a calibration operation depending on type of soil. As reported by the United States Department of Agriculture (USDA) [45], a soil can be assigned to one of the twelve texture classes according to the values for the proportions of sand, silt, and clay, which are located along each of the three axes of the textural triangle in Fig. 53. Each class is represented by a range of grain size, an absolute density at % of moisture content and, consequently, a maximum moisture content hold by the soil type. Most of commercial probes need to be calibrated into the specific soil before the actual use, regardless of the measuring technique implemented. About this, the state of the art includes many techniques for the moisture content estimation with an indirect measurement based on the analysis of soil physical-chemical properties [46] [47]. These techniques substitute the direct gravimetric method based on soil evaporation with the sample drying through oven and the calculation of the mass of water lost as a percentage of the mass of the dried soil.

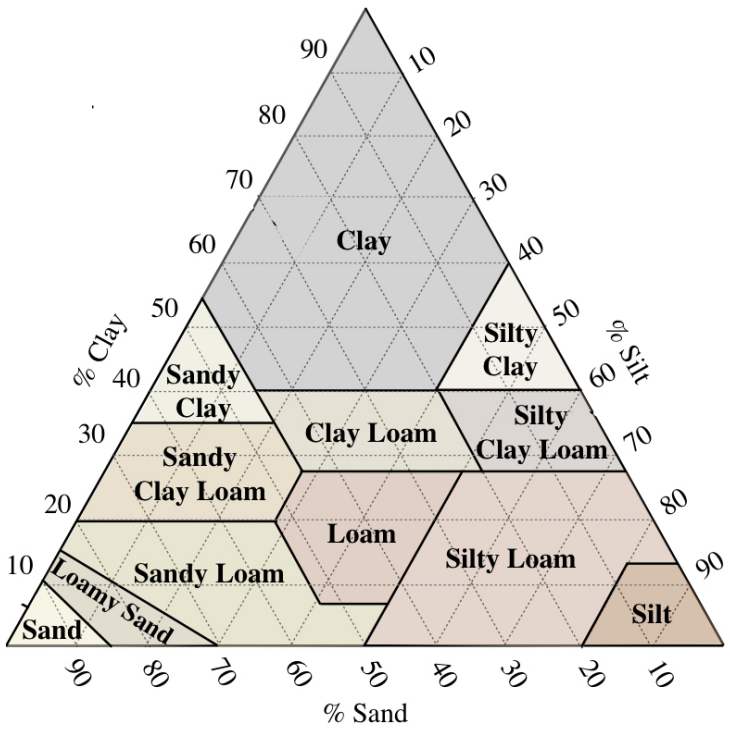

Fig. 53: USDA textural triangle showing the percentages of clay, silt, and sand in the texture classes [48]

The indirect methods involve: i) very costly and radioactive neutron scattering [49] and gamma ray attenuation sensors [50], ii) ground penetrating radar measurements [51], iii) tensiometers [47], iv) polymer-based microsensors and nano sensors fabricated on silicon wafers using micro-electro-mechanical systems [52], v) electrical resistivity probes [53] , vi) soil thermal properties measurements [54], and vii) infrared sensors [55] [56]. However, the most widespread tendencies are related to the assessment of dielectric properties among soil components [57] [58] [59] such as the invasive Time Domain Reflectometry (TDR), Frequency Domain Reflectometry (FDR) and capacitive techniques [60]. The basic idea of this family of technique is to excite the soil with an electromagnetic wave in order to stimulate only the water molecules, characterized by a dielectric constant equal to 80 at 20 °C (up to 3 GHz) which is higher than the other soil constituents and the air, which is approximately 1.00059 at 101325 Pa [61]. TDR determines dielectric permittivity of the soil mass by measuring the delay in time between the incident and reflected electromagnetic pulses (10 kHz - 10 GHz frequency range), which propagate along a stainless steel or brass probe installed in the soil [47]. The measurement depends on the probe shape [62] and it is influenced by air distribution, salinity, orientation and size of solid particles [63], because of which calibration models on the type of soil are introduced. On the other side, FDR and capacitive probes work determining the dielectric constant of a medium by measuring the charge time of a capacitor using that medium as a dielectric. The capacitance probe has a pair of electrodes (either an array of parallel spikes or circular metal rings) which form a capacitor with the soil [47]. As opposed to the capacitive probes, which work at mono-frequency excitation, FDR collects the information in a wide range of frequency typically at 10 - 150 MHz. As the TDR technique, both FDR and capacitive approaches have a certain sensitivity to the composition of the region adjacent to the probe including the soil grain size, air bubbles and soil composition. The adherence problem between soil and probe is a consequence of a measurement centered in a small area, meaning that some information in depth are not allowed. About that, the architecture of the non-invasive probe we propose has the potential to identify moisture gradient up to a specific depth. The same goal can be performed also with the other alternative probe, which is installed in the soil but the electromagnetic propagation is irradiated in a surrounding region. This means not only that the issues of electrode/soil contact are surmounted but also that the probe can embed different antennas along the length to investigate the moisture gradient. Therefore, both the probes can allow the moisture measurement in depth furtherly enriching the information on soil status and becoming innovative with respect to the commercial devices available. Since the two systems proposed are based on the same architecture, but mainly differ in the probe choice and in the statistical method, we start with the description of the system architecture for the non-invasive probe and then we will show, at the end of this chapter, variations introduced for the alternative one.

3.2 System architecture

The new non-invasive sensor for moisture sensing has an open-ended rectangular waveguide as a fundamental part of the system. The idea comes from a patented waveguide vector spectrometer for the assessment of food compositional parameters by L. Ragni et al [64]. The waveguide directs the flow of an electromagnetic wave, generated by a transmitting (TX) antenna, along its length until it hits the soil, which reacts with a reflected waveform captured by a receiving (RX) antenna. Both the antennas are, therefore, embedded in the waveguide in the internal surface as in Fig. 54, where we can appreciate that the RX one is along the way of the transmitting signal collecting both the TX and RX contributions. The dimensions of the waveguide (9.6 cm × 24.5 cm × 4.6 cm) was studied to guarantee a high-pass filtering with a cut-off frequency of 1.56 GHz, while the maximum frequency investigated can reach 2.7 GHz.

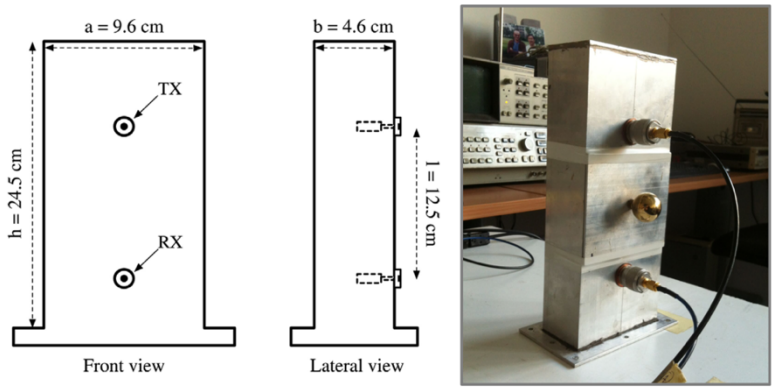

Fig. 54: Layout and picture of the waveguide implemented (figures are not to scale).

The system associated with the waveguide has the double task of generating an AC signal at RF frequency (1.5 GHz - 2.7 GHz) and comparing the TX and RX signals in order to extract the complex impedance, therefore acting as a vector analyser. The block scheme, proposed in Fig. 55, shows the connections between the RF source and the gain/phase detector with the waveguide involving also blocks for the acquisition of the complex impedance and the processing using a personal computer.

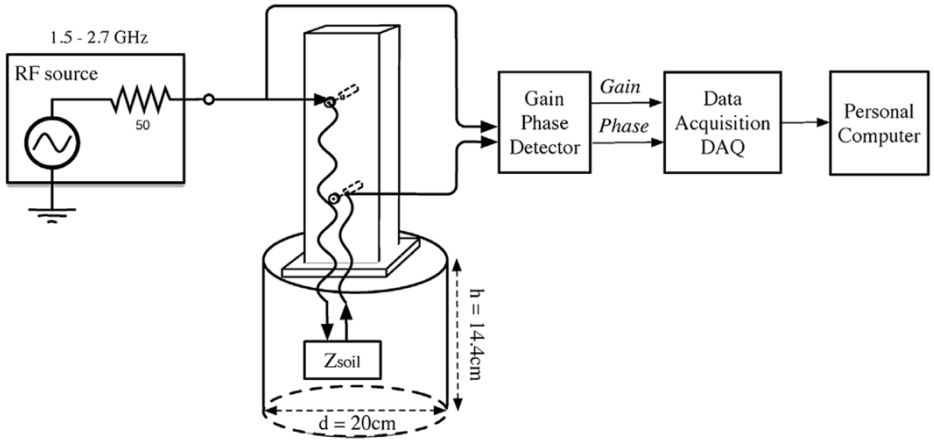

Fig. 55: Block scheme of the waveguide-based system.

The RF source can be chosen depending on the final application of the system. For preliminary tests in laboratory also test bench instrumentations can be used with the aim to generate a linear sine wave sweep from 1.5 GHz to 2.7 GHz. For this purpose, the sweep oscillator mainframe HP8350B combined with the HP83592B RF plug-in by Hewlett-Packard was employed for sending out the sweep with a duration of 60 s and an output power of 13 dBm. The RF signal needs also to be split (two ways at 6 dBm), as shown in Fig. 55, to both the waveguide and the gain phase detector. The use of the splitter, combined with a 0.7m coaxial cable, attenuates the power at the input of TX antenna which has been measured to be equal to 4.3 dBm (at 1.5 GHz) and 5.4 dBm (at 2.7 GHz). The gain/phase detector is a fully integrated system AD8302 by Analog Devices [65]. The general structure of the detector is represented in Fig. 56.

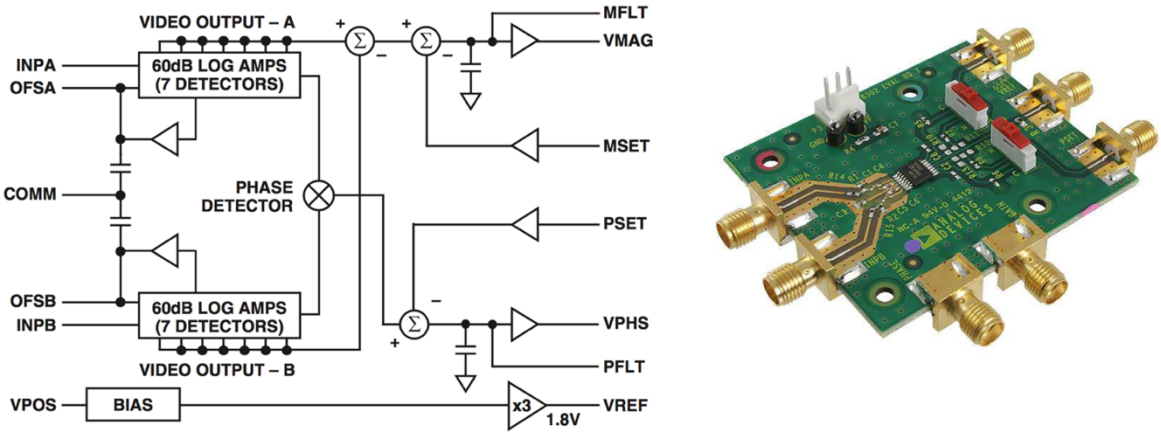

Fig. 56: General structure of the AD8302 and related evaluation board used for test.

First of all, it consists of two logarithmic amplifiers which compress the input signals (INPA e INPB, respectively for channel A and B), characterized by a large range, into a compact decibel-scaled output in the current domain. Then a phase detector, with a symmetric structure, returns a current signal proportional to the difference between INPA e INPB voltage phases. We can observe that the architecture of the phase detector implemented does not allow to distinguish between +90 ° or -90 ° having an ambiguous phase difference of 180 °. Both in magnitude and phase paths, respectively on the top and on the bottom part of Fig. 56, a subtraction operation is implemented to evaluate the difference between the two channels, while a further subtraction block for each path is necessary to remove setpoint inputs (MSET and PSET). The resulting differences are integrated in the averaging capacitors at MFLT and PFLT pins and buffered to obtain VMAG and VPHS. While VPHS can assume values from 0 ° to 180 ° scaled to 10 mV/degree, VMAG can vary from -30 dB to 30 dB scaled to 30 mV/dB with inputs (INPA e INPB) between -60 dBm and 0 dBm. The 0 dBm maximum value in input forces to use an attenuator for the TX path in Fig. 55, chosen with 20 dBm as attenuation factor. We can note that, these technical strategies do not influence the accuracy of the final moisture content, in fact the useful information is contained in the relative measurement between transmitting and receiving signals. To complete the description of the block scheme (Fig. 55), the data acquisition is entrusted to a DAQ USB-4431 by National Instruments with a resolution of 24 bits and 100 Sa/s as sample frequency, while a LabVIEW (NI 2014) interface is developed to easily collect data on the PC. The set-up built

for the test in laboratory, made up by the RF source, the waveguide and the evaluation board of AD8302 (AD8302-EVALZ) with the LabVIEW interface are shown in Fig. 57.

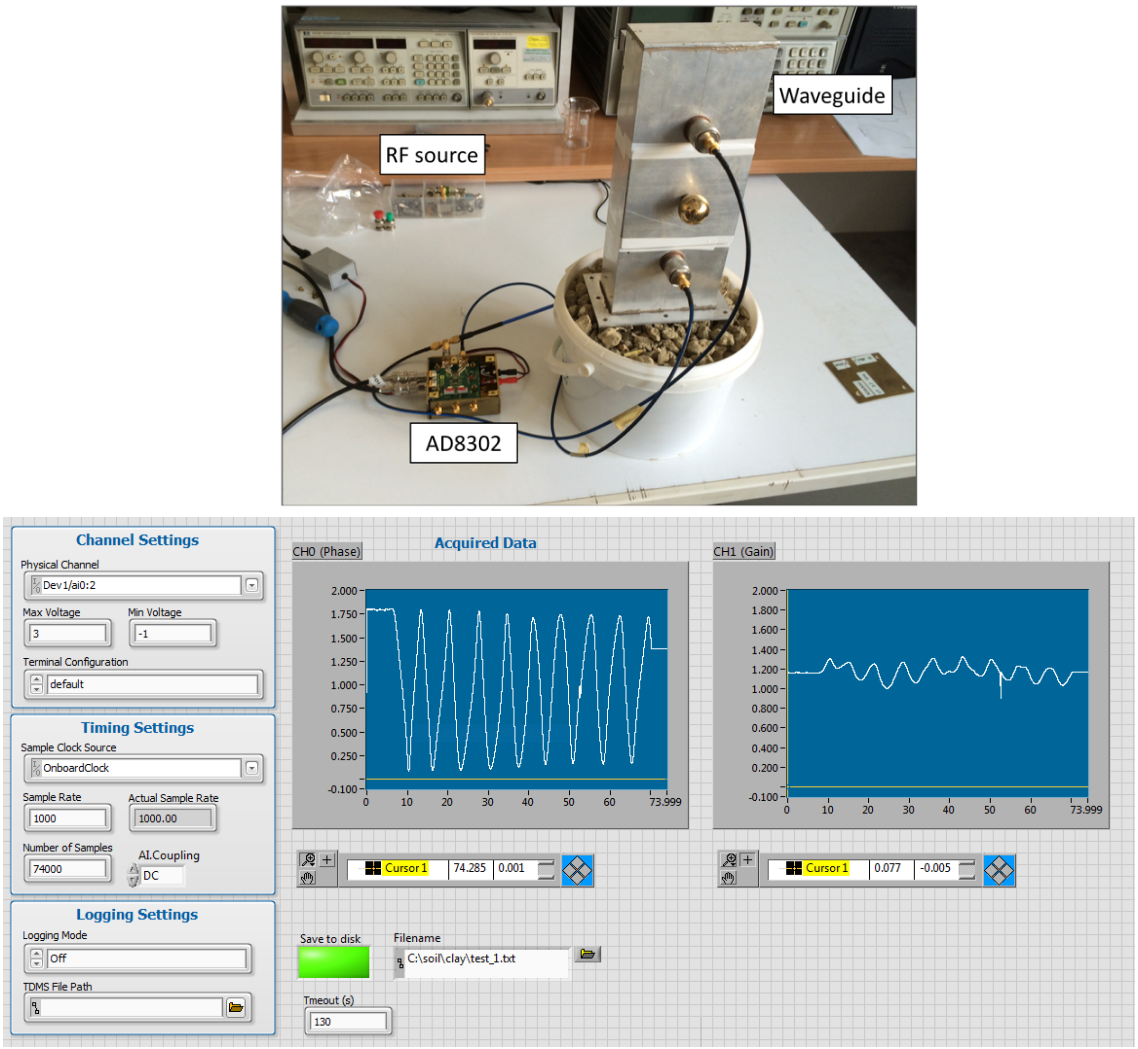

Fig. 57: Set-up with test bench instrumentation and LabVIEW interface for data acquisition.

The LabVIEW interface is designed to mainly select the sample rate and the number of samples we want to collect. It allows to display the gain and phase information and to save data on a text file for post-processing. The described system should be combined with powerful statistical tools to discriminate the moisture content information in magnitude and phase spectrum. The explanation of the statistical analysis adopted is explained in the next section.

3.3 Multivariate statistical analysis

Multivariate statistical analysis refers to advanced techniques for examining relationships among multiple variables at the same time. The method applied for the soil moisture sensor is the Partial Least Square (PLS) bilinear approach as data compression, where new variables are built from the original ones reflecting the latent structure or principal components (PC). To fully understand the working principles and the potentiality

of the PLS, the following description is divided into three main parts: Principal Component Analysis (PCA), Partial Least Square (PLS) and N-way PLS (N-PLS).

3.3.1 Principal Component Analysis (PCA)

Principal Component Analysis (PCA) is a dimension-reduction tool that can be used to reduce a large set of data, containing multiple inter-correlated variables, into a small one that still contains most of the information. This is achieved by transforming a given data matrix X (N-observation and P-variables) into a new set of principal components (PCs), which are uncorrelated and ordered so that the first few PCs retain most of the variation present in all the original variables.

Let us identify the X_j matrix elements with $j = 1...P$ so as $X = [X_1, X_2, ..., X_p]$, then a linear combination of these variables can be written as:

$$t_1 = w_{11}X_1 + w_{12}X_2 + ... + w_{1p}X_p = w_1^T X \tag{3.1}$$

where t_1 is a new vector in the same space as X_j, and w_{ij} are weight coefficients. Since the matrix X contains variation relevant to the problem, it seems reasonable to have as much variance as possible also in t_1 defined as $var(t_1)$. If this amount of variance in t_1 is appreciable, it means that this new variable is a good summary of the all X_j variables and the problem can be expressed as the research of optimal weights to maximize $var(t_1)$.To evaluate how the variables equally contribute to the variance contained in t_1, it is necessary that weights are normalized and the matrix X has to be centered and scaled. Therefore, the problem can be summarized as the maximization of the variance described as: $\max_{\|w_1\|=1}(var(t_1)) = \max_{\|w_1\|=1}(t_1^T t_1)$. Observing the Eq. (3.1), the problem can be translated into: $\max_{\|w_1\|=1}(w_1^T X^T X w_1)$, which is a standard problem in linear algebra, where w_1 is the first eigenvector of the covariance matrix of X.

To correctly understand how t_1 is a good representative of X, the most intuitive solution is to project the variables of X, represented by its columns, on the new variable t_1 applying a regression as follows:

$$X = t_1 p_1^T + E_X \tag{3.2}$$

where p_1^T is the regression coefficient vector and E_X the matrix of residuals. We can note that, the coefficients in p_1^T should be considered as a criterion for assessing the information capability of t_1, exactly like the weights in Eq. (3.1). In the PC theory, $p_1^T$is called loading vector, t_1 is the score vector and the "principal component" term is associated with the combination of these two quantities [66].

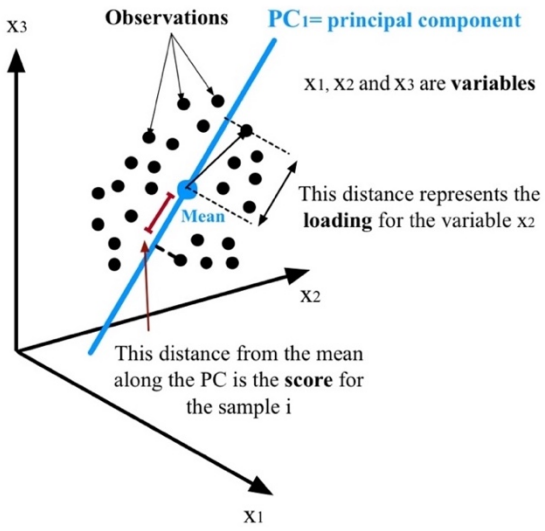

Fig. 58: Geometrical interpretation of one-PC model into a data set of 3 variables [67].

From a geometrical point of view, Fig. 58 shows a swarm of points representing the data on X in a P dimensional space with p=3 and one principal component model summarizing the data. The Figure also allows to discriminate that the fitting of data points on the PC line is a least square process [67]. In the luckiest case, we can have one principal component which explains all the variance of the original data. However, the complex nature of the data set typically does not allow to be explained by only one PC but it requires different PCs, each of these explains a variance contribution independent from others. This leads to extend the previous explanation into a higher dimensionality, where the score and loading vectors become matrices as follows:

$$X = TP^T + E_X = \widehat{X} + E_X \tag{3.3}$$

where $\hat{X}$ differs from X for the residuals and, therefore, can be considered a model of X [66].

An interesting approach to exploit the potentiality of the PCA and better interpret data is to visualize the score and loading plots. To understand the interpretations of these plots we refer to the example in the reference [68], where the spectra obtained by a Near-Infrared Spectroscopy (NIRS) technique is used to classify the adulteration of pure olive oil by soya, sun flower, corn, walnut and hazelnut oils. Fig. 59 shows the score plot of the first three components that explain 99 % of the variance in the spectral data. The figure shows the 3D plot, according to the number of components chosen, where the oils are grouped on the basis of the scores. It becomes clear that the score grouping reflects on the adulteration grouping as explained by the labels (soya, sun flower, corn, walnut and hazelnut oils) in the figure. This method of classification is called SIMCA (Soft Independent Modelling of Class analogies).

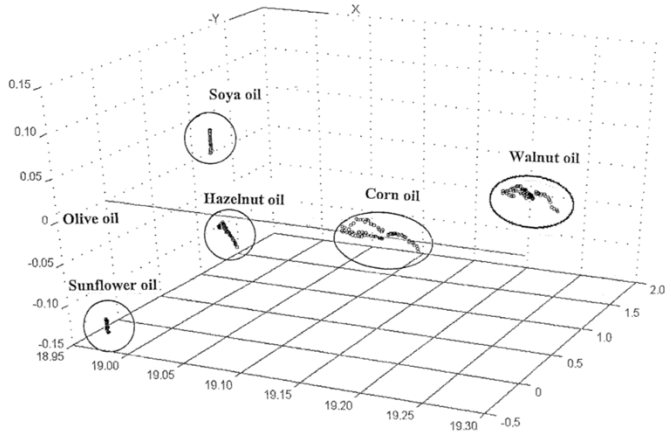

Fig. 59: Example of score plot for adulteration identification on oil samples through NIR spectroscopy [68].

Another useful plot is the loading behaviours respect to the variables. We propose the loading analysis performed from spectral NIR acquisitions for the evaluation of the quality characterization of apricots [69]. The loadings are calculated for the first four components respect to a wavenumber range associated with the NIR investigation. From the plot in Fig. 60 we can observe that X-loadings have similar behaviours in the central part of the plot. However, since the loadings explain what the principal components are representing, the superimposition of the curves makes difficult the identification of different pieces of information given by the PCs. Therefore, the wavenumber ranges, where the absolute variation of the loading curves is bigger, represent good investigation ranges. The loading plot is then used for selecting specific regions among variables, where the discriminative power of the PCs is more powerful.

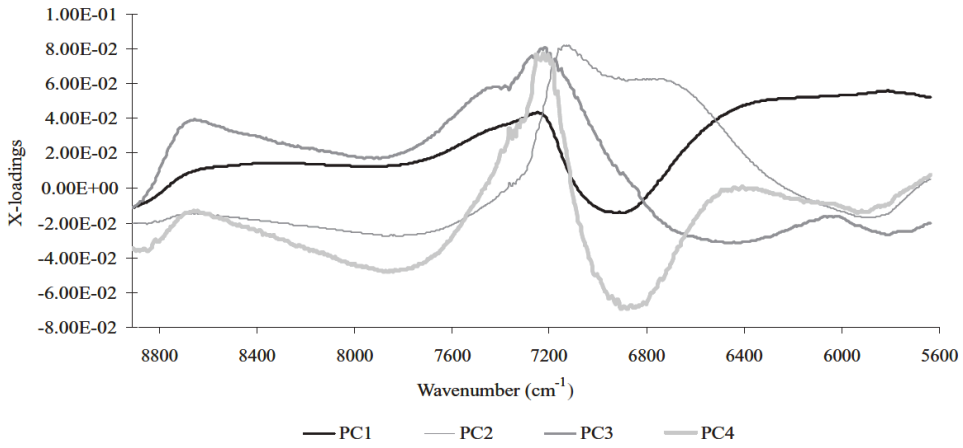

Fig. 60: Example of loading plot for the quality characterization of quality of apricots through NIR spectroscopy [69].

Based on the above description, the PCA is considered an optimal statistical tool which can be used for first classification or, as commonly used, as a pre-processing tool for linear discriminant analysis, artificial neural network or linear regression [66] as Partial Least Square method described in the next section.

3.3.2 Partial Least Square Regression (PLS)

The Partial Least Square Regression (PLSR) is a linear regression based on the principal components of a set of independent variables (matrix X) and a set of dependent variables (matrix Y). The ability of this tool is to analyse a lot of data which are strongly correlated, noisy and even incomplete in both X and Y [67]. Applying the PLS, the predicted variables Y are modelled by means of a set of predictor variables, which are the scores of X. To completely understand the previous sentence, we can refer to the Eq. (3.3) where the score matrix T is a good representative of the information in X. Applying the same considerations to the dependent variables Y we can obtain the relative scores into the matrix U as follows:

$$Y = UQ^T + E_Y \tag{3.4}$$

with Q^T the Y-loadings and E_Y are Y-residuals.

As shown in Fig. 61 the two score matrixes T and U can be combined to find a PLS component (Fig. 61) through the relationship:

$$U = BT \tag{3.5}$$

where B contains the regression coefficients into a matrix form.

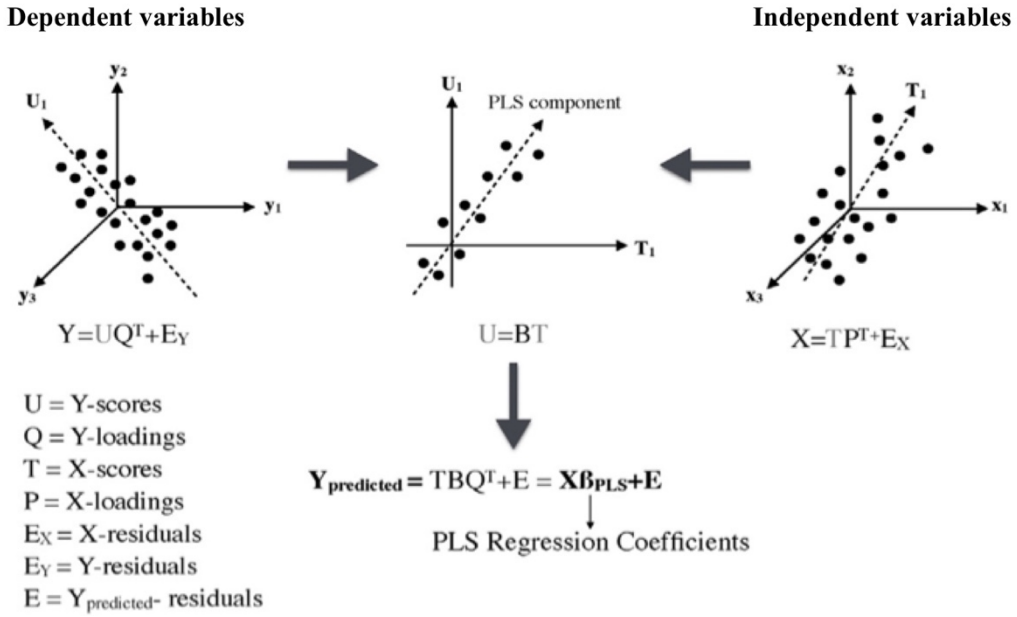

Fig. 61: Working principle of PLS [48].

By substituting Eq. (3.5) into Eq. (3.4), predicted dependent variables are so obtained [48]:

$$Y_{pred} = TBQ^T + E = XWBQ^T + E = X\beta_{PLS} + E \tag{3.6}$$

where E contains the residuals of Y_{pred} and β_{PLS} the PLS regression coefficients. In Fig. 61 we are supposing that the principal component is one, anyway if this is not enough to explain most of the information of the original data, we need also to consider other PLS components.

At this point the PLS model based on X and Y returns all the parameters described before: T, W, P, U, Q. To complete the development of the model and to be correctly applied in applications, it should be calibrated and validated. The calibration assures that the model properly assesses all the variables and conditions which can affect the model results and demonstrate the ability to predict observation from this effort. The validation can be considered an extension of the calibration, preferably using a new independent set validation X to predict the observations. The validation phase is mandatory to define the model as a good representation of a real system. One common approach applied for both these phases is the cross-validation (CV). It consists of randomly dividing the original data in groups and then build parallel models with one of the groups deleted [70]. In the calibration phase it can be useful to determine the optimal number of PLS components which affect the quality of the model [48]. In the validation phase, the CV is a smart strategy when new independent data are not available but the original data set is applied in a different way.

As regards the plots of the PLS parameters, the most significative ones show the relationship between predicted variables Y_{pred} and the original dependent ones Y. These plots can be obtained both in the calibration and validation phases, but this last one is the most significative phase. Based on this, the quality of this model is assessed by two regression parameters which are the coefficient of determination (R^2) and the root mean square error ($RMSE$).

R^2 explains the proportion of the variance in the dependent variables that is predictable from the independent ones. Assuming that y_i (vector of length n) is the original dependent variable observed and $\hat{y}_i$ the predicted one with the same length, the R^2 is expressed as:

$$R^2 = 1 - \frac{RSS}{TSS} = 1 - \frac{\sum_{i=1}^{n}(y_i - \hat{y}_i)^2}{\sum_{i=1}^{n}(y_i - \bar{y}_i)^2} \tag{3.7}$$

with $\bar{y}_i$ the average of y_i. Maintaining the same notations, the $RMSE$ measuring the difference between predicted and observed variables is calculated as:

$$RMSE = \sqrt{\frac{\sum_{i=1}^{n}(\hat{y}_i - y_i)^2}{n}} \tag{3.8}$$

Both indexes can be calculated in calibration phase, and after the validation where the parameters are more significative.

3.3.3 Variants of PLSR

Variants of PLSR are multiple and can act changing the data representation or the nature of the relationship between some parameters such as the scores of dependent and independent variables. Modifying the data representation is the basic idea of the N-way PLS developed by Bro [71]. It is useful when multi-way data in X are involved, for example when a measurement can be obtained with two different techniques and the predictive model wants to consider both of them for a better prediction. This means that the X matrix increases its order becoming an N-dimensional matrix depending on the N-techniques involved. If we simply assume that $N = 3$, the original data matrix is a third-order one represented in Fig. 62.

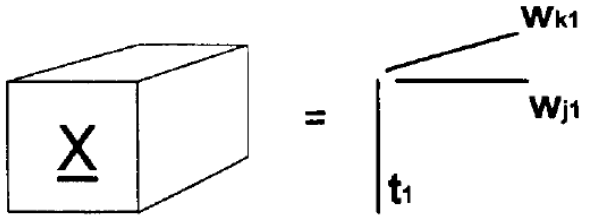

Fig. 62: Graphical representation of the 3D matrix with t_1 score and w_{k1} and w_{j1} loadings [71].

As regards Fig. 62 and the decomposition expreseds in Eq. (3.3), each element of the 3D X matrix can be represented as:

$$x_{ijk} = t_i w_j^J w_k^K + e_{ijk} \tag{3.9}$$

where w^j and w^k are two loading vectors [71]. The presence of these two coefficient vectors is the only variant compared to the classical PLS, therefore, the previous description can be applied assuming this shrewdness. The potentiality of this technique in impedance spectroscopy application is surprising since it can combine the two quantities absolute and phase in a unique model for the prediction of a specific information spread into both spectra.

Another big family of PLS variants involve modelling data with non-linear behaviour. Many systems, in facts, show underlying non-linear relationships which cannot be modelled by the classical linear PLS. However, the PLS framework can be still maintained using a non-linear transformation of variables. This non-linear operation can be directly applied to original data or, more common, to the relationship between the scores $(t,u$ in Eq. (3.5)$)$. As regards this method, many developed algorithms are based on the type of the non-linear transformation applied, but which still guarantees orthogonality among scores. Originally, this procedure was investigated by Wold [72] using a second order quadratic regression (QPLS) to fit the relationship between the scores as shown in Fig. 63 which can be compared with the linear approach in Fig. 61.

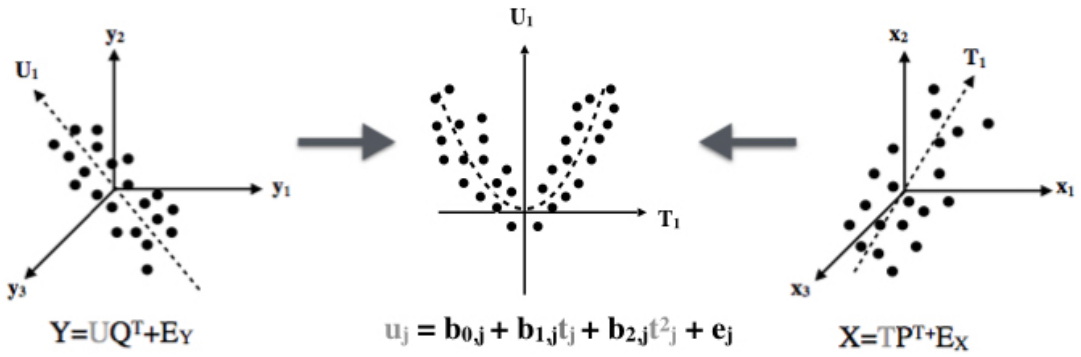

Fig. 63: Working principle of QPLS.

The mathematical relationship between the scores can be summarized using the single output score u_j as follows:

$$u_j = f_j(t_j) + e_j = b_{0,j} + b_{1,j}t_j + b_{2,j}t_j^2 + e_j \tag{3.10}$$

where $b_{k,j}$ for k=0,1,2 are the quadratic coefficients and e_j residuals [73].

However, it can be possible that the quadratic relationship does not perfectly match the trend between the scores and, for this reason, other non-linear functions should be introduced to overcome this problem. The generalization of this method involves a non-linear mapping with some smoothing regression procedures [74], spline functions (quadratic or cube) [75] or neural network algorithms [76]. As regards the techniques involving specific non-linear functions (quadratic, cubic,..), for which a pre-knowledge of the relationship between scores is necessary, a neural network with one hidden layer can be used to approximate any continuous function.

Another interesting approach based on applying the linear relationship between scores (Eq. (3.5)) but first pre-processing the data in a non-linear way is the Kernel Orthogonal PLS (K-OPLS). It is a combination of two PLS variations which are the use of a kernel function to move data in a high-dimensional space, where linear PLS can be used, and the orthogonality principle on data where the systematic information in X, not correlated to Y, is removed. The kernel PLS (K-PLS), which can be also applied alone as the orthogonal one (O-PLS), maps the original data into a high-dimensional space where data can become linear from the Cover's theorem [77]. After this manipulation, the PLS can be applied on the feature space. For the prediction of output variables, K-PLS provides an efficient method to deal with the nonlinarity issues.

On the other side, the classical O-PLS cleans the data from the systematic errors of measurement, or belonging to the system, which are not significative for the final prediction. From a mathematical point of view, it consists in removing the variation in X that is orthogonal to Y and applying the PLS scheme obtaining easier data to be interpreted. The only tricky point of O-PLS regards the iterative research of the orthogonal components, which can be time-consuming, and of the initial conditions to start the research [78]. To overcome this problem, the PCA described in Section 3.3.1 is a good strategy to find the initial condition saving time. An overview of the O-PLS is shown in Fig. 64.

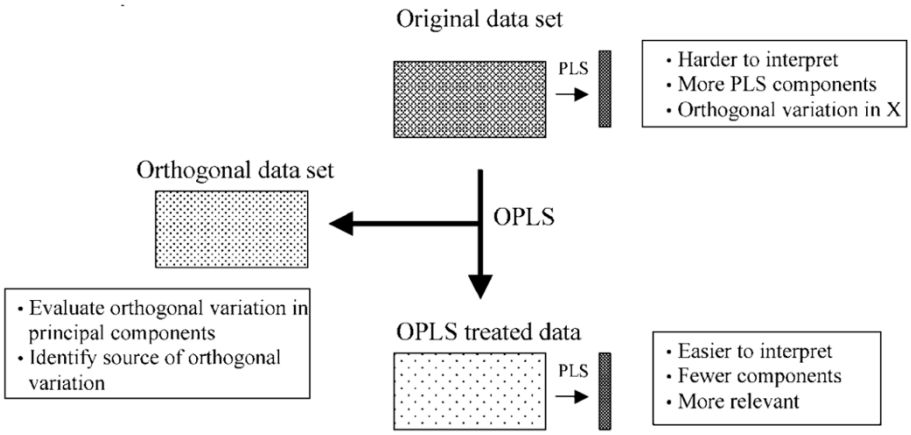

Fig. 64: Overview of the O-PLS technique [78].

By combining together the kernel transformation with the orthogonalization, a powerful and accurate statistic tool to investigate non-linear trends in system is obtained where the predictive variations are separated from the structured noise in the feature space [79]. The commonly used kernel function is the polynomial and the gaussian ones, respectively calculated as follows:

$$k(x,y) = (x^T y + 1)^p \tag{3.11}$$

$$k(x,y) = \exp(-||x-y||^2 / 2\sigma^2) \tag{3.12}$$

where p and σ are parameters which influence the predictive ability of the kernel method [79]. In the new created feature space, the variation in X are thus separated in two sets of latent variables representing orthgonal information. By respectively defining T_P and T_O as the predictive score and the corresponding orthogonal version, and applying the same description for the loadings (P_P predictive and P_O orthogonal), the Eq. (3.3), on the basis of the PLS regression, becomes [79]:

$$X = T_P P_P^T + T_O P_O^T + E_X \tag{3.13}$$

3.4 Test plan

The test plan is drawn up with the aim of evaluating the performance of the soil moisture sensor with different types of soil and with stratified samples at different moisture content. Following the USDA guidelines about the soil textural classification [45], we chose three types of soil as representative of the entire triangle with the information shown in the Fig. 65.

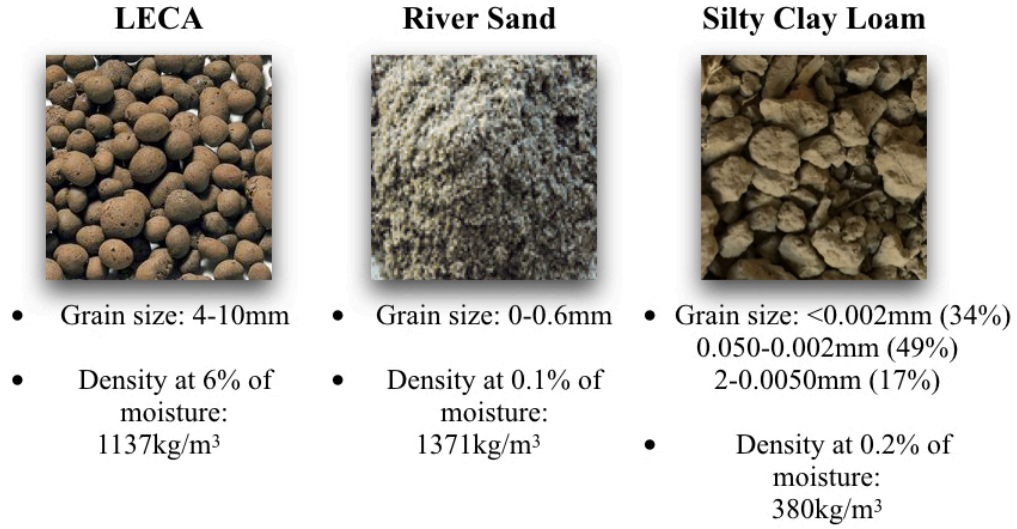

Fig. 65: Soil samples based on textural classification.

The Lightweight Expanded Clay Aggregate (LECA) sample belongs to the class Clay in Fig. 53 and it was purchased from local distribution (Laterlite, Italy). The river sand is on the bottom part and left side of the triangle (Fig. 53) and it is distributed by Bacchi S.P.A (Italy). Finally, the silty clay loam is collected from the agricultural soil in Emilia Romagna (a region in Italy) and it has an intermediate behaviour between clay and silt classes. To obtain a sample set at different moisture content, we first evaluated the field capacity of each type of soil and then calculated five moisture points in this range.

The procedure to reach the fixed moisture levels is developed adding a proportional quantity of deionized water to the driest sample (for each type of soil). Table 5 shows the physical parameters (moisture content, gravimetric and volumetric density, soil density and moisture soil density) obtained for all the samples involved in the tests [48]. For the tests aimed to the evaluation of the moisture content, each measurement is performed filling a plastic cylindric container (20 cm in diameter × 14 cm in height) with a specific sample. In order to evaluate the repeatability of the procedure, multiple measurements are executed while repositioning the waveguide on soil surface, mixing the soil and rotating the container on its axis of a constant angle (40 °) as described in Fig. 66.

Table 5: Physical parameters for soils samples at different moisture contents.

Soil	Moisture content (%)	Soil density (g/dm^3)	Moisture soil density (g/dm^3)	Volumetric moisture content (m^3/m^3)
River sand	0.1 ± 0.01	1485	2	0.002
	5.09	1318	67	0.067
	10.06	1409	142	0.142
	15.03	1496	225	0.225
	20.0	1603	321	0.321
LECA	0.2 ± 0.07	383	1	0.001
	7.2	402	29	0.029
	14.1	425	60	0.060
	21.1	452	95	0.095
	28.0	468	131	0.131
Silty clay loam	5.8 ± 0.8	1143	67	0.067
	11.5	1062	121	0.121
	16.9	973	165	0.165
	22.5	935	210	0.210
	28.0	834	234	0.234

The dependent variables are so collected in a matrix of 45 samples (5 moisture content for 9 repetitions) × 6800 spectra (gain or phase), while the independent variables are in a vector of 45 samples × 1 variable (moisture content, %). As regards the stratified, or double-layer tests, the container is filled with two overlapped layers (7cm each layer) at two different moisture content for each type of soil. The dependent variable matrix is built with 90 samples (10 stratified combination in Table 6 for 9 repetitions) × 6800 spectra (gain or phase), while the observed vector is 90 sample × 1 information (moisture content, %).

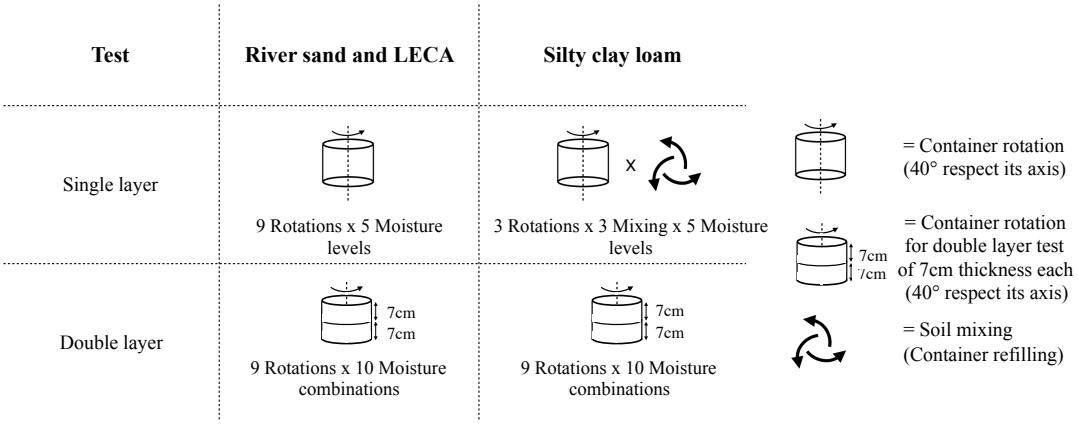

Fig. 66: Detail of repetitions on samples with container rotation and soil mixing [48].

Table 6: Combinations of layers at different moisture content [48].

Soil	Layer	Moisture combinations									
River sand	1	0.1%	5.1%	0.1%	15.0%	0.1%	20.0%	5.1%	10.1%	5.1%	15.0%
	2	5.1%	0.1%	15.0%	0.1%	20.0%	0.1%	10.1%	5.1%	15.0%	5.1%
LECA	1	0.2%	7.2%	0.2%	21.1%	0.2%	28.0%	7.2%	14.1%	7.2%	21.1%
	2	7.2%	0.2%	21.1%	0.2%	28.0%	0.2%	14.1%	7.2%	21.1%	7.2%
Silty clay loam	1	5.8%	11.4%	5.8%	22.5%	5.8%	28.0%	11.4%	16.9%	11.4%	22.5%
	2	11.4%	5.8%	22.5%	5.8%	28.0%	5.8%	16.9%	11.4%	22.5%	11.4%

Data are elaborated with the PLS and N-PLS tools in Matlab [80]. Results are shown in the next section.

3.5 Results and discussion

The first results obtained are related to the gain and phase spectra depending on the frequency points of the excitation signal. As we can see in Fig. 67 for LECA sample spectra, it seems difficult to appreciate the different moisture content, also in the zoom in Fig. 68 where changes are more relevant but still difficult to estimate quantitatively. Therefore, the insufficient discriminative power of these plots justifies the use of the statistical tools. As described in 3.3.1 section about the PCA, preliminary plots can be studied in relation to the score and loadings in order to discriminate where the information is focused and a classification depending on the moisture content. On the left plot in Fig. 69, there is a range of frequencies (1.5 GHz - 1.7 GHz) where the difference between the loadings of PC1 and PC2 is maximum in the absolute value. This means that in this range variability is better explained and it can be very useful for the moisture prediction. On the right side, the score plot helps to preliminary classify the samples, detecting 5 areas for each moisture content.

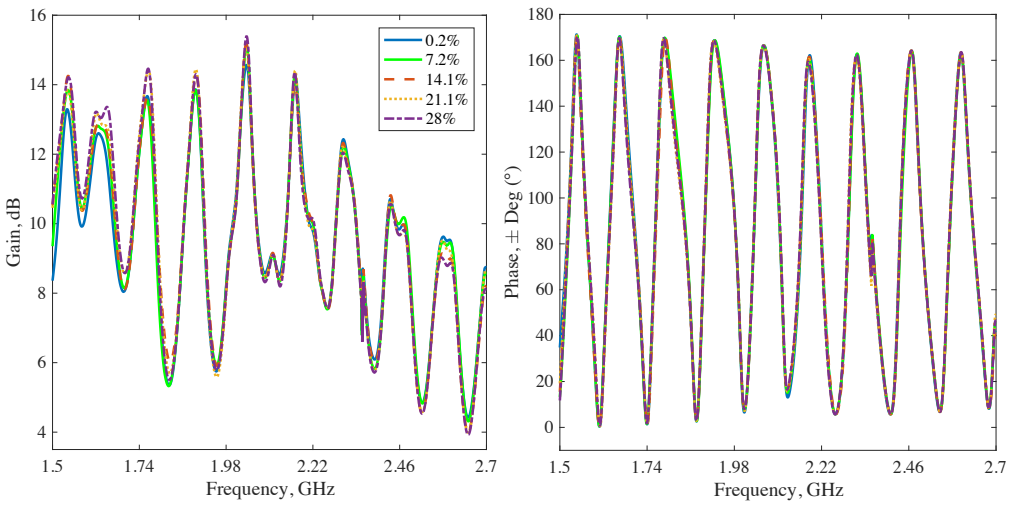

Fig. 67: Gain and phase spectra for LECA sample at different moisture content [48].

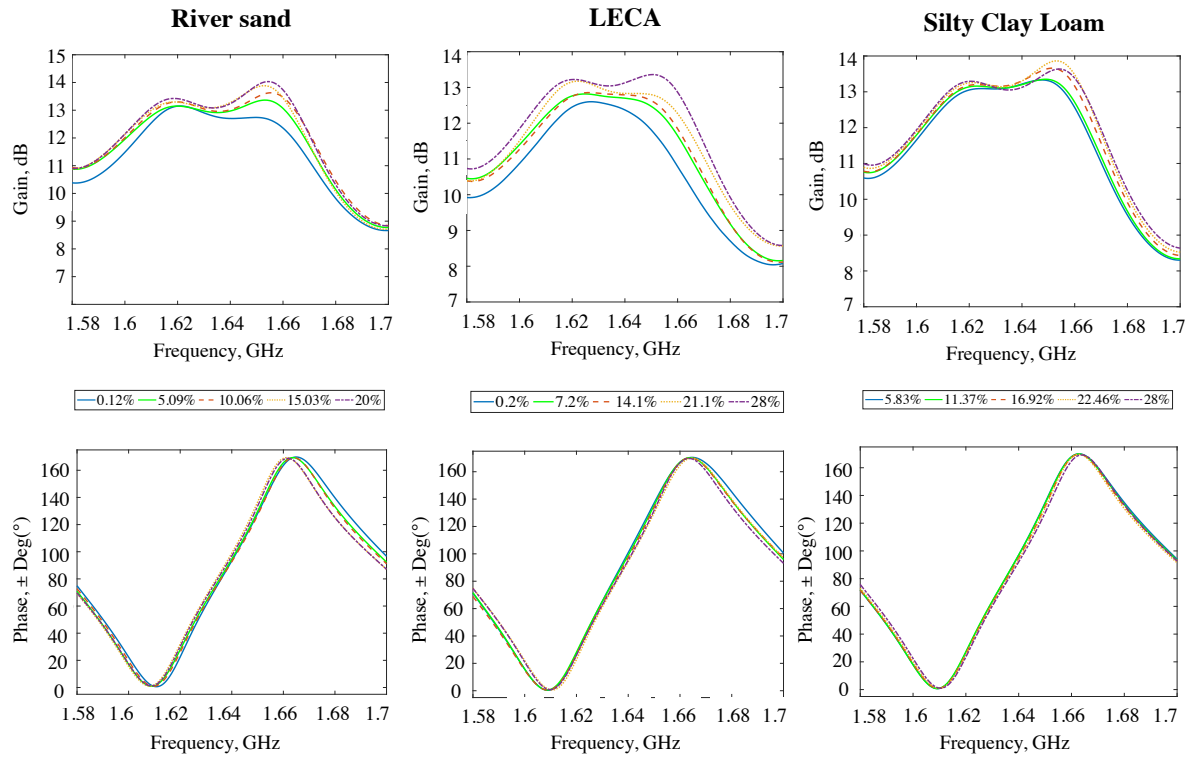

Fig. 68: Spectra zoom in 1.58GHz-1.7GHz for the three types of soil [48].

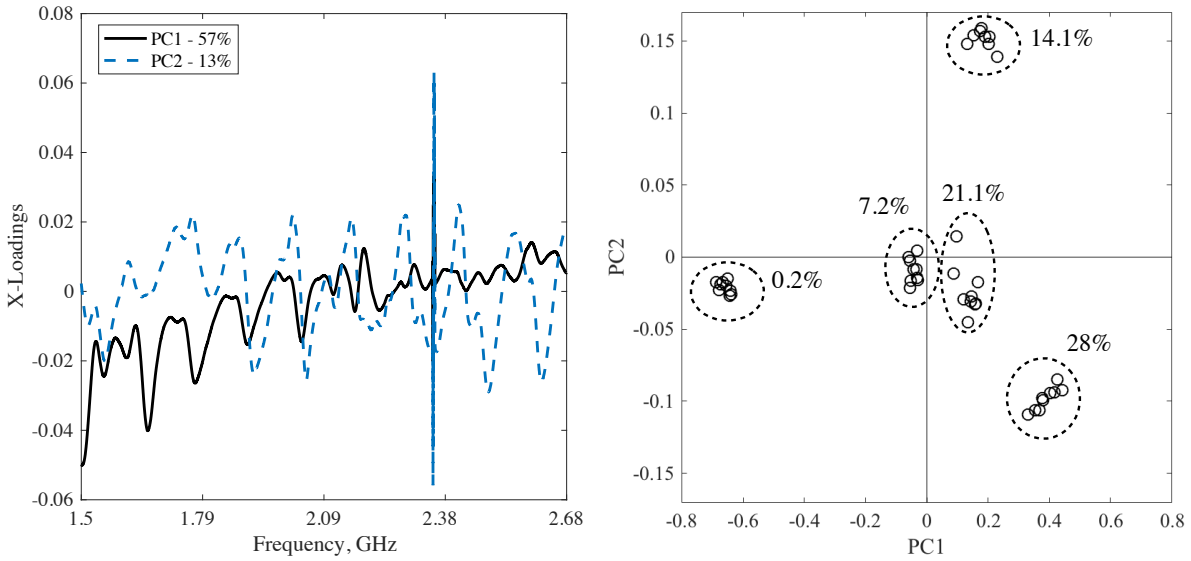

Fig. 69: Loading plot (left side) of PC1 and PC2 (Gain, LECA sample) [48].

On the basis of these inferences, we extract frequency ranges of interest for each type of soil and, therefore, PLS models are studied. The following Table 7 shows the R^2 and RMSE parameters in calibration and validation phases for the PLS models.

Table 7: PLS regression analysis for both gain and phase.

Soil	Parameter	Frequency range (GHz)	PLS regressions					
			Calibration			Segmented Cross Validation		
			PCs	R^2	RMSE	PCs	R^2	RMSE
River sand	Gain	1.5-1.7	4	0.992	0.6	4	0.989	0.8
	Phase	1.5-1.7	4	0.988	0.8	4	0.983	0.9
LECA	Gain	1.5-1.7	4	0.988	1.1	4	0.982	1.4
	Phase	1.5-1.7	5	0.991	0.9	5	0.988	1.1
Silty clay loam	Gain	1.5-2.68	5	0.982	1.0	5	0.941	1.9
	Phase	1.5-2.68	4	0.953	1.7	4	0.934	2.1

From this table we can infer that the best performance (higher R^2 and lower RMSE) is achieved by the river sand model (R^2=0.989 gain and RMSE=0.8), meaning that the prediction of the moisture content for this type of soil is very accurate. We can also observe a good performance for LECA and for the silty clay loam which has the most complex texture (swell phenomenon is appreciated) and, therefore, justifies less accuracy for the parameters. From a graphical point of view, the just discussed results, are reported in Fig. 70. To further improve the prediction power of these models, we can combine the gain and phase spectra in a unique model through the N-way PLS. The models obtained, shown in Fig. 71, are considered improved versions of the normal PLS model, since the R^2 increases and RMS decreases for LECA and Silty clay loam.

The second group of tests on stratified samples is studied with PLS models built for each combination of moisture content on layers and for each type of soil. The PLS parameters, reported in Table 8 show, for all the soil types, a good estimation for the first layer and a slightly lower accuracy for the deeper layer. These results underline the potentially of this novel sensor to investigate a moisture gradient in depth up to 14cm. The best results are obtained for LECA sample as in Fig. 72.

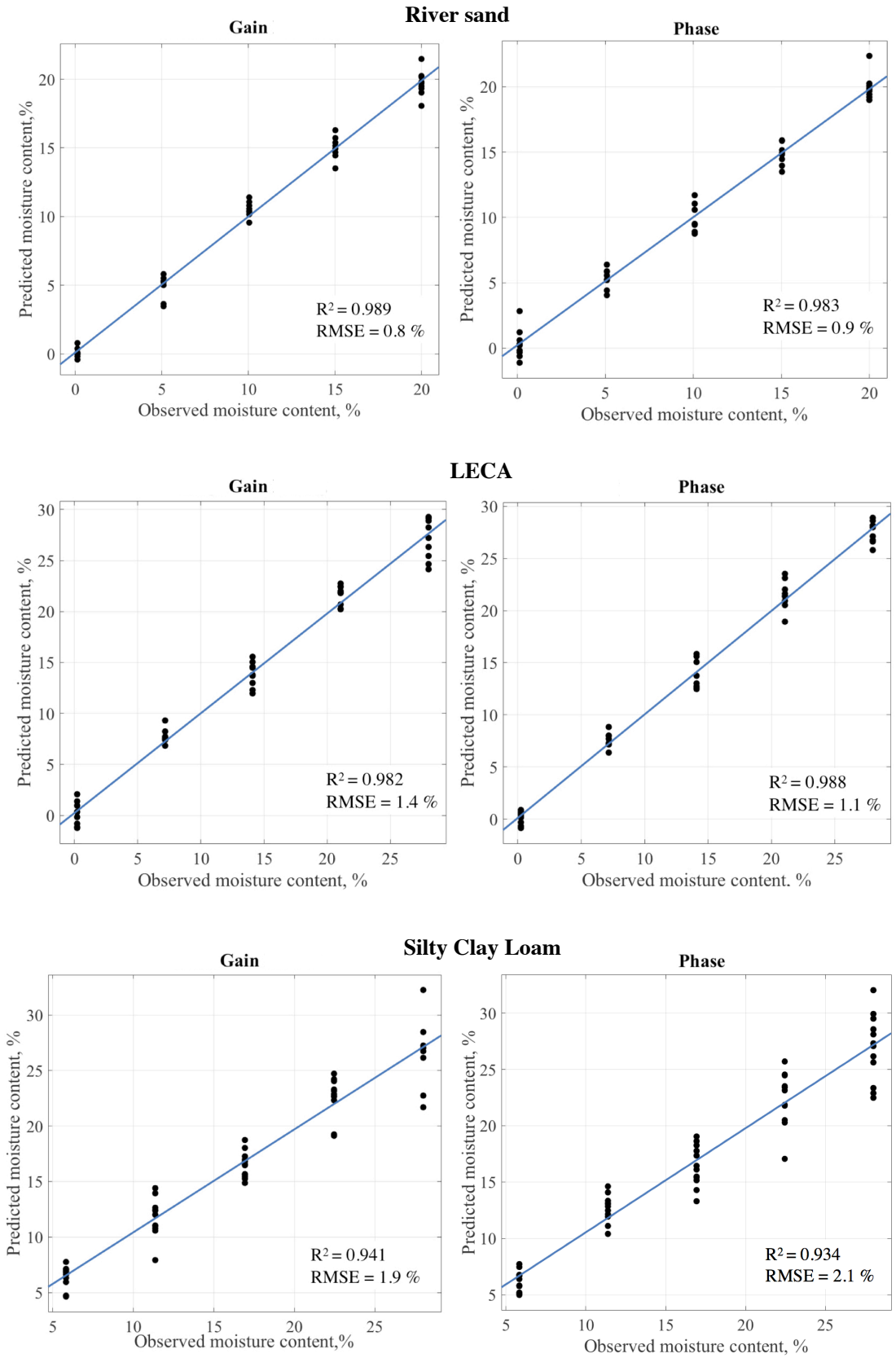

Fig. 70: Predicted versus observed values for soil moisture content (%) with PLS analysis (gain and phase) [48].

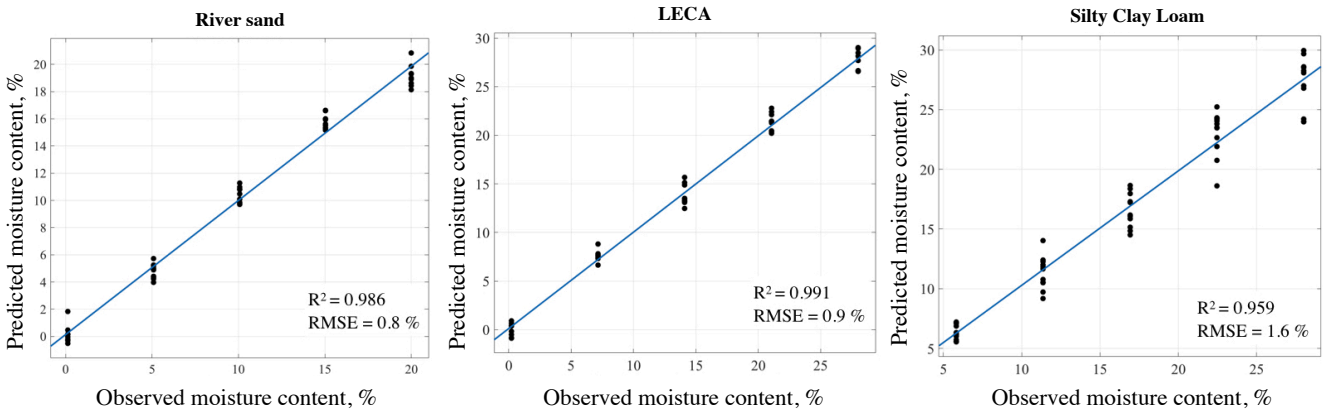

Fig. 71: Predicted versus obtained moisture contents (%) with N-way PLS model [48].

.

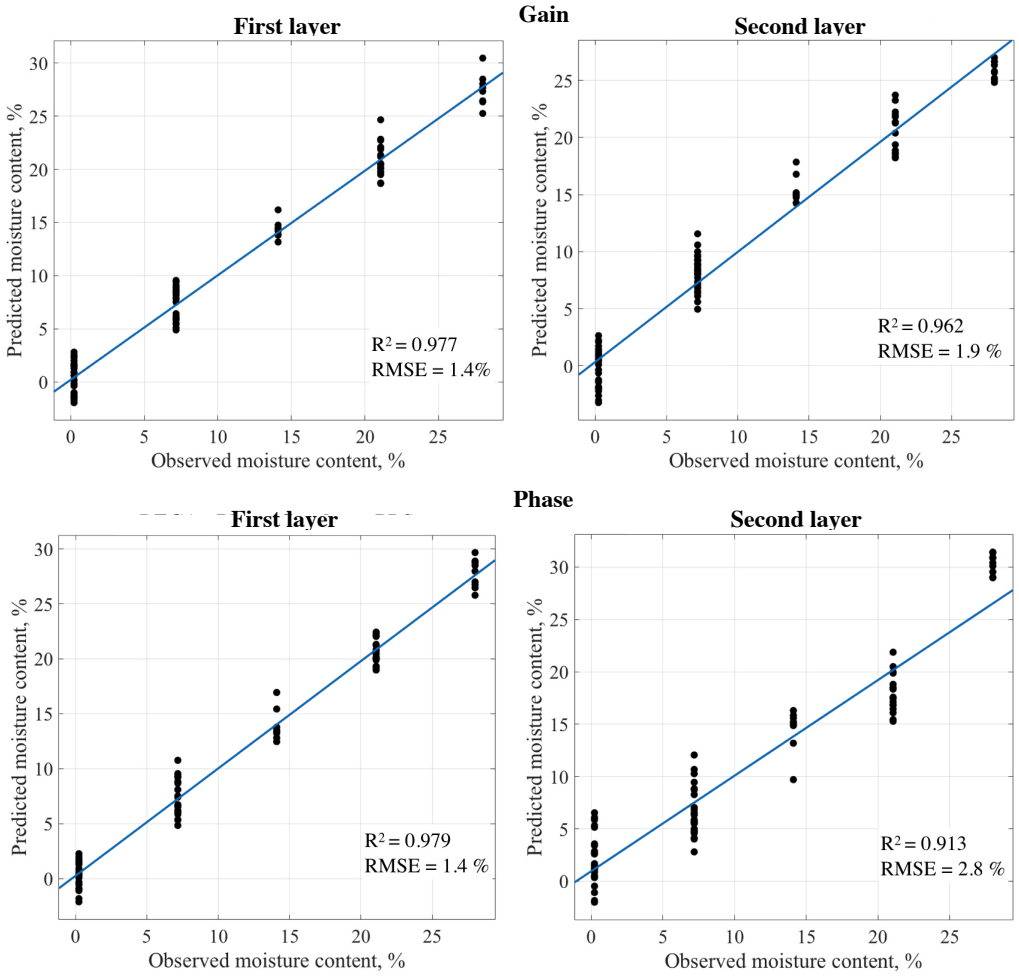

Fig. 72: Predicted versus obtained moisture content (%) for stratified tests [48].

Table 8: PLS analysis on stratified samples [48].

Soil	Parameter	Layer	Frequency range (GHz)	PLS regressions					
				Calibration			Segmented Cross Validation		
				PCs	R^2	RMSE (%)	PCs	R^2	RMSE (%)
River sand	Gain	1	1.5–1.7	2	0.948	1.5	2	0.942	1.7
		2	1.5–1.7	7	0.933	1.8	7	0.902	2.1
	Phase	1	1.5–1.7	5	0.970	1.2	5	0.963	1.3
		2	1.5–1.7	8	0.940	1.7	8	0.902	2.1
LECA	Gain	1	1.5–1.7	5	0.982	1.3	5	0.977	1.4
		2	1.5–1.7	4	0.968	1.7	4	0.962	1.9
	Phase	1	1.5–1.7	5	0.982	1.3	5	0.979	1.4
		2	1.5–1.7	3	0.922	2.6	3	0.913	2.8
Silty clay loam	Gain	1	1.5–2.68	3	0.956	1.6	3	0.946	1.8
		2	1.5–2.68	7	0.952	0.7	7	0.902	2.4
	Phase	1	1.5–2.68	4	0.961	1.5	4	0.947	1.7
		2	1.5–2.68	8	0.954	1.6	8	0.906	2.3

3.6 Compact implementation

The obtained results demonstrate that the non-invasive sensor, combined with the statistical method, successfully predicts the moisture content of a soil regardless of its specific type. However, the experimental setup, built to test the system, includes bulky bench instruments (RF source, DAC and PC) which make the measurements in situ difficult. In fact, the final application of this sensor has the role of an autonomous sensor node as part of an IoT network, therefore, a compact implementation is required to be applied in field. The basic idea is to manufacture a battery-powered device, reproducing the blocks in Fig. 55, with commercial integrated circuits (ICs) on a board, and allocate this in a plastic electrical junction box to be completely waterproof to the atmospheric agents. Fig. 73 shows the circuit box combined with the waveguide, which represents the autonomous sensor fed by a rechargeable battery. The status of the battery (in Voltage) is shown in a display embedded in the box, while the ON/OFF switch allows to enable/disable the circuit functioning.

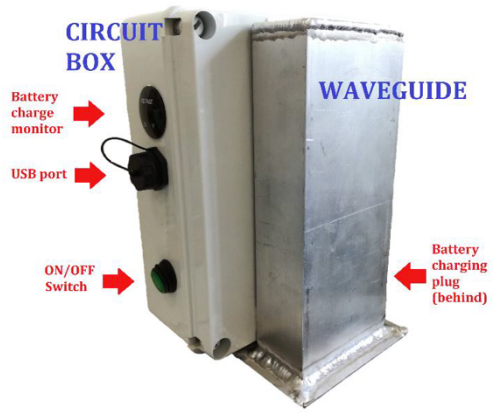

Fig. 73: Manufacture of the autonomous sensor device for soil moisture sensing.

The architecture of the circuit board (Fig. 74) can be summarized in the following four main sections: i) management and control, ii) source generation, iii) gain and phase measurement and iv) power (Fig. 74).
The management and control are entrusted to a microcontroller (µC) PIC24FJ256GB606 (Microchip Technology Inc.) which performs four tasks:

- provides an input signal x_n;
- samples and elaborate gain and phase data;
- writes these data on SD-card;
- communicates with a personal computer through a serial USB interface.

The signal, generated by the µC, is a codified information x_n of a linear ramp necessary for the voltage control oscillator (VCO). Such signal, digitally expressed with the Serial Peripheral Interface (SPI) protocol, is turned into the analogue ramp $x(t)$ through a digital to analogue converter (DAC) by Analog Devices (AD5761R). The ramp generated has a 16-bit resolution and an amplitude range between 0 to 20 V, which justifies the power source as combination of the DC-DC boost and the low-dropout regulator (LDO) at 21 V (Fig. 74).

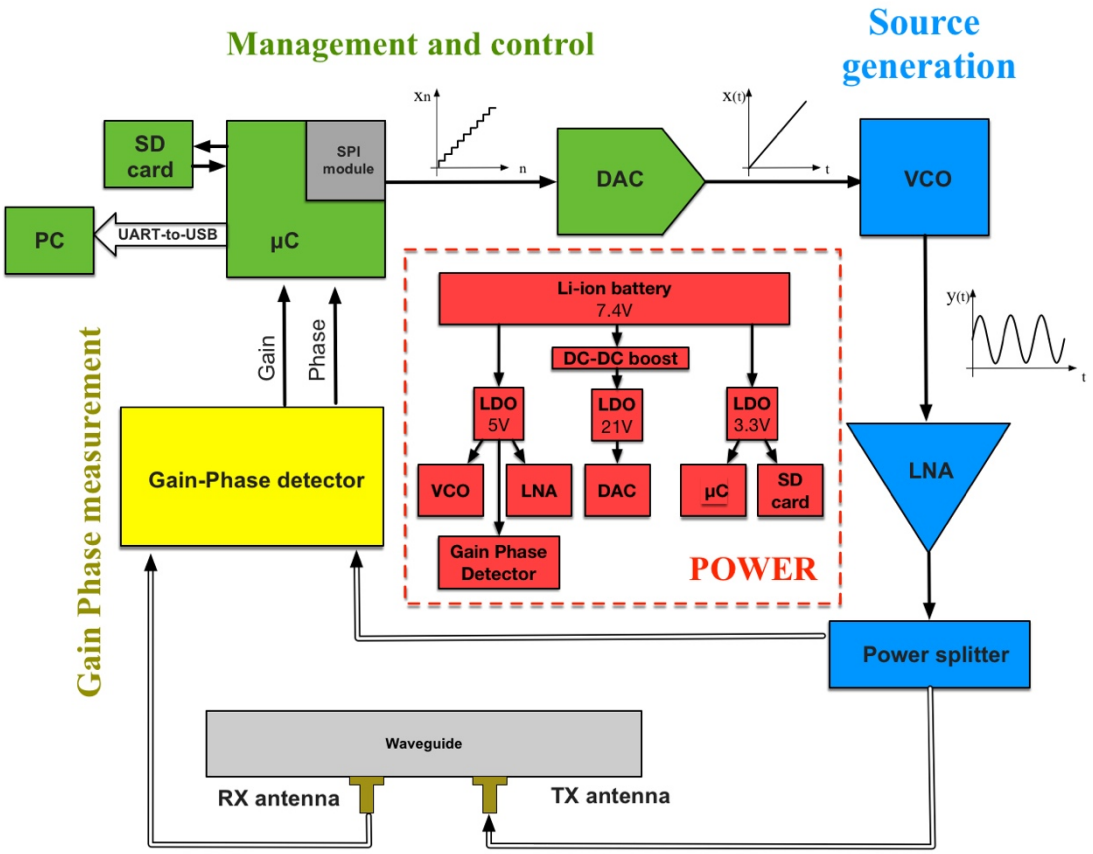

Fig. 74: Main blocks of the compact device architecture.

Subsequently, the VCO (Minicircuits ZX95-2700A+) translates the voltage ramp points into a frequency sweep of sinusoidal waves between 1.3 GHz - 2.7 GHz as the project specifications. The output power generated from the VCO is equal to 3.3 dBm which is quite low in comparison with the previous test bench set up. For this reason, a low noise amplifier (LNA) was introduced with a high gain of 20 dB in the 1.5 GHz - 3.8 GHz working range. The component chosen is an ultra-low noise RF amplifier by QORVO (TQL9092). Afterwards, the sinusoidal sweep is diverted into both the TX antenna of the waveguide and into the gain phase detector for the comparison with the received signal. To reach this goal, a power splitter equally divides the sine waves into two identical signals but with half power. When the waveform occurs in the TX antenna, the response of the soil to this excitation is captured by the RX one. The power comparison of these quantities is commissioned to the AD8302, described in section 3.2, which returns the gain and phase spectra sampled by the microcontroller. The latter converts both the signals in digital domain (12-bit ADC internal to the µC) and sends out this information using the Universal Asynchronous Receiver-Transmitter (UART) protocol. The conversion into USB protocol, for simple use with the personal computer, is given by the TTL-232R cable which, internally, embeds the FTDI FT32R chip for UART-to-USB conversion. Another implemented approach, to save the spectra, is using an SD-card to store a large amount of data. This technique is very useful when periodic acquisitions are performed such as in situ measurements. The card is internally divided into standard blocks of a fixed length equal to 512kB with a maximum capability of 256 MB. With a transfer rate of 23 MB/s in writing, it is compiled by the µC through the SPI protocol. Fig. 74 shows also the power scheme

for the ICs previously described, highlighting how the source is split into the three branches at 5 V, 21 V and 3.3 V.

To easily use the sensor device, a user-friendly interface (GUI) in Matlab is also developed. This has the double task to show/save data and to program some measurement parameters. The GUI in Fig. 75 is divided into a "Test Mode" and "Logger Mode" panels. The "Test Mode" is enabled pushing the bottom "Start", which performs a measurement plotted in the two figure boxes and saved into a text file with a timestamp information. On the other way, the "Logger Mode" allows us to select the period length in time, according to which the measurement is applied, and the timestamp (current data in day, hours, minutes, seconds) which might be lost as information when the battery is discharging. Both these operations consist in correctly programming the real-time clock (RTC) of the µC . According to the time setting for performing a measurement, an interrupt event will occur when the scheduled time has elapsed. The modalities are shown in the flowcharts (Fig. 76) of the µC programming where tasks are explained.

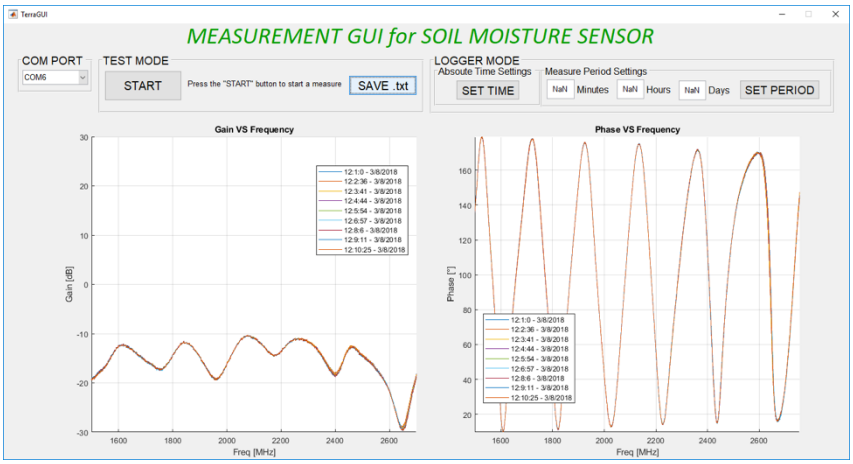

Fig. 75: Matlab GUI associated with the moisture sensor.

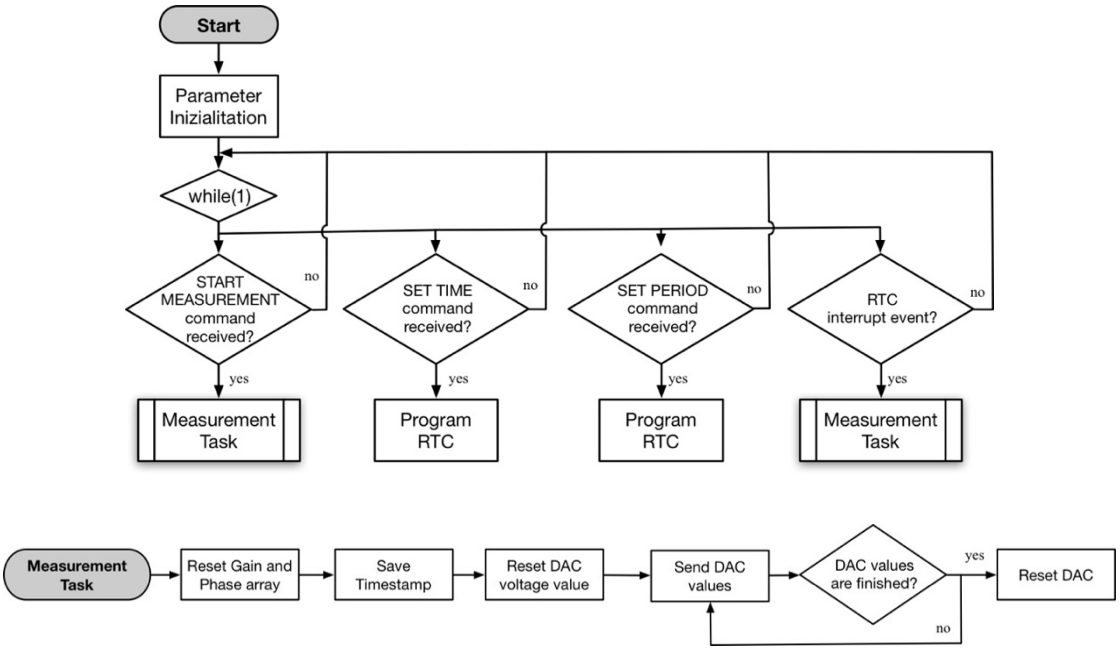

Fig. 76: Flowcharts of the microcontroller firmware.

At the present, the compact device is still under test but preliminary acquisitions are obtained using the river sand samples and applying the PLS model. In validation, the device reaches an R^2 up to 0.93 and an RMSE of 1.86 %. That values demonstrate the accurate prediction power also for the compact system developed.

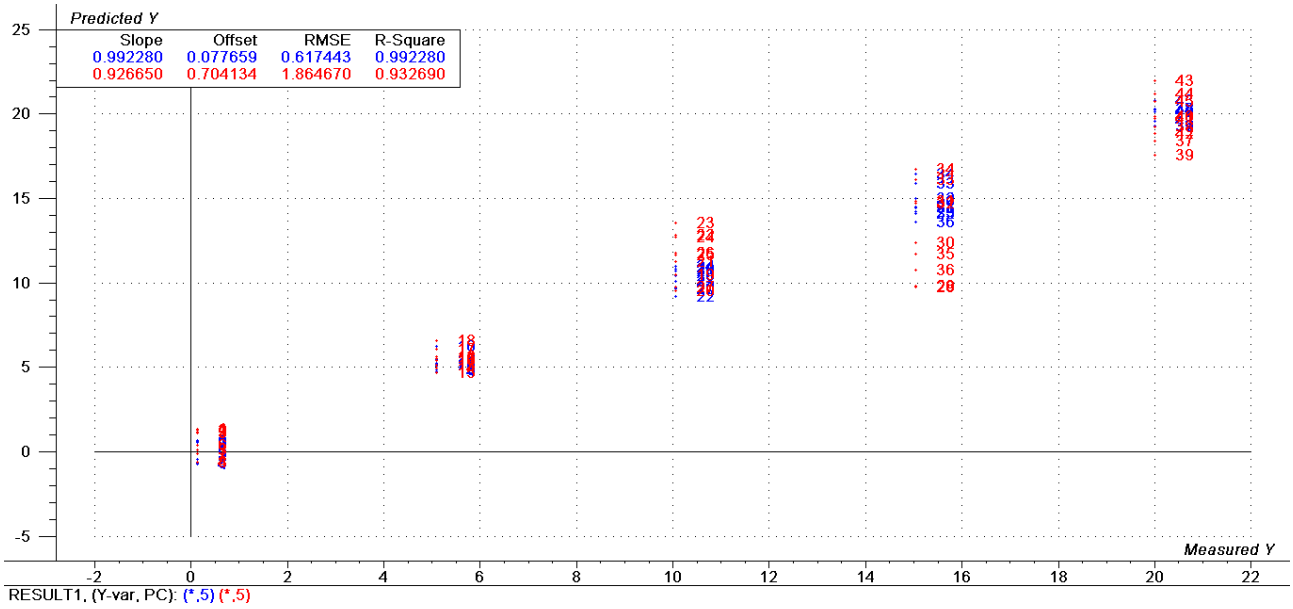

Fig. 77: Observed moisture content versus predicted (using Unscrambler software).

3.7 Alternative probe combined with K-OPLS

Maintaining the same architecture described in section 3.2, a new probe is explored to measure the soil moisture content. The working principle of this novel probe is the same of the original waveguide since TX and RX antennas are involved, but embedded in a PVC sealed pipe. The antennas used are $1/4$ of a dipole mounted on a nylon ring and placed in the pipe rotated by 90° the one towards the other, for avoiding direct coupling of EM signals from transmitting and receiving antennas [81]. The layout of the probe and the practical use is shown in Fig. 78 (a), (b) and (c). Compared to the waveguide, this probe is inserted into the soil but the moisture content is evaluated in the distributed region near the antennas overcoming the problems of the probe-soil contact failure, typical of commercial devices. An interesting upgrade of this probe is also shown in Fig. 78 (d), where different antennas could be spread along the pipe to evaluate the moisture content at different depths. Such system is tested following the previous plan described in Section 3.4, with the container filled with a uniform soil type (not stratified modality), among river sand, LECA and silty clay loam while investigating a frequency range of 1 GHz - 2.7 GHz.

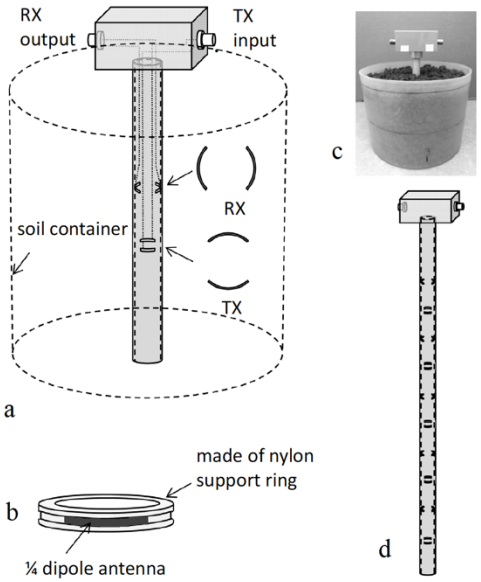

Fig. 78: New probe manufacture [81].

To investigate the non-linear behaviours of the system, the K-OPLS analysis (Section 3.3.3) is used and compared with the classical PLS as in Table 9. The score plot for the river sand sample is shown in Fig. 79(a) where the K-OPLS model is characterized by only one predictive PLS component since it is sufficient to discriminate the moisture content. The predictive score vector represents the hydration discriminatory direction while the score associated with the PC of the dependent variable collects systematic and linearly independent variations. The predicted versus observed values of the moisture content (river sand, gain) in Fig. 79 (b) shows a very good prediction with an R^2 value up to 0.988 and an RMSE of 0.7 %.

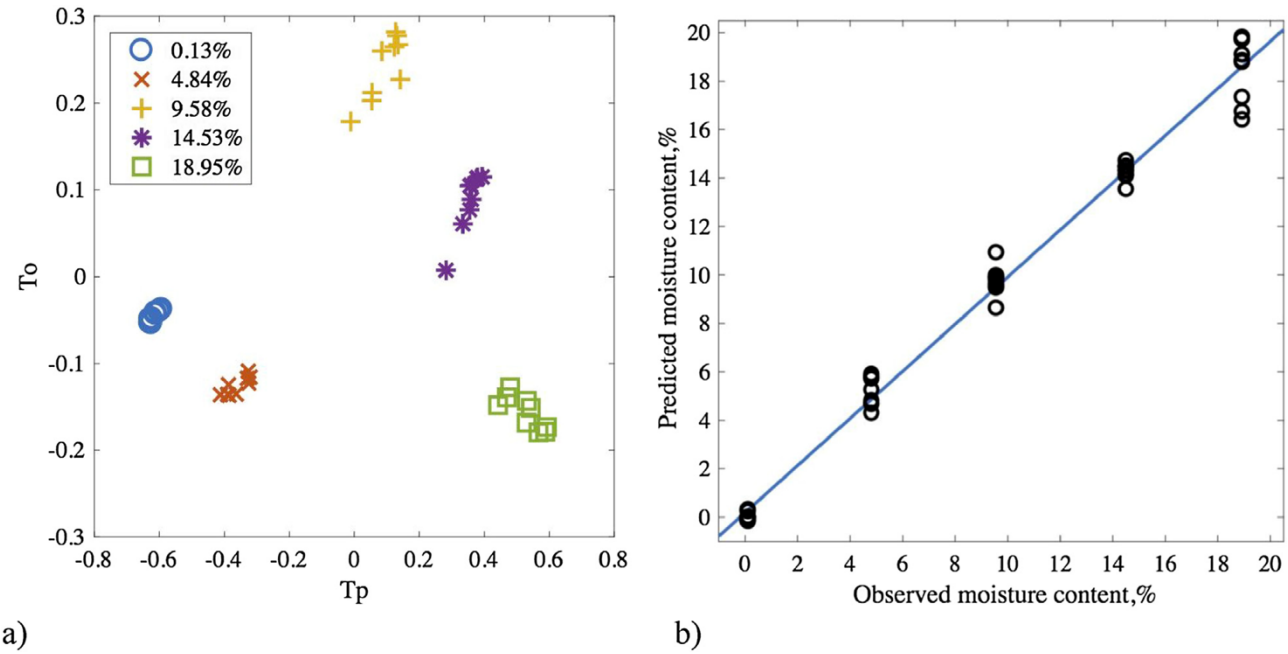

Fig. 79: K-OPLS predictive score vector Tp against first Y-orthogonal score vector To; b) predicted versus observed values of the moisture content (%) for river sand gain spectra (K-OPLS, R2= 0.988, RMSE = 0.7 %) [81].

The potentiality of the K-OPLS manifests when a unique model, collecting the various soil types, is built (R^2=0.971 and RMSE=1.4 % for the gain), meaning that the a priori knowledge of soil composition is unnecessary. Therefore, the optimal R^2 and RMSE values for the total model (Silty clay loam + river sand + LECA) make this system capable of predicting the moisture content without a previous soil calibration and also ignoring soil composition, texture, density and other chemical and physical properties. The excellent obtained performances are also stressed in order to evaluate the influence of the temperature (2 ° and 22 °) on the gain and phase spectra (Fig. 80). The figure shows shifts in the waveforms in the range 1.18 GHz -1.28 GHz and more than 1.3 GHz, due to the dependence of the loss factor and of dielectric constant on the temperature. However, the temperature can be modelled as a further dependent variable, in addition to the moisture content, for the prediction model to improve the accuracy of the result.

Table 9: Comparison of PLS and K-OPLS analysis for the new probe [81].

PLS and K-OPLS regression analysis for the prediction of soil moisture content.

Soil	Parameter	Frequency range (GHz)	PLS			K-OPLS				
			PLScomp	R^2	RMSE	σ	PLScomp	ORTHcomp	R^2	RMSE
Silty clay loam	Gain	1.10–1.36	6	0.970	1.4	1.0	1	3	0.964	1.5
	Phase	1.10–1.36	4	0.980	1.1	0.9	1	3	0.867	2.3
River sand	Gain	1.10–1.36	2	0.960	1.4	0.9	1	2	0.988	0.7
	Phase	1.10–1.36	5	0.983	0.9	1.0	1	4	0.851	2.0
LECA	Gain	1.10–1.36	1	0.975	1.6	0.5	1	1	0.970	1.7
	Phase	1.10–1.36	6	0.981	1.4	0.9	1	4	0.946	2.2
Silty clay loam + river sand + LECA	Gain	1.10–1.36	9	0.513	6.1	0.8	1	7	0.971	1.4
	Phase	1.10–1.36	10	0.553	5.8	1.0	1	8	0.909	1.6

Legend: PLScomp, number of PLS components; RMSE, root mean square error; ORTHcomp, number of orthogonal components.

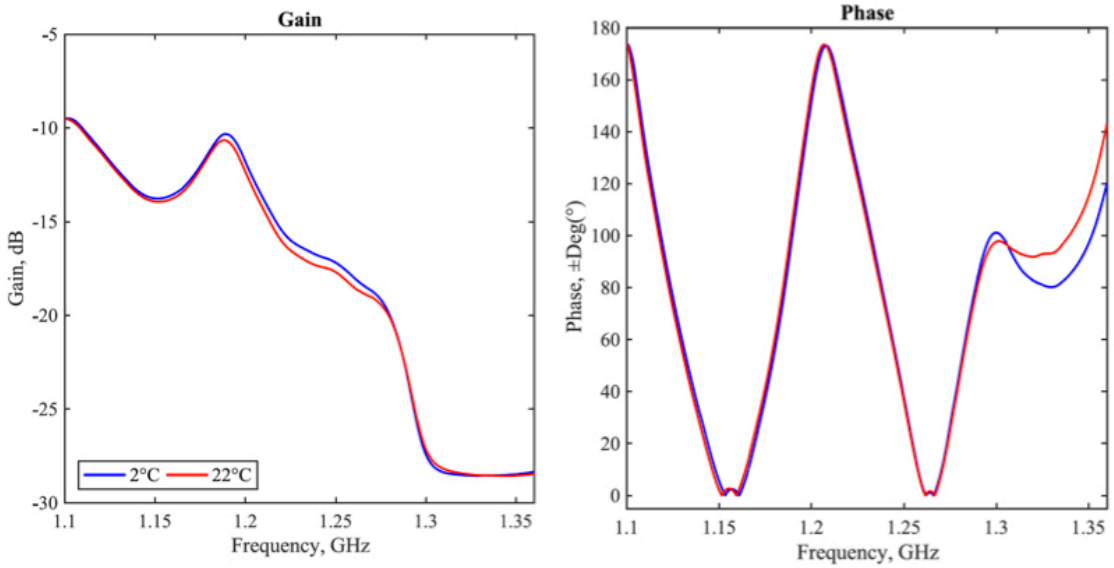

Fig. 80: Variations of spectral acquisitions depending on temperature [81].

3.8 Project relevance in thesis topic

The project described shows not only a new approach for investigating soil moisture content, but it can be assumed as a strategy for the elaboration of the impedance spectra. The IS typically collects a lot of data which contain the information we want to isolate, such as when using power mismatch to investigate the moisture content. Focusing the attention on the information extrapolation, the statistical tools are powerful prediction techniques which can be applied in a lot of applications specially in those environments influenced by different variables. This is the typical situation of any sensor node, which does not live in a controlled environment but it is subject to many changes around it. For example, let us think about a wearable sensor with electrodes for monitoring the vital parameters of a subject. The measurement can be influenced by a lot of disturbances such motion artefacts, insufficient adhesion of the electrodes, unwanted physical or chemical variables, and so on.
The same conclusions can be also drawn for the moisture sensor described, which might be influenced by weather conditions, temperature, soil conductivity and composition and so on. The statistical model, therefore, can help in detecting only the information of interest improving the accuracy of the measurement itself. For this reason, the PCA, PLS methods and its variants are fundamental techniques regardless of the nature of the impedance (electrical, power comparison) and of the applications. The high prediction power of the PLS for the non-invasive probe is supported by R^2 values more than 0.934 with the best case of 0.989 (river sand, gain) and by RMSE up to 0.8 % (river sand, gain). In general, we can assess that the best performances belong to the river sand sample while less accuracy is appreciable for the silty clay loam mainly due to some swell phenomena at high moisture content values. For all types of soil the prediction quality is improved by the application of the N-PLS model which combines together absolute and phase to a unique model. The best results are shown for the LECA sample with an R^2 value of 0.991 and RMSE equal to 0.9 %.
Moreover, by considering the non-linearity effects for the alternative probe, a non-linear K-OPLS model, including all types of soil, is compared with PLS one where we can highlight an amazing upgrade for the R^2 moving from 0.513 to 0.971 and for the RMSE from 6.1 % to 1.4 %.
All these excellent results can be associated with the fact that the statistical models can be calculated offline and only the predictive parameters, generated from it, can be added into the device. In this way, these coefficients will be combined with each new spectrum acquisition to predict the moisture content. Moving the model elaboration offline means that the computation weight is lightened and, therefore, the power consumptions are reduced as the IoT requires. In conclusion, we can successfully join these tools with the new emerging sensor architectures in order to ignore the high variability of the environments surrounding the sensor and to easily predict the desired information.

Chapter 4: Technical and implementation strategies for low-power IS system.

Novel technical and implementation strategies are introduced to overcome two main problems of the classical sine-based technique which are: the wide measurement time, to cover a range of frequencies, and the implementation which mainly involves analog blocks weighting on the power consumption. This means that, in the perspective of the modern sensor concept as the IoT, they are not perfectly suitable but other techniques can be explored with the aim of getting a fast measurement and a low-power implementation while maintaining high accuracy. The measurement time can be made instant with the impulse excitation, but it can generate non-linearity phenomena due to the wide amplitude of the signal. For these reasons, alternative methods are applied such as the random-like signals, which cover a wide range of frequencies in one-shot. The implementations are consequently related to the nature of the random stimulus, which can be a white noise, a multi-sine combination or a pseudo-random sequence (PRS). In particular a PRS can be built with binary elements (PRBS), embeddable in an almost-digital architecture and reaching low-power performances. Also the impedance extraction can get benefits from the PRBS, since a time-domain elaboration and a direct frequency processing, described in the following sections, are applicable. The frequency information can also be extracted by the time-domain though the application of a Fast Fourier Transform (FFT), for which many efficient implementation schemes are known. The following sections will describe a PRBS-based technique and two methods for inferring the impedance, respectively in time and directly in frequency domain. Both algorithms (time and frequency domain) are proposed with emphasis on the strategies chosen and on the elaboration algorithms implemented into the digital ultra-low power platform GAP8 described in Section 4.5. The comparison between the proposed systems is performed in term of power consumption and processing time with the aim to identify the suitable technique to be embedded in low-power sensors.

To conclude this chapter, we show a possible application, which is related to the development of a wearable device, where low power budget is significant for improving the life-time of the sensor. Towards this perspective, we describe a possible analog interface and the printable electrodes particularly suitable in the wearable technology. The combination of the analog part with the novel electrodes allows the non-invasive sensing on skin, from which different parameters can be extracted: from the sweat composition to the detection of skin diseases like cancer.

4.1 PRBS for time-domain impedance investigation

As described in section 1.5.4, the random signal $x(t)$ has the advantage to be represented by an autocorrelation function $R_x(\tau)$, which is approximately a Dirac's delta:

$$R_x(\tau) = x(t) * x(-t) \approx E_x \delta(t) \tag{4.1}$$

where E_x is the energy of the signal and $x(-t)$ is the time reversed signal. Defining the output of the system as $y(t)$, we can obtain the impulse response by a convolution with the time-reversed signal as follows:

$$y(t) * x(-t) = h(t) * x(t) * x(-t) \approx E_x h(t) \tag{4.2}$$

Since there is a duality between the impulse response and the impedance behaviour in time, as described in section 1.5.1, we can assume that the impedance is inferred with a single convolution operation. If we generalize the property in Eq. (4.1), we can find a signal $x_{inv}(t)$, which satisfies the relation:

$$x(t) * x_{inv}(t) \approx \delta(t) \tag{4.3}$$

The above equation can be moved in frequency domain expressed as:

$$X(j\omega) X_{inv}(j\omega) \approx 1 \tag{4.4}$$

This means that to obtain the $x_{inv}(t)$, an inverse Fourier Transform $\mathcal{F}^{-1}$ can be applied to the following relation:

$$x_{inv}(t) = \mathcal{F}^{-1}(X_{inv}(j\omega)) = \mathcal{F}^{-1}(1 / X(j\omega)) \tag{4.5}$$

In this way, the impedance is obtained by simply convolving the $x_{inv}(t)$ with the output:

$$y(t) * x_{inv}(t) = h(t) * x(t) * x_{inv}(t) \approx h(t) \tag{4.6}$$

Such impedance has the advantage to be implemented using a simple convolution operation, which involves sums and multiplications and, therefore, very suitable in digital architecture. To discover the further implementation benefits of this technique, we need to describe how the random signal can be produced. Since the signals are not treated as continuous from an implementation point of view, we move into the discrete domain where signals are considered vectors of fixed elements. The random signal can be therefore defined as a sequence x_n with $(n = 0,...,N-1)$, and the convolution, involving the convolutional inverse x_n^{inv}, becomes a cyclic convolution as follows:

$$x_n^{inv} \circledast x_n = \sum_{k=0}^{N-1} x_k^{inv} x_{(n-k) \bmod N} = \delta_n \tag{4.7}$$

where *mod* is the modulo operator (signed remainder after division). In order to perform the cyclic convolution easily, also for the implementation purposes, we can apply the linear convolution but repeating the sequence x_n for K times. The unwrapping of the cyclic convolution into the linear, performed between a main sequence and a folded one, is represented in Fig. 81:

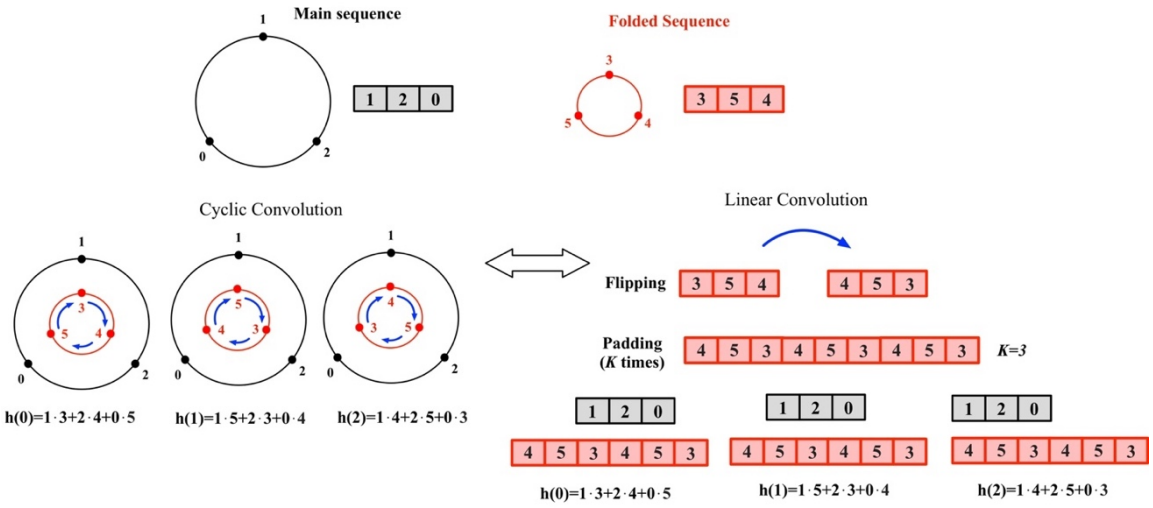

Fig. 81: Cyclic convolution explication into the linear.

Fig. 81 shows that the same results can be drawn regardless of the method used (convolution or linear). To get this, the linear convolution flips the folded sequence and adds a padding by concatenating the vector (minimum 3 times to avoid edge effects). When such translation in linear convolution is applied to the Eq. (4.2), the $x(t)$ is twice inverted (one time to get the $x(-t)$ and the other for the flipping in Fig. 81), this allows to identify the convolution $y(t)*x(-t)$ as a FIR filter operation. As regards the padding (Fig. 81), we can build a single random pattern and repeat it, obtaining a sequence represented as follows:

$$\bar{x}_n = \sum_{k=0}^{K-1} x_{(n-kN) \bmod N} \qquad n \in \mathbb{Z} \tag{4.8}$$

As a random signal, x_n can be chosen among different possibilities [82]:

- PRBS obtained by randomly generating the binary elements {0,1} from a uniform discrete distribution. With this choice, we need to refer to the Eq. (4.6) where a general inverted input is considered x_n^{inv}, obtained as:

$$x_n^{inv} = IDFT(DFT(x_0,...,x_{N-1})) \tag{4.9}$$

  Although the PRBS is binary, therefore representable in digital domain, the inverted version should be calculated by applying an Inverse Discrete Fourier Transform (IDFT) and a direct one (DFT) which means that it will not still binary.

- PRBS built from random phases $\varphi_0,...,\varphi_{N-1} \in [0,2\pi]$ used to construct the vector $X_n = (e^{j\varphi_0},..,e^{j\varphi_{N-1}})$ from which we can infer the exciting signal x_n by an IDFT.

The advantage of this method is that the inverted sequence x_n^{inv}corresponds to the time-reversed version ($x(-t)$ in continuous domain) with real values (by imposing the Hermitian symmetry), therefore we can use the same sequence as system input and for the impedance processing. However, we lost the benefits originated from the binary property.

- A specific sub-class of the PRBS, called Maximum Length Sequences (MLS), are binary vectors generated recursively using a series of digital shift registers with selected XOR feedback [83]. The number of shift registers represents the order of the sequence expressed as: $2^N - 1$. The antipodal ± 1 version of this sequence plus the constant $z = 1/(2^{N/2}+1)$ has a constant modulus DFT, so again the cyclic inverse is the time reversed sequence. The further benefit, respect to the previous choice, relies on the fact that the input sequence and, therefore, the time-inverted are binary. This means that the MLS in input can be easily generated or stored in a digital architecture while sending with even a 1-bit DAC; moreover, the processing will be lightened by convolving with the binary sequence. A drawback is related to the length of the sequence as a power of 2, which can be tricky when applying, for example, the FFT. However, such disadvantage is considered reasonable and easily surmountable padding the sequence with one value. Another critical point is due to the fact that, in order to obtain an MLS with constant modulus, the binary elements should be subtracted for the constant z, meaning that the MLS has a no-zero offset. The presence of such DC value can represent a problem when the MLS is used to excite through electrodes a biological tissue, such as the skin, where the DC can produce the electrode oxidation. Nevertheless, when the order of the MLS is high, the z value is very small and, therefore, negligible.

Since the MLS collects more advantages, we consider it the best choice among PRB sequences. The statistical properties describing such signal are represented in Fig. 82.

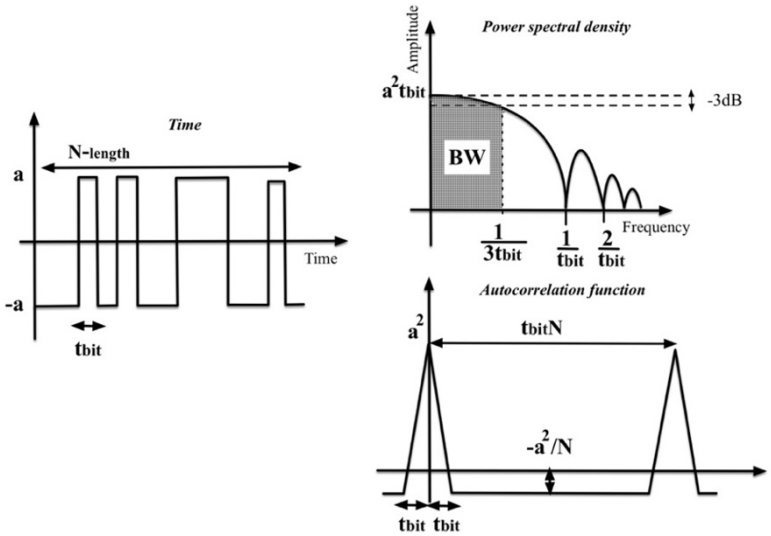

Fig. 82: MLS representation in time and through statistical properties.

The bit-time defined as the time occurring while sending a bit is represented as t_{bit} and it influences also where the power density lobes are falling. Moreover, observing the power spectral density, we can assume that the uniform stimulation ends when the power density falls by 3dB, from which we can derive the stimulation bandwidth (BW) at $1/3t_{bit}$ [84].

4.2 MLS for direct frequency-domain impedance investigation

In addition to the time-domain technique, widely described, it is possible to investigate directly the impedance spectrum in a very efficient way, when the constant modulus MLS is chosen as stimulus. Starting from the time-domain discussion, the impedance can be explored by applying the following formula:

$$h(t) = y(t) * x(-t) \tag{4.10}$$

The above equation can be moved into the frequency domain by applying the FFTs on the response ($Y(f)$) and on the inverted excitation ($\bar{X}(f) = \mathcal{F}(x(-t))$). The relationship between the two quantities becomes:

$$H(f) = Y(f) \bullet \bar{X}(f) \tag{4.11}$$

Splitting the complex equation into the modulus and phase parameters, we get:

$$\begin{aligned} |H(f)| &= |Y(f)| \bullet |\bar{X}(f)| = |Y(f)| \bullet \alpha \\ \langle H(f) &= \langle Y(f) - \langle \bar{X}(f) \end{aligned} \tag{4.12}$$

Because the $\bar{X}(f)$ is the Fourier Transform of an MLS signal, we can assume a constant spectrum (equal to α) as described in Fig. 82 by the BW. Therefore, the modulus of the impedance spectrum $|H(f)|$ is equal to the spectrum of the output $|Y(f)|$ except for the α parameter. On the other hand, the phase information $\langle H(f)$ is brought back to the subtraction respectively between the phase of the response and the phase of the inverted stimulus. From an implementation point of view, the most expensive operations are the FFTs since they are followed by a multiplication for a constant factor and a subtraction (Eq. (4.12)). However, since the reversed input $x(-t)$ is always known a priori and used as excitation when desired, this FFT can be calculated offline only once and the parameters α and $\langle \bar{X}(f)$ can be stored. This is valid also if the technique is implemented in an ultra-low power platform as the GAP8, whose processing algorithm has a computational complexity given above all by one FFT computation and phase subtraction. Taking in consideration the previous implementation with 16,384 samples, the FFT (radix-2 DIT) involves 780k instructions which will be added to 16,384 subtractions, therefore, the computational budget amounts about to 800k instructions. However, this estimation does not coincide exactly with the number of cycles, which involves further cycles necessary to the architecture for performing the operations. In particular, the previous time-domain technique can work among integer data which are the PRBS sequence and the response which can be quantized. The convolution between these integer data is still representable by integers. On the other hand, in the direct frequency method, the absolute value $|Y(f)|$ cannot be an integer as also the $\langle Y(f)$, the $\langle \bar{X}(f)$ and their subtraction. In fact, the complex phases can assume any value, especially for $\langle Y(f)$ which strongly depends on the device under test. For this reason, a floating point or a fixed-point data implementation is suggested. The floating-point method guarantees a high accuracy but at the expense of computational costs when the subtraction between floating is applied. Moreover, the architecture will need a floating-point unit (FPU), therefore GAP8 will be unsuitable. On the other side, fixed point data are interpreted as integer by any

architecture, thus not adding complexity on the computation. However, phase displacements can be very small in size, which can difficulty be appreciated with a fixed-point approximation. A preliminary test in Matlab was performed to test the working principle of the method applied to an RLC circuit $\left(\frac{5\cdot10^{11}}{n^2+2.5\cdot10^5 n+5\cdot10^{11}}\right)$ shown in Fig. 83. The frequency method is digitally implemented in GAP8 and compared to the time-domain version in term of power consumption and processing time.

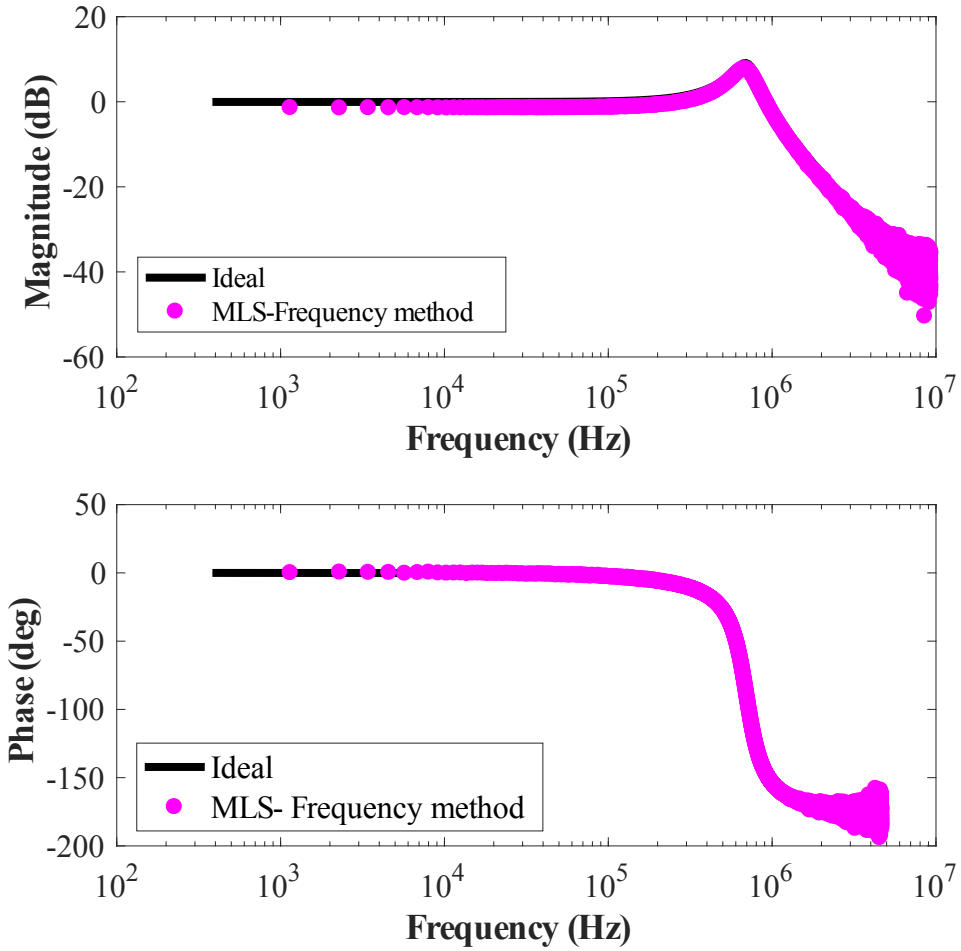

Fig. 83: Impedance spectrum in magnitude and phase for an RLC circuit with MLS-Frequency method.

4.3 Implementation strategies for time-domain and frequency-domain algorithms

In the previous chapter we suggested some preliminary advices useful during the implementations, such as the linear convolution (opposed to the cyclic) in time-domain algorithm and the MLS as preferable excitation for both methods. To get the full control of the system, and to optimize it for a low-power consumption, we need to describe in deep all the blocks involved in the impedance measurement systems as in Fig. 84.

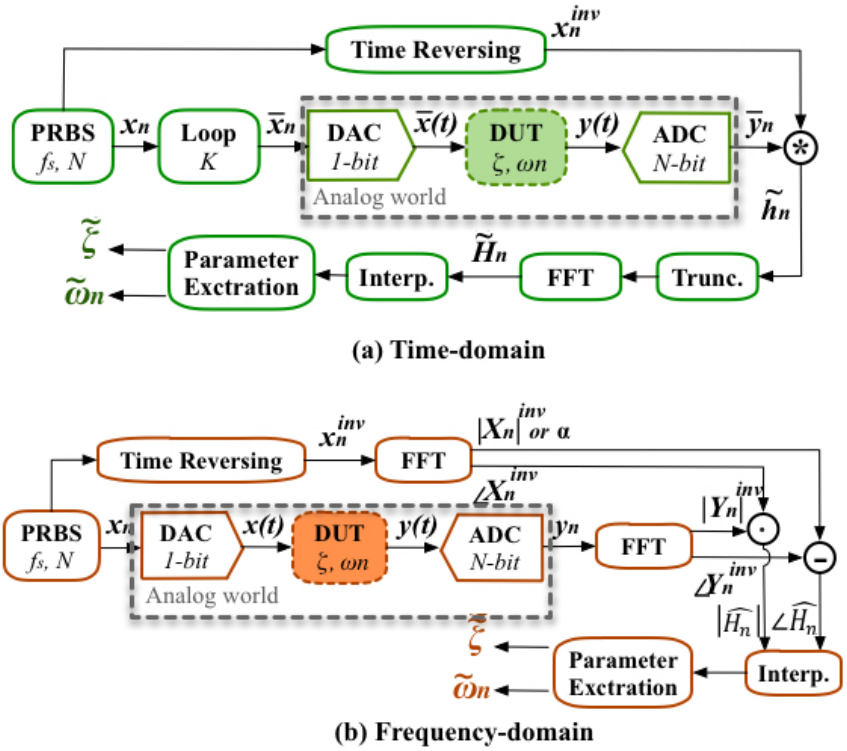

Fig. 84: Block scheme of the impedance measurement systems.

Starting from the time-domain implementation (Fig. 84 a), the MLS is defined by the PRBS sequence of length N and the bit frequency f_{bit} (related to the t_{bit} in Fig. 82 through: $f_{bit} = 1/t_{bit}$). This pattern must be concatenated (Loop block) for repeating the sequence in order to later apply a linear convolution instead of a cyclic one. Thanks to the binary nature of the MLS, a digital-to-analog converter (DAC) with 1-bit resolution is enough to send out the excitation which will cross a device under test (DUT). When the interaction between MLS and DUT occurs, we move in the analog domain where the signals can be represented in continuous time. The response of the system to this excitation, can be therefore expressed as:

$$y(t) = h(t) * \bar{x}(t) \tag{4.13}$$

We note that, since $\bar{x}(t)$ is a repeated sequence, therefore, also the output $y(t)$ is repeated too.

At this point, to process the impedance in time $h(t)$ we need to return into digital domain using an analog-to-digital converter (ADC) with N-bit resolution. The linear convolution between x_n^{inv} and the discrete repeated response $\bar{y}_n$ produces the discrete repetition of the $h(t)$, defined as discrete with $\tilde{h}_n$ in Fig. 84 a. To extract

only one repetition, remembering also that the linear convolution generates edge effects, the signal is truncated and, if desired, it can be moved in frequency domain using an FFT.

On the other hand, the frequency-domain implementation (Fig. 84 b) directly sends the PRBS to the DUT through the 1-bit DAC since no direct convolution is applied and no edge effects are considered. The DUT response, sampled and quantized by the ADC block, is moved into the frequency domain through the FFT and compared with the FFT of the reversed input signal. The comparison performed in term of absolute values and phase subtractions are interpolated and analysed to extract the DUT parameters.

In both implementations, some block parameters in common plays a significant rule for the result accuracy. Before deciding them, we should know the time constants of the DUT, in particular the biggest τ involved is essential to calibrate the f_{bit}. Following the Nyquist-Shannon sampling theorem, in fact, the frequency bit should be at least equal to the double of $1/\tau$, moreover it should match the f_{ADC} and f_{DAC} ($f_{bit} = f_{DAC} = f_{ADC}$) to correctly sample the data.

With these assumptions, the impedance spectrum will be reconstructed with a frequency resolution of $f_{res} = f_{bit} / N$, which corresponds to the minimum frequency detected, while the maximum frequency is $f_{\max} = f_{bit} / 2$.

In order to evaluate the influence of the system parameters to the accuracy of the impedance estimation, we assume a second order under-dumped system (RLC parallel) as DUT, with the following transfer function:

$$\frac{\omega_n^2}{n^2 + 2\zeta\omega_n n + \omega_n^2} = \frac{5\cdot 10^{11}}{n^2 + 2.5\cdot 10^5 n + 5\cdot 10^{11}} \tag{4.14}$$

where ω_n is the natural frequency and ζ is the damping factor, while the biggest time constant is 8μs ($1/(\zeta\omega_n)$). Such constant can be detected from the impulse response (Fig. 85 b) by the envelope, of the under-damped response, which is equal to the decay of an RC circuit (Fig. 85 a). From this figure, we can infer that after 5τ the response is completely exhausted. This assessment is fundamental in the choice of the sequence length, since it should cover the exhaustion of the response in accordance with the biggest time constant and the frequency bit with the following relation:

$$N \geq 5\tau f_{bit} \tag{4.15}$$

Following the strict relation of the Eq. (4.15), we get the minimum number of points to correctly reconstruct the impulse response, while using more points will assure a better accuracy. The same discussion can be drawn for the choice of the f_{bit}, which has to be at least the double of the excitation band but, increasing the value, the accuracy will improve (we suggest choosing at least 4-times the bound level). Moreover, only for time-domain algorithm, the excitation must be concatenated in the Loop block at least 3 times ($K \geq 3$) considering that the edge effects, produced by the linear convolution operation, are confined in the marginal repetitions. On the other hand, many repetitions can be applied to obtain repeated impulse responses, which can be averaged for improving signal-to-noise ratio.

Once we have set the parameters, the measurement time can be estimated as $t_{meas} = N / f_{bit}$.

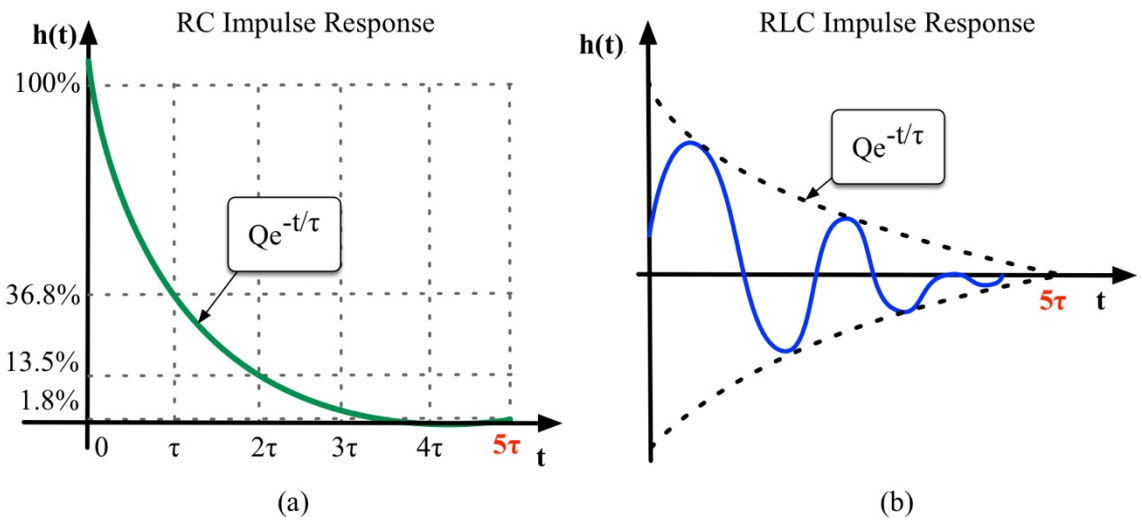

Fig. 85: Impulse response of an RC and RLC circuits with emphasis on time constants.

The algorithm steps for the choice of the parameters are summarized as in Fig. 86:

Set Parameters

1: Identify the excitation band of the DUT and the biggest time constant: **BW, τ.**

2: Set the f_{bit} at more than 3 times: $f_{bit} \geq 3BW$

3: Set the length of the sequence: $N \geq 5\tau f_{bit}$

4: Repeat the sequence at least 3 times: $K \geq 3$

5: The measurement time is $t_{meas} = NK/f_{bit}$.

Fig. 86: Procedure to correctly set the parameters to apply the PRBS-time domain algorithm.

A comparison among the ideal TF and the results obtained by a good and bad choices of parameters are evaluated for the under-dumped system (Eq. (4.14)) and shown in Fig. 87. Since in the good setting accuracy can be improved by increasing the bit frequency or the length of the MLS sequence, a study about the relations of these with the accuracy was conducted in Matlab. As comparison criterion we chose the percentage of errors, associated with ω_n and ζ deducted by the TF recontruction:

$$\%err_{\zeta} = \frac{100\left|\zeta - \tilde{\zeta}\right|}{\zeta} \qquad \%err_{\omega_n} = \frac{100\left|\omega_n - \tilde{\omega}_n\right|}{\omega_n} \tag{4.16}$$

where $\tilde{\zeta}$ and $\tilde{\omega}_n$ are the estimated ones.

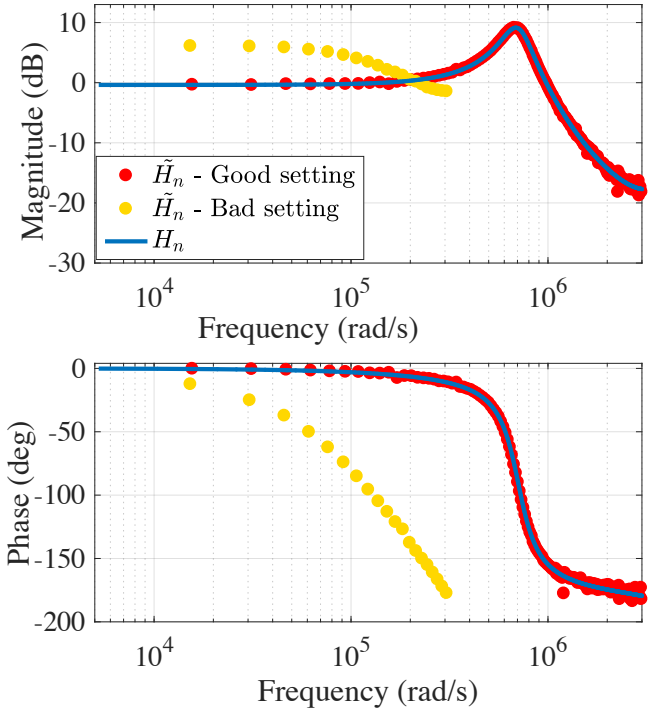

Fig. 87: Comparison between good and bad setting of parameters for an under-dumped system.

The dependence of f_{bit} and N to the $\%err_\zeta$ is represented by the surface plot in the next figure.

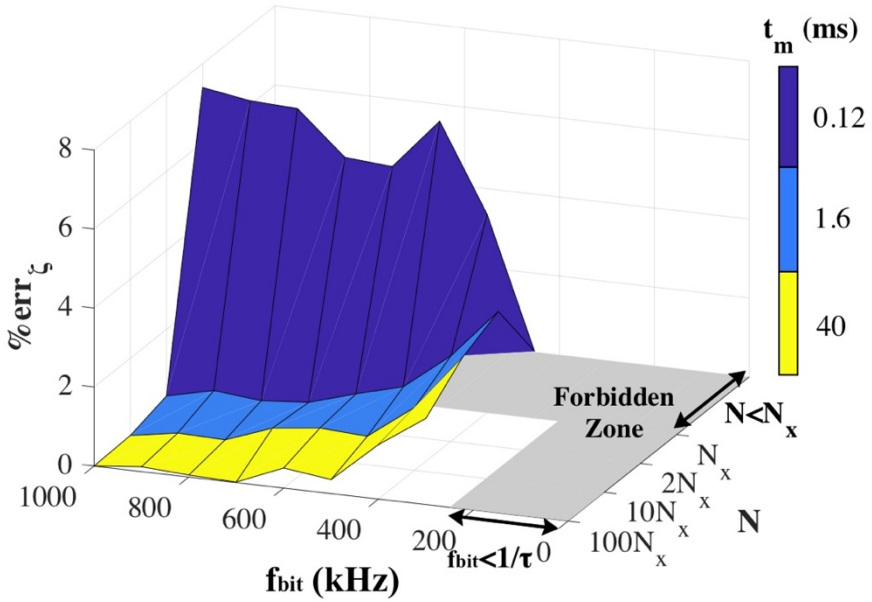

Fig. 88: Dependency of the bit frequency and MLS length on the error related to the damped factor.

The above study, applied for time-domain but extendable to the frequency method, assumes that $K = 3$ and the bit resolution of the ADC is 8, since it was demonstrated that this resolution does not influence the accuracy too much. Fig. 88 shows a forbidden zone, which does not satisfy the good parameter setting and the TF is not

well reconstructed. On the other hand, it becomes clear that, increasing f_{bit} or N, the $\%err_{\zeta}$ decreases less than 1% while the measurement is performed in 40 ms (time-domain). However, if we choose N minimum we boost the measurement time up to 120 μs while meeting an average error around the 8 % which can be also reasonable in some applications.

As a general rule, the trade-off between f_{bit} and N, taking also into consideration the measurement time, should avoid excesses which should require more stringent hardware requirements and heavy processing. Therefore, the previous description has to be interpreted as a guideline for the user to set the parameters in order to save computations and time. Based on the accuracy desired, in fact, it is possible to calibrate such quantities in order to get a soft implementation.

The same conclusions in Fig. 88 can be also drawn for the dependence of $N$and f_{bit} on $\%err_{\omega_n}$.

4.4 Algorithm strategies

What stands out from the system description in Fig. 84, is that both algorithms are mainly made up by a convolution operation and a Fourier Transform. Implementing these two elaborations in a digital architecture is not obvious if we want to keep the computation and power consumptions reduced. In this chapter we will illustrate some implementation choices suitable for any processing unit as long as they respect the requirements illustrated. In the next section 4.5, a specific ultra-low power platform will be introduced with further optimizations exploiting the platform potentiality.

4.4.1 Convolution with Fast Hadamard Transform

The heart of the time-domain algorithm relies on the convolution operation. It can be assumed as the only essential processing applicable to get the impedance information in the time-domain collecting as much information as the frequency spectrum. Therefore, if module and phase are not necessary, the time-domain impedance can be used to assess some characteristics from the DUT. Although the linear convolution involves only sums and multiplications (Fig. 81), it can be a heavy processing if the lengths of vectors involved are large. Let us assume to apply a convolution between two vectors with the same length N, the number of operations computed are N^2 MAC (multiply accumulator) operations. For example, this means that, if we want a wide and dense spectrum of $(2^{14}-1)$ points, they should be the length of the MLS and, consequently, the length of the response by the DUT. The convolution operation between these two sequences will include:

$$(2^{14}-1)\bullet(2^{14}-1)=16{,}383\bullet16{,}383=268{,}402{,}689=268\bullet10^{6}\,MAC \tag{4.17}$$

Computing more than 268 million of MAC operations can be time-consuming and it should be performed in an efficient way aligning with low power requirements. For these reasons, we can decide to use a fast algorithm to improve the performance, such as the Fast M-Transform (FMT).

The FMT can be applied only to the MLS sequences and it consists of two vector permutations and a fast Hadamard Transform (FHT).

Starting from the problem formulation, we want to perform the convolution between:

$$y_n * x_n^{inv} = h_n \tag{4.18}$$

where x_n^{inv} is the reversed time version of the input signal. The above equation can be interpreted as a deconvolution operation from $x_n * h_n = y_n$ to get the impulse response [85]. In matrix form, the deconvolution can be expressed as in (4.19).

$$\begin{bmatrix} h_1 \\ h_2 \\ h_3 \\ h_4 \\ h_5 \\ h_6 \\ h_7 \end{bmatrix} = \begin{bmatrix} x_1 & x_2 & x_3 & x_4 & x_5 & x_6 & x_7 \\ x_2 & x_3 & x_4 & x_5 & x_6 & x_7 & x_1 \\ x_3 & x_4 & x_5 & x_6 & x_7 & x_1 & x_2 \\ x_4 & x_5 & x_6 & x_7 & x_1 & x_2 & x_3 \\ x_5 & x_6 & x_7 & x_1 & x_2 & x_3 & x_4 \\ x_6 & x_7 & x_1 & x_2 & x_3 & x_4 & x_5 \\ x_7 & x_1 & x_2 & x_3 & x_4 & x_5 & x_6 \end{bmatrix} \bullet \begin{bmatrix} y_1 \\ y_2 \\ y_3 \\ y_4 \\ y_5 \\ y_6 \\ y_7 \end{bmatrix} \tag{4.19}$$

where the x_i elements can be ± 1 as the MLS theory. Before applying the fast algorithm, it is necessary to map the values into 0 and +1 following the relations:

$$\begin{aligned} 0 &\Leftrightarrow +1 \\ 1 &\Leftrightarrow -1 \end{aligned} \tag{4.20}$$

The matrix obtained by the mapped x_i elements ($P \times P$), known as M-matrix, is symmetric and satisfies a recursion formula for both columns and rows. Therefore, every row (or columns) of M can be expressed as a linear, modulo-two combination of the first K rows through the matrixes L ($P \times N$) and S ($N \times P$) where N is the order of the MLS sequence ($2^N - 1$ elements) :

$$M = LS = S'L' \tag{4.21}$$

The S matrix can be built by the first N rows of M, while the L contains a square identity matrix of N elements and can be calculated by the relation:

$$L = S'\sigma^{-1} \tag{4.22}$$

Where σ^{-1} is the inverted matrix which contains the first N columns of S. The above factorization is described in Fig. 89.

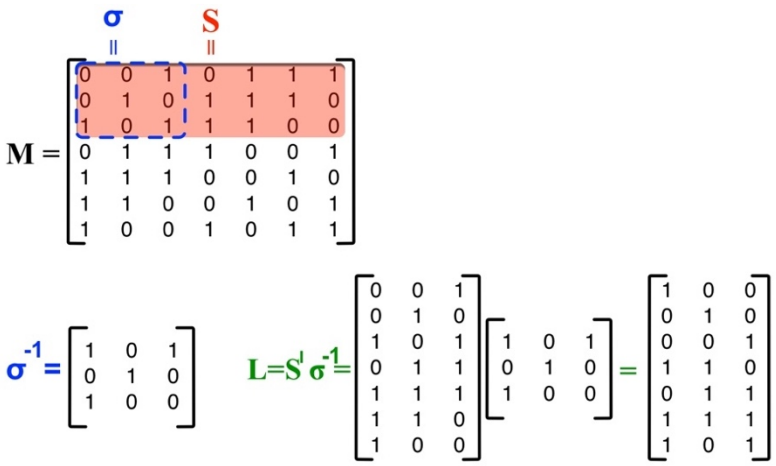

Fig. 89: Factorization of the M-matrix.

Once identified the factorization of the M matrix, we can introduce the Hadamard matrix (H) which can be mathematically returned into the M. The H matrix, in fact, has a zero row and zero column bordering to the left and top of M producing an H matrix with size $(P+1)\times(P+1)$ [85]. Moreover, as the M-matrix, H can be factored by means of the matrix B as follows:

$$H = \begin{bmatrix} 0 & 0 & 0 & 0 & 0 & 0 & 0 & 0 \\ 0 & x_1 & x_2 & x_3 & x_4 & x_5 & x_6 & x_7 \\ 0 & x_2 & x_3 & x_4 & x_5 & x_6 & x_7 & x_1 \\ 0 & x_3 & x_4 & x_5 & x_6 & x_7 & x_1 & x_2 \\ 0 & x_4 & x_5 & x_6 & x_7 & x_1 & x_2 & x_3 \\ 0 & x_5 & x_6 & x_7 & x_1 & x_2 & x_3 & x_4 \\ 0 & x_6 & x_7 & x_1 & x_2 & x_3 & x_4 & x_5 \\ 0 & x_7 & x_1 & x_2 & x_3 & x_4 & x_5 & x_6 \end{bmatrix} = BB' \tag{4.23}$$

The factorizations in Eq. (4.21) and Eq. (4.23) suggest the relationship between M and H and a mean for converting one into the other. Since B and L contain the same elements in different orders, such as S and B', we can define two permutation matrixes (P_L and P_S) which represent the new order of elements:

$$L = P_L B \qquad S = B' P_S \tag{4.24}$$

Therefore, the M matrix can be written as:

$$M = LS = P_L BB' P_S = P_L H P_S \tag{4.25}$$

The M-sequence transform, which allows to perform the deconvolution, can be done reordering the received data according to P_S, applying the Hadamard transform and reordering the transformed data according to P_L. The method described is summarized in the Fig. 90.

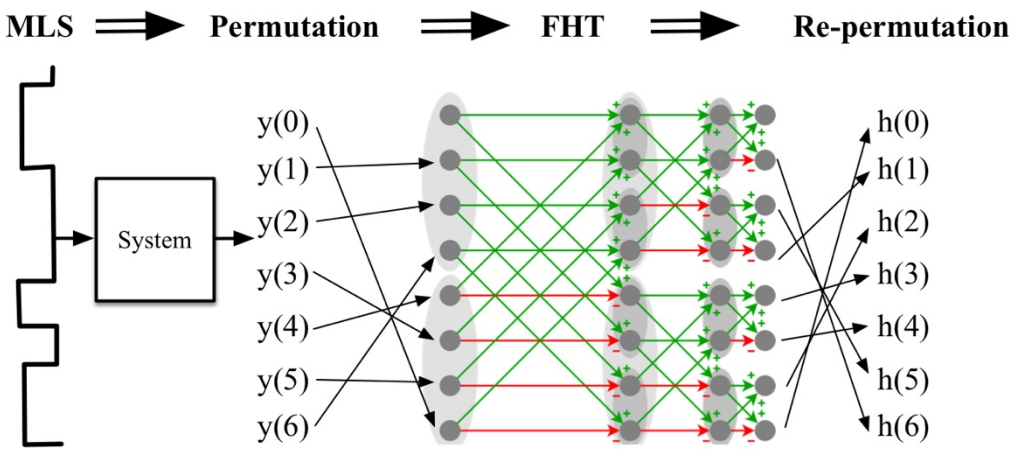

Fig. 90 Fast convolution with Hadamard Transform (FHT).

The big advantage of applying this algorithm is the clear reduction of the computational complexity from N^2 to $2.5N\log_2(N)$ [86], which means moving from 260 millions of operations to 573,401 with a reduction factor more than 450 (for N=14). As we can see in Fig. 90, the FHT involves only sums and subtractions and it can be represented using a butterfly scheme similar to the FFT, which will be described in the next section.

4.4.2 FFT

The Fourier Transform in discrete domain (DFT) can be performed reducing the computational complexity with the introduction of fast algorithms such as the Fast Fourier Transform (FFT). These algorithms are based on the mathematical ability to identify some common schemes, such as the butterfly one, in the formulation of the DFT [87]. Let us consider N discrete samples defined as $x[n]$ for $n=0,...,N-1$, the DFT is:

$$X[k]=\sum_{n=0}^{N-1} x[n]e^{-j\frac{2\pi kn}{N}},k=0,...,N-1 \tag{4.26}$$

Defining the trigonometric constant coefficient $W_N=e^{-j\frac{2\pi}{N}}$ as the twiddle factor [88], the Eq. (4.26) becomes:

$$X[k]=\sum_{n=0}^{N-1} x[n]W_N^{kn} \tag{4.27}$$

which, in matrix formulation, can be represented as:

$$X=\begin{bmatrix} 1 & 1 & \dots & 1 & 1 \\ 1 & W_N & W_N^2 & \dots & W_N^{(N-1)} \\ 1 & W_N^2 & W_N^4 & \dots & \dots \\ \dots & \dots & \dots & \dots & \dots \\ 1 & W_N^{(N-1)} & W_N^{2(N-1)} & \dots & W_N^{(N-1)(N-1)} \end{bmatrix} x \tag{4.28}$$

The above formulations clearly show that the number of complex multiplications involved are N^2.
The first method to reduce the complexity is based on a decimation in time (DIT) which involves $N\log(N)$ operations. The demonstration of this algorithm [89] relies on splitting even and odd terms in DFT definition:

$$X[k]=\sum_{n=0}^{N-1}x[n]e^{-j\frac{2\pi kn}{N}}=\sum_{m=0}^{N/2-1}x[2m]W_N^{k2m}+\sum_{m=0}^{N/2-1}x[2m+1]W_N^{k(2m+1)}\quad k=0,..,N-1 \tag{4.29}$$

where a change of variable is applied ($m=n/2$).
If we consider the first N/2 terms of the *X[k]*, the previous equation can be written, considering the equality $W_N^{2mk}=W_{N/2}^{mk}$, as:

$$X[k]=\underbrace{\sum_{m=0}^{N/2-1}x[2m]W_{N/2}^{mk}}_{DFT\ \substack{even\\terms}}+\underbrace{W_N^k\sum_{m=0}^{N/2-1}x[2m+1]W_{N/2}^{mk}}_{DFT\ \substack{odd\\terms}}\qquad k=0,..,N/2-1 \tag{4.30}$$

and the remaining N/2 outputs are:

$$X\left[k+\frac{N}{2}\right]=\sum_{m=0}^{N/2-1}x[2m]W_{N/2}^{m(k+N/2)}+W_N^{k+N/2}\sum_{m=0}^{N/2-1}x[2m+1]W_{N/2}^{m(k+N/2)}\quad k=0,..,\frac{N}{2}-1 \tag{4.31}$$

We can prove that the following equalities are valid:

$$\begin{aligned}W_{N/2}^{m(k+N/2)}&=W_{N/2}^{mN/2}W_{N/2}^{mk}=W_{N/2}^{mk}\\W_N^{k+N/2}&=W_N^{N/2}W_N^k=-W_N^k\end{aligned} \tag{4.32}$$

On the basis of these, the Eq. (4.31) becomes very similar to the first part (Eq. (4.30)) except for a minus sign:

$$X\left[k+\frac{N}{2}\right]=\sum_{m=0}^{N/2-1}x[2m]W_{N/2}^{mk}-W_N^k\sum_{m=0}^{N/2-1}x[2m+1]W_{N/2}^{mk} \tag{4.33}$$

The above discussion on the DIT FFT can be represented by a scheme involving one complex multiplication, sum and subtraction. Fig. 91 shows a scheme called "butterfly", for the shape of data-flow, with an 8-points DIT FFT.
The DIT is based on the grouping of the input terms; however, it is also possible to group even and odd terms of the output. In this specific case, the algorithm is called decimated in frequency (DIF) and the mathematical discussion can be found in reference [89] . Until now, we have assumed that the problem dimension is reduced of a factor equal to 2 at each stage of the FFT, which means that the scheme has a radix-2 decimation [91]. To furtherly reduce the complexity, we can express the DFT as the combination of 4 DFTs, whose dimension is ¼ of the original, called radix-4 decimation [92].
The comparison of the decomposition performances is shown in Fig. 92.

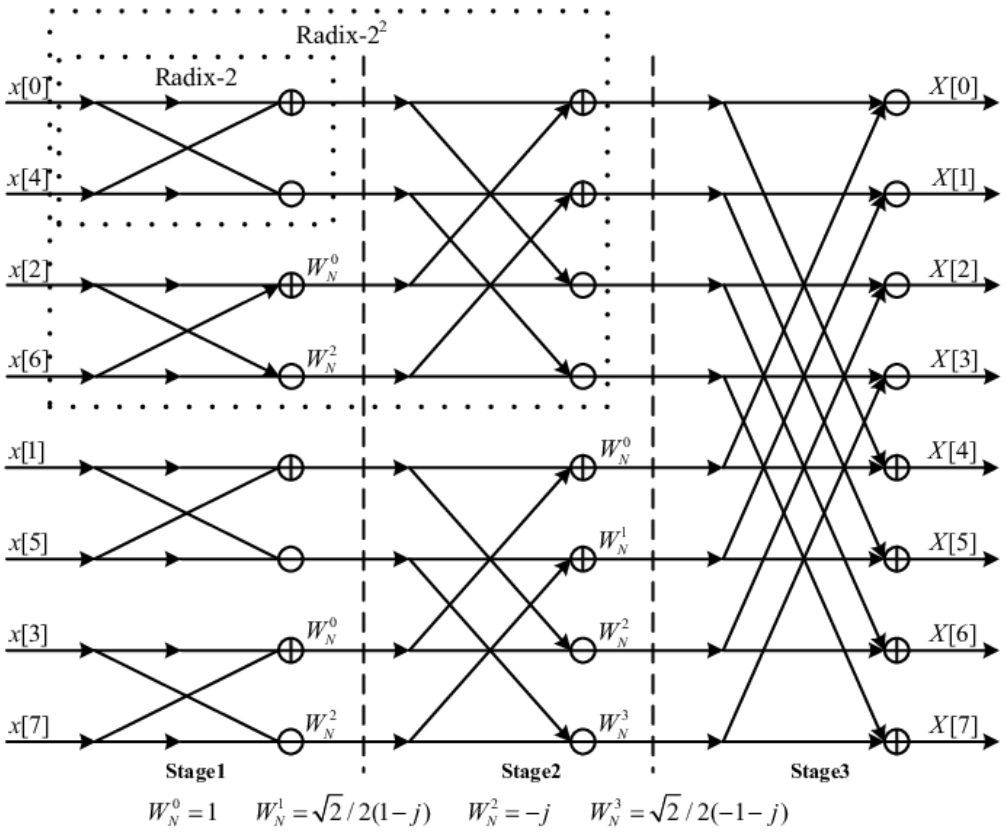

Fig. 91: Butterfly scheme for 8-points DIT FFT [90].

Radix-2 Decomposition		Radix-4 Decomposition	
Number of stages:	**log2N**	Number of stages:	**(log2N)/2**
Complex multiplication for a single stage:	**(N/2)log2N**	Complex multiplication for a single stage:	**(3N/8)log2N**
Complex sums for a single stage:	**Nlog2N**	Complex sums for a single stage:	**(3N/2)log2N**

Fig. 92: Computation complexity of radix-2 and radix-4 decimations.

4.5 Ultra-low power platform GAP8

The above algorithm implementations require a hardware platform able to boost the performance in term of energy efficiency. To achieve this target, we use the ultra-low power programmable platform GAP8, which originates from the PULP (Parallel Ultra Low Power Platform) project by a collaboration between the University of Bologna and the Eidgenössische Technische Hochshule (ETH) Zurich [93] [94].

4.5.1 Architecture

GAP8 stems from the need to wireless transmit a big amount of data related to the IoT sensor activities. The main idea is to lighten the transmission volume with a processing close to the sensor and entrusted to an ultra-low power MCU. The challenge of the chosen platform is, therefore, to perform Giga Operations per Seconds (GOPS) on a small battery power improving the sensor autonomy. GAP8 is a RISC-V based SoC (System on Chip) fabricated in TSMC 55nm LP CMOS technology [95]. The architecture, shown in Fig. 93, is developed around two main control units, which are a fabric controller (FC) and a core cluster.

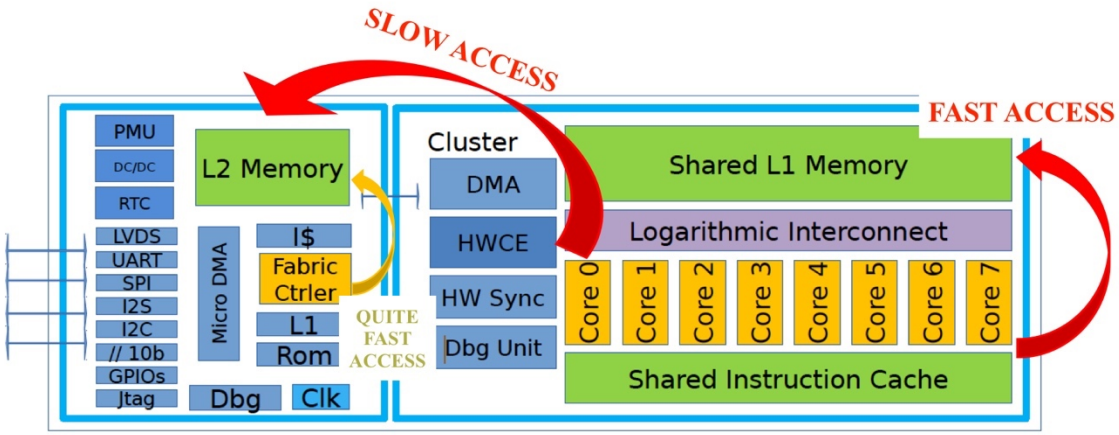

Fig. 93: Top-level view of the GAP8 architecture.

The FC is a single MCU with optimized performance in term of fast-access time data memory. With respect to the memory hierarchy, data can be stored in L1 and L2 (also an L3 can be introduced, which is external not shown in Fig. 93) memories. Typically, the access from a core is fast towards high-level memories (L1 is the highest), while the FC guarantees a fast access also for L2. On the other hand, the cluster contains 8 independent cores sharing the L1 and L2, but requiring more time to access the L2 compared to the FC. However, to reduce the interaction with the lowest level memory, a Direct Memory Access (DMA) is capable to hide the access cost while transferring 1D or 2D data [95]. The further advantage of the cluster relies on the possibility to parallelize an algorithm entrusting a workload portion to a every single core. This is possible

thanks to the shared memories and the shared instruction cache maximizing the algorithm efficiency. Moreover, the hardware block (HW Sync) improves the parallelism, allowing fast event management, parallel thread dispatching and synchronization.

The RISC-V architecture of the GAP8 authorizes the extension of the Instruction Set (ISA) to furtherly boost the performance of the platform. The GAP8 designers improved the DSP kernels, the manipulation of real/complex numbers as vectors of short data type and various array manipulations (multiplication and MAC instructions, rounding, normalization and clipping). The computational benefit is that most of these instructions are performed in a single-cycle. A set of Single Instruction Multiple Data (SIMS) are also added to manage groups of data collected in vectors (4-byte or 2-short elements). Other performed instructions are related to the bit-manipulation such as insertion, extraction and so on. Another strength of GAP8 is the possibility of running CNN-based applications using a dedicated Hardware Convolution Engine (HWCE) which evaluates a 5×5 or 3×3 convolutions (4,8 or 16-bit operands) in a single cycle.

All these data elaborations can be executed from data originating from a lot of peripherals embedded in the platform (SPI, UART, I2C, CAM and others).

The boosting speed up given by the implementation through GAP8 is proposed for the FFT algorithm (radix-4) with data at 15-fractional bit (Q15).

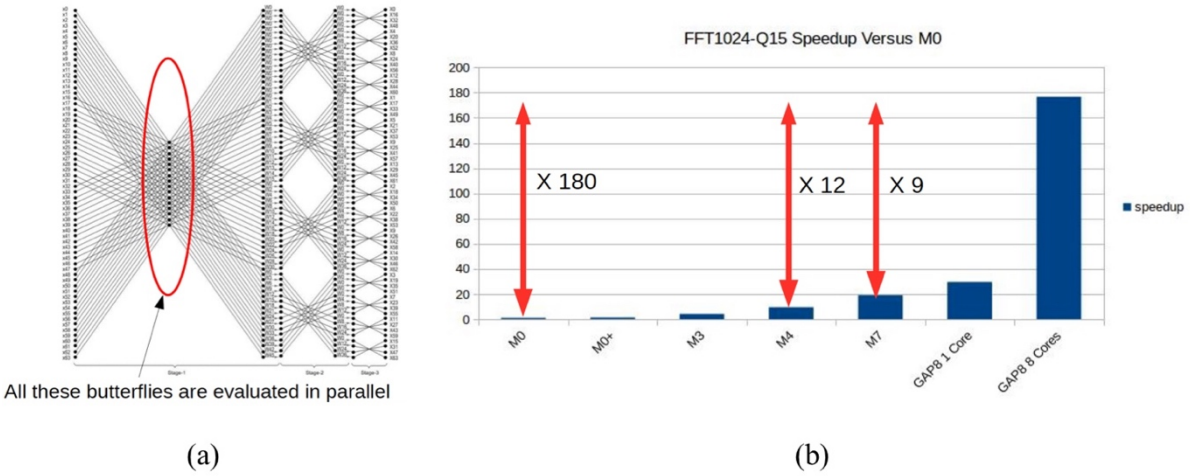

Fig. 94: Parallelization in the Butterfly scheme (a) and performance compared to the ARM-Cortex commercial products (M0, M0+, M3, M4, M7) in (b).

In Fig. 94 we can observe the parallelization applied (a) and the speedup compared to some ARM-Cortex products, where we can appreciate an improvement of the GAP8 speed-up up to 180 when all the 8 cores are employed. With these assumptions, GAP8 can deliver up to 10GMAC/s for CNN inference (90MHz, 1.0V) with an energy efficiency equals to 600 GMAC/s/W and a bad power consumption case of 75 mW.

4.5.2 GAPUINO board

We used GAP8 embedded in the board produced by Green Waves Technologies and known with the name of "GAPUINO" (for its compatibility with Arduino). The top-view is shown in the following figure:

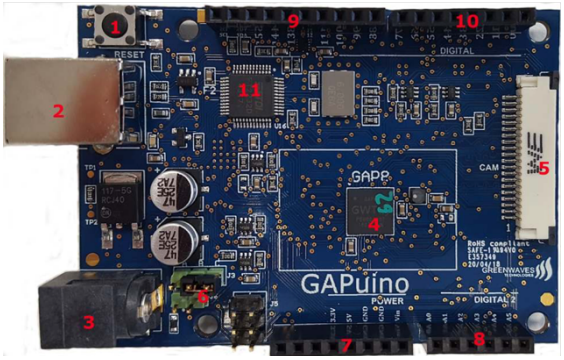

Fig. 95: Top view of GAPUINO board.

The GAP8 can be programmed thorough a USB-cable in C/C++ and OpenMP languages. A camera and a sensor board could also be connected to GAPUINO in order to enrich the measurements. The combination of all the boards available are shown in the picture.

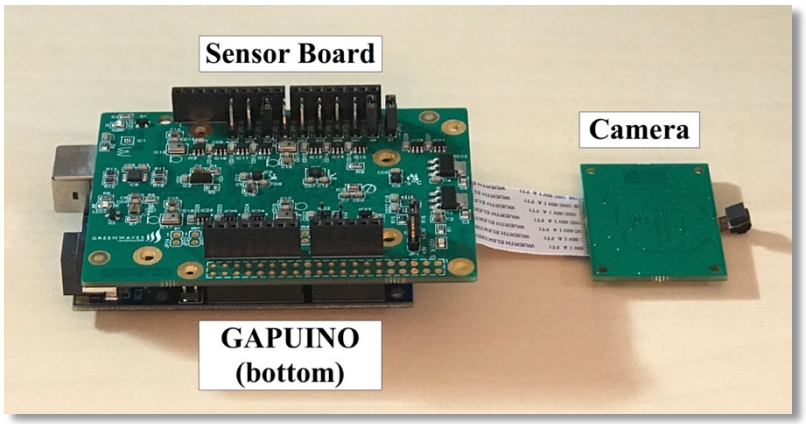

Fig. 96: Combination of GAPUINO and other boards available.

For a complete description of the boards we suggest visiting https://greenwaves-technologies.com.

4.5.3 Algorithm implementations

Starting from the time-domain implementation, the two main blocks (FHT and FFT) were implemented on GAP8 exploiting the platform potentialities and paying attention to the memory management. To obtain a wide and dense spectrum, we create an MLS of a length of $2^N - 1$ with $N = 14$, corresponding to 16,384 samples. Despite the MLS is binary, the only efficient storage way is using an 8-bit data type (*char*) for each MLS bit. Although it may seem a waste of resources, the char type is the smallest structure available in term of memory size while other ways to storage, for example storing 8 bits in one structure and then extracting them bitwise, requires too many computations. Moreover, GAP8 offers 512kB in L2, therefore, it can be widely used and then the DMA can be exploited to manage data into the L1 memory, allowing the computations. In L2 we can be also store the output $\bar{y}_n$ of the ADC in the system (Fig. 84) which is quantized even with 8 bits, considered enough for a good impulse response reconstruction. We need also to consider that the FHT result, which is the same result of the convolution, might assume very high values, when many samples are involved, and, therefore, forcing to employ a wider data-type up to 32 bits. The previously described FHT is implemented through two permutations and the application of the Hadamard scheme. The FHT uses N/2 stages when a Radix-4 scheme is employed as in [96]. On the basis of this, each stage was furtherly unrolled in two consecutive loop blocks to lighten the contentions due to the consecutive memory access to the same variable. An example of the implementation stages with N=4 is shown in Fig. 97.

For each stage of the scheme, the necessary data are moved from L2 to L1, through DMA, so as to minimize the transfers and fully occupy the memory space in L1 (maximum 64kB). This strategy is applied also for permutations. Since the GAP8 architectures, offers up to 8 cores working in parallel, we can parallelize the scheme in Fig. 97. However, the continuous memory accesses to the same variables involve many stalls due to all the cores, therefore, we verified that using only one core is the most efficient way to implement the convolution operation.

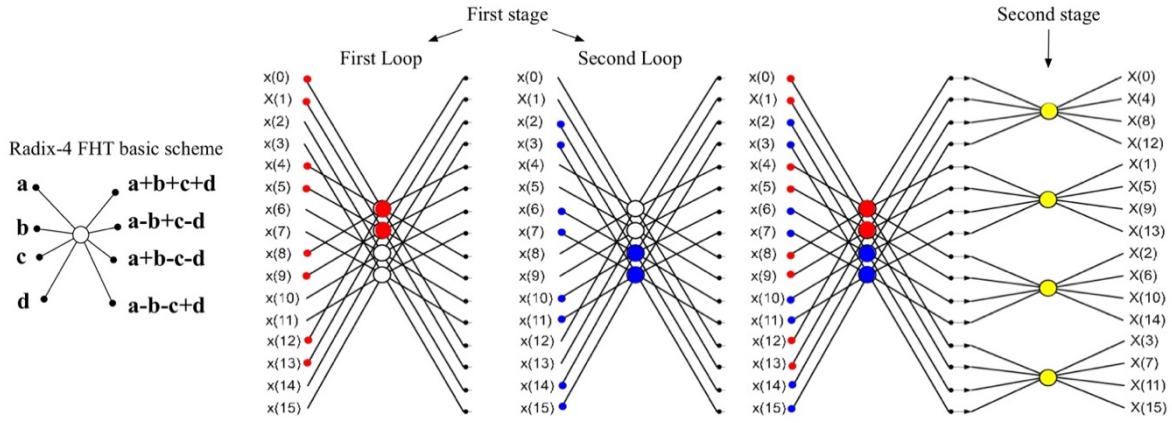

Fig. 97: Hadamard transform implementation for 16 samples.

Moreover, we can consider that the residual 7 cores available can be committed with other tasks for other computations or measurements. We need to clarify that the efficiency in the algorithm implementation is

measured by the number of cycles, necessary to perform the task, which should match the number of instructions. All the unmatched cycles can be due to stalls in loading/storing variables or related to the core synchronization and so on, therefore the goal of any good implementation is to minimize the mismatch instructions/cycles. Following this guideline, the optimized algorithm produced is shown in Fig. 98.

In the flowchart, we can appreciate that the main block includes two permutations and the FHT scheme as described in Fig. 90. We can note also that after the first permutation, the vector is padded with one element in order to have a 2^N length, necessary to apply the FHT; moreover, the FHT contains a quantization block to reduce the data size from 32 bit to 16 bit. This strategy is performed in the last stage of FHT to reduce the computation in the maximum research and its utility is related to the application of the FFT requiring 16-bit data type. Both the permutation and the FHT involve some blocks for reading data. This task is necessary since, as previously described, data are typically stored in L2 and moved in L1 using the DMA. This memory management is performed with respect to the reduced capability in L1 (64 kB) compared to L2 (512 kB).

On the other side, the FFT is implemented with a DIT Radix-2 scheme, where the twiddle factors are stored in L2 as a look-up table to correctly reorder the output after the "butterfly" scheme application, as we can observe in Fig. 91. Storing 16,384 twiddles and 16,384 elements of the look up table with a 16-bit data type is an excess of memory for the L1. Most common FFT libraries, however, need all these factors available at each FFT stage, meaning that they need to be stored in L2 and the core works fetching variables directly there. Such operations involve a lot of memory contentions since we cannot move to L1 with the DMA. For this reason, we can decide to entrust the FFT to the fabric controller which is faster in accessing L2 compared to a cluster core. The output of the algorithm is a complex vector containing real and imaginary parts of the complex impedance in a frequency domain.

On the other hand, the frequency-domain algorithm involves the FFT computation, a multiplication for a constant factor and a phase subtraction. The technique shown in time-domain algorithm to extract the frequency information can be maintained using the fabric controller to speed up the memory access in L2. The same controller is also employed for the multiplication and the phase subtraction between sequences of length 16,384 elements. These last two elaborations are computationally negligible compared with the FFT processing.

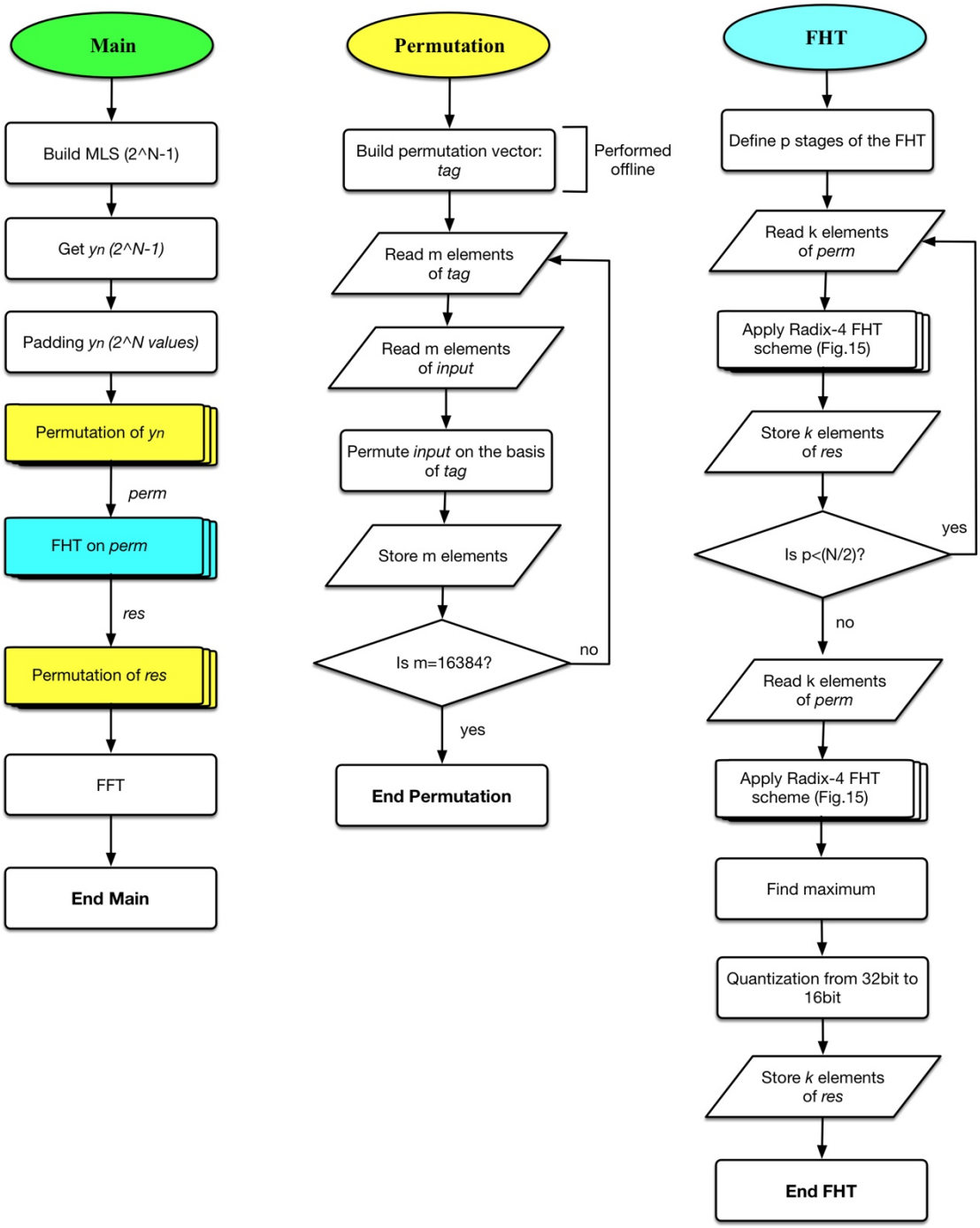

Fig. 98: Flowchart of the time-convolution convolution algorithm with FHT.

4.5.4 Results and performance

Before testing the algorithms on GAPUINO, the GAP8 distributor offers the possibility of simulating the algorithm behaviour in a virtual platform and in an FPGA (ZC706 Xilinx Zynq-7000) which acts as the GAP8. These preliminary tests help to understand and prevent problems referring to the algorithm implementation, especially for stalls and missed synchronizations. Moreover, the FPGA allows the communication through peripherals with the analog world connecting with a device under test. For this reason, we preliminary chose to evaluate the transfer function of an RC circuit as DUT. This test was performed using the time-domain algorithm with FFT included since the frequency-domain approach does not add further complexity. To interface these passive components with the FPGA, we used a commercial microcontroller (PIC24FJ64GC006) in particular for sampling data (ADC) and communicating with standard protocols (SPI). The connection between the FPGA with the microcontroller board is shown in the Fig. 99. The working flow consists in the FPGA sending the MLS sequence, through the SPI protocol (SDO signal), which crosses the RC circuit. The produced voltage drop is observed in the RC circuit output and sampled by the ADC embedded into the PIC24 and then transmitted as SDI to the FPGA which collects data and performs the elaboration.
Since this test is focused on the correct working of the algorithm, we can simply test the transfer function (TF) and not the impedance spectrum, which would have required a further block for current-to-voltage conversion. For an RC circuit assembled with passive components R=348 kΩ and C=47 nF, the transfer function is:

$$H(s) = \frac{64}{s+64} \tag{4.34}$$

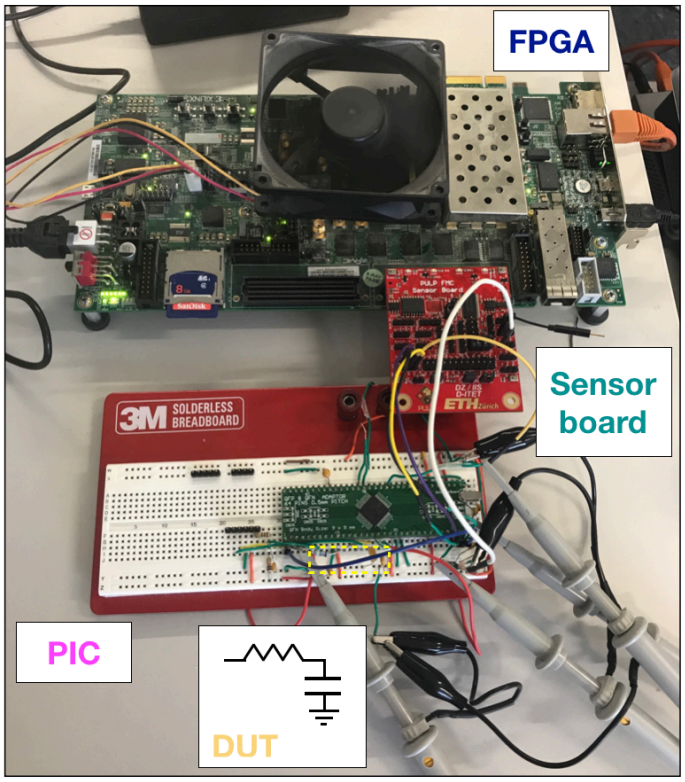

Fig. 99: FPGA with PIC24 board for extracting the transfer function of an RC circuit.

We assume that the we want to construct a spectrum of 8,192 points, exciting the RC circuit up to 1.5 kHz which seems reasonable considering that the cut-off frequency of the RC circuit is around 10 Hz.
The result obtained with GAP8, compared with the ideal TF (Fig. 100), shows a faithful behaviour to the ideal one with high accuracy especially for low frequencies.

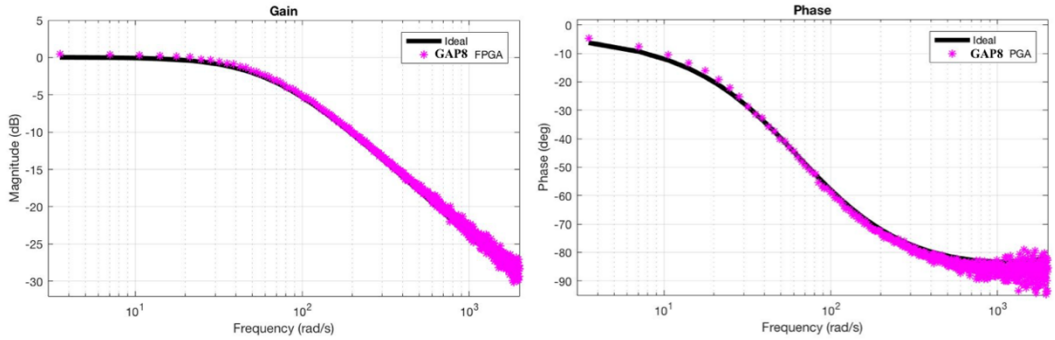

Fig. 100: FPGA results testing the TF of an RC circuit.

The value of the estimated TF at the cut-off frequency (calculated as the magnitude decay at 3 dB) differs from the ideal one by a factor of 10 %. If we compare this result with the one obtained in simulation, although for another circuit (Fig. 88), we can say that we reach a high accuracy taking into consideration that we are testing an RC circuit assembled with passive components in the real world where further noise sources can contribute.
Moving into the GAPUINO platform, the first tests were executed in time-domain storing all the data necessary to the algorithm working into the memory, bypassing the analog interactions with the real world. A very high accuracy in the impedance estimation is reached also with this board, as shown in Fig. 101 where the impedance in time is obtained with bit frequency at 3 MHz by applying the Hadamard Transform to the previously described RLC circuit with the following TF: $\frac{5 \cdot 10^{11}}{s^2 + 2.5 \cdot 10^5 s + 5 \cdot 10^{11}}$.

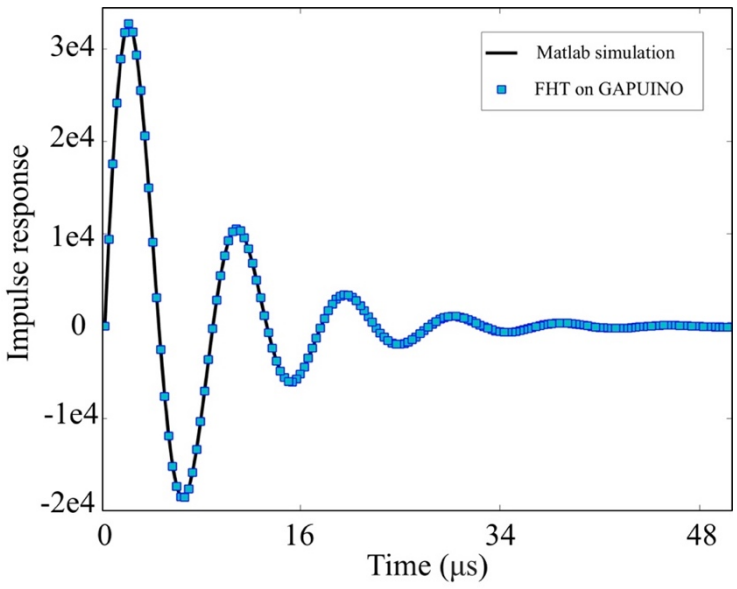

Fig. 101: Impedance in time obtained by GAP8 using GAPUINO (time-domain algorithm).

The simulation curve and the one obtained with GAPUINO are exactly the same, since the FHT does not change the convolution results but only lightens the computation.

Moving into the frequency-domain algorithm, the FFT application in Fig. 102 shows a slight decrease in the accuracy specially at low frequencies due to a rounding of values given by the FFT implementation chosen. However, this is a systematic error which can be easily compensated.

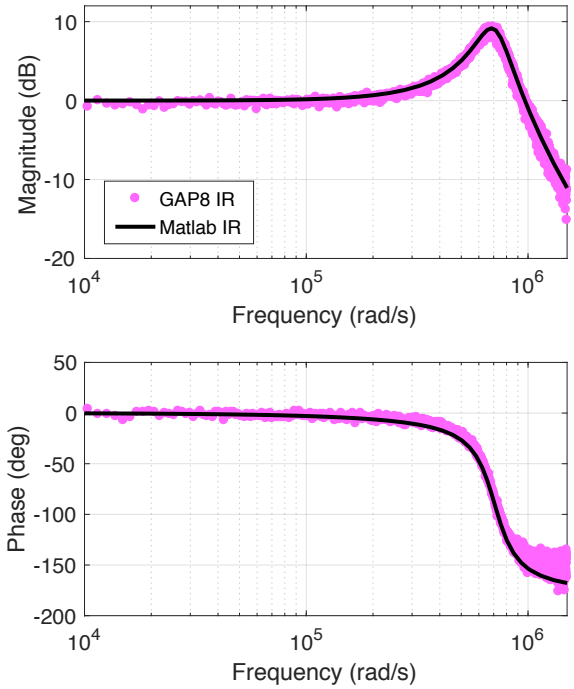

Fig. 102: Impedance in frequency obtained by GAP8 using GAPUINO (frequency-domain algorithm).

Despite the slight accuracy reduction, the estimation of the RLC parameters is very well reconstructed with an error $\%err_{\zeta}$ equal to 5 % and $\%err_{\omega_n}$ equal to 2%.

The successful reconstructions of the desired information are strengthened by the excellent performance in term of algorithm efficiency and power consumptions. The comparison between the two algorithms is described in term of number of instructions and cycles which reflect on the power consumption and the processing time.

By assuming 16,384 samples, the convolution and the FFT, which are the main elaborations for respectively time and frequency domain, involve the theoretical number of operations described in (4.35)

$$\begin{aligned} &Convolution: 16{,}384\,MAC \times 16{,}384 shift = 268{,}402{,}689\,MAC = 2.6e8\,MAC \\ &FFT: 16{,}384 \log_2(16{,}384) = 229{,}376 = 2.2e5op \end{aligned} \tag{4.35}$$

where MAC is a multiply-accumulator operation. The application of the Hadamard transform for the convolution in time, further reduces the instructions into:

$$2.5 \log_2 16{,}384 = 573{,}440 = 5.7e5op \tag{4.36}$$

When these operations are implemented in GAP8, other instructions are intrinsically added associated with the loading/storing variables, memory management and so on. This increases not only the number of instructions but also the number of cycles that the architecture requires to perform a specific task. By assuming

the frequency algorithm performed by the fabric controller (FC) and the time-domain executed by one core belonging to the cluster, Fig. 103 shows cycles and instructions involved.

	#Cycles	#Instructions	
Perm1	154347	100334	Cluster core
FHT	10342333	6352380	Cluster core
Perm2	111691	65818	Cluster core
FFT	2755616	783414	FC

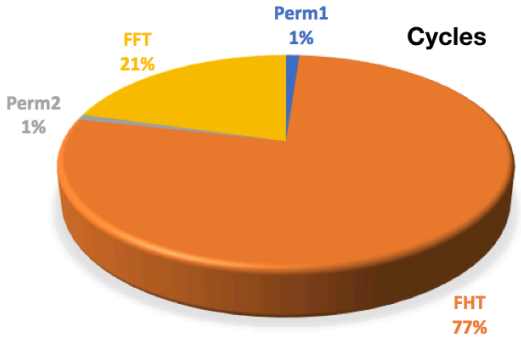

	#Instructions	#Cycles
TOTAL Cluster Core	6518532=6.5e6	10608371=1e7
TOTAL Fabric Controller	783414=7.8e5	2755616=2.7e6

Fig. 103: Number of cycles and instructions involved in the algorithm implementation.

We can observe that the FHT fills the 77% of the entire computational budget, especially compared to the FFT. However, the number of cycles for the convolution operation (Perm1+FHT+Perm2) is around 10 millions, which is significantly lower than the theoretical number in Eq. (4.35). From these values, processing time can be evaluated depending on the core working frequency, while the power consumption can be measured through the current consumption on GAP8 into the GAPUINO board. We should take into consideration that the time domain exploits one core of the cluster which is always enabled, while the frequency approach uses only the FC. This means that, although the cluster allows parallel measurements the consumption is higher than the use of the single FC. However, this was the only reasonable strategy to manage a big amount of data.

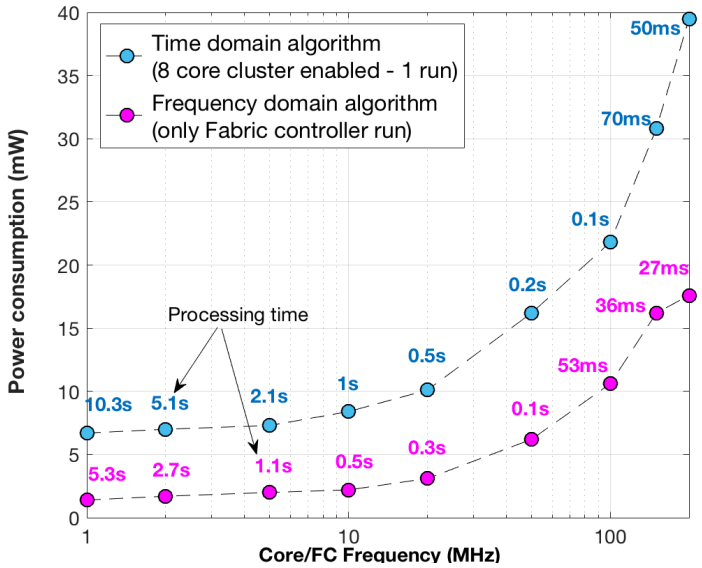

Fig. 104: Power consumption and processing time for time and frequency domain algorithms.

Fig. 104 shows an increasing behaviour of the power consumptions for both algorithms while increasing the core frequencies. At 200 MHz, the frequency implementation consumes only 17.6 mW respect to 40 mW of the time-domain while the elaboration can be performed, respectively, in 27 ms and 50 ms. When the processing time is not relevant, the entire impedance extraction (at 1 MHz) can be obtained with a power consumption of only 1.4 mW in time and 6.4 mW in frequency.
Observing Fig. 104, we can find a trade-off between the maximum consumption requested and the fastness of the measurement desired which depends on the time variability of the device under test.

4.5.5 Analog interface for GAPUINO

Observing the block scheme in Fig. 84, it emerges that the response requires an interaction with the analog world. However, for testing the working of the algorithm, such response was simulated offline in Matlab and then stored in the GAP8 memory bypassing the analog interface. Taking now this interaction in consideration, we also have to consider that the device under test is stimulated in voltage and the corresponding response is in current, so also a current-to-voltage conversion is necessary. This requirement forces to modify the scheme in Fig. 84 adding an I/V converter (Fig. 105), which was not previously considered since not necessary for testing only the correct working of the algorithm.

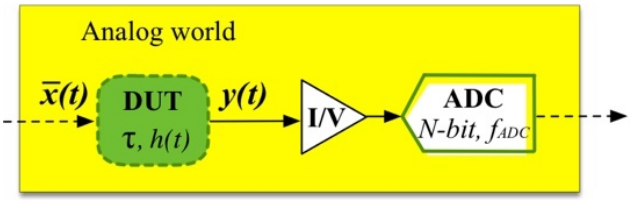

Fig. 105: Modification of the impedance measurement system (Fig. 84) with current-to-voltage block.

Since a possible application of the described system is a wearable device, the low-power requirement is maintained also for the research of the I/V and ADC blocks. Other specifications should refer to the specific application of this wearable sensor; however, for a general case we can consider that the DUT will be excited up to 1MHz. Such frequency respectively value influences the bandwidth of the I/V and the sampling frequency of the ADC. For these reasons, the I/V proposed is the AD8066 (Analog Devices) with a wide bandwidth up to 145MHz and a power consumption of 64mW. On the other hand, the ADC employed is an 8-bit low power ADC (LTC1406 by Linear Technology) where the output is given by a parallel bus and consuming 150mW. This analog interface, still under development, is made up by the converter and the ADC should be integrated in a PCB connected between GAPUINO and the DUT. In particular the connection with the device under test should guarantee the correct excitation and the response reading, typically performed with electrodes.

4.6 Electrodes for wearable applications

If we consider the application of an impedance-based device with low-power consumption, it can be applied in a lot of fields, for example in wearable technology to investigate some parameters from the skin. In this perspective the implementation described perfectly matches the request but suitable flexible electrodes for the measurement are necessary. In the standard impedance measurement, only two electrodes are necessary, respectively, refers to the voltage and current quantities as shown in Fig. 106.

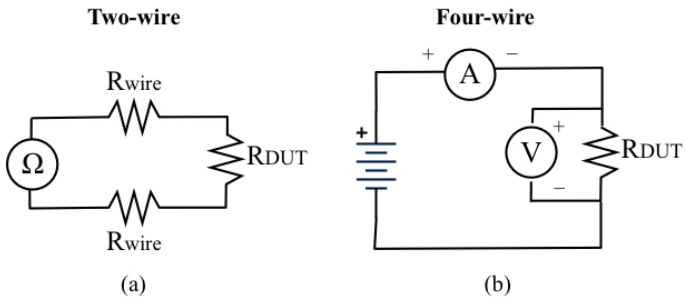

Fig. 106: Methods for impedance measurement using two or four wires.

The two-wire method has the drawback of taking into consideration the resistances of both the wires while evaluating the R_{DUT}. This could be injurious if the DUT resistance is much smaller than the wires. To overcome this problem, it is possible to use a 4-wire configuration, where one pair is associated with the voltage stimulation and the other pair closes the current loop crossing the device. Finding commercial electrodes for wearable applications is not a simple research because they are typically manufactured specifically for the device and the application. For these reasons, the only choice is to adapt commercial electrodes used in other fields and combine them for the wearable technology. In connection with this problem, we started the research toward two-wire electrodes with characteristics of miniaturization and suppleness. We selected a range of printable electrodes (by GSI Technologies) on paper support with gold ink and protected by a polymeric film differing for dimensions and shapes. A different type of electrodes was also tested which is an interdigitated in gold with a glass support distributed by Micrux. Eight samples of electrodes were collected in Fig. 107.

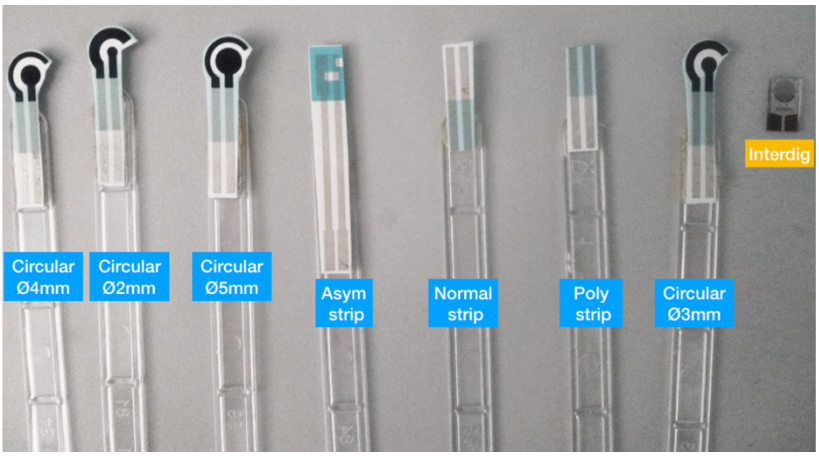

Fig. 107: Samples of electrodes chosen for wearable application.

The circular samples differ for the size of their diameters, while the strips have asymmetric bars (Asym strip) or symmetric polymerized bars (Poly strip) and not (Normal strip); the interdigitated on glass support is represented on the right side of Fig. 107 (Interdig). These electrodes are subjected to three tests in order to evaluate their impedance behaviour when applied to a saline solution at 0.9% NaCl (Test1), a solution reproducing the sweat composition (Test2) and a long-term test for monitoring the status of electrodes up to 5 days. The impedance is evaluated in absolute and phase values spread into a frequency range of 20Hz-2MHz using the precision LCR meter (E4980A by Agilent). Absolute values collected from the complex impedance (Fig. 108) show a decreasing behaviour along the frequency axis becoming asymptotic at high frequencies. Observing the error bars in Fig. 108, we can appreciate that the circular samples have lower standard deviations, while the bars have a small displacement in amplitude, that is optimal since we want a minimum interference of the electrodes while measuring the saline solution impedance, which covers the rule of a resistance (constant modulus) . The same conclusions can be inferred from the phase plot where the behaviour increases from negative values to zero. The entire behaviours of absolute and phase reflect a capacitive impedance which can be represented with an open-circuit for low frequencies and a short circuit for high ones. This can be also observed in the Cole-Cole plot in Fig. 110 (a) and in the zoom in Fig. 110(b) studied for the Poly strip electrode.

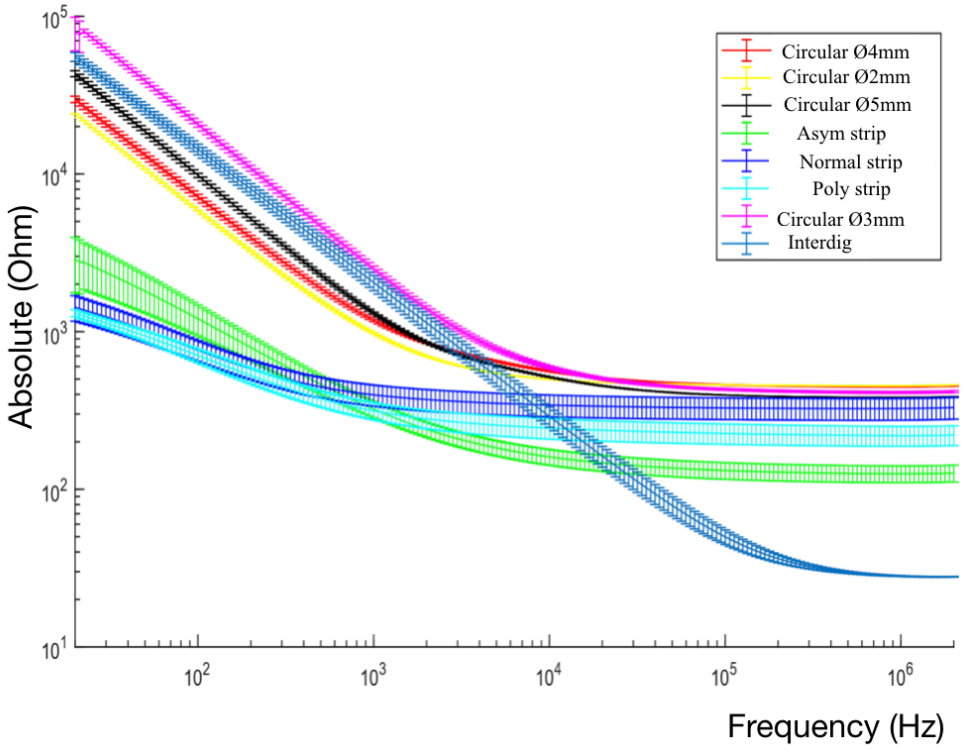

Fig. 108: Absolute values of electrodes into a saline solution obtained with sine waves (amplitude 50mV) in 20Hz-2MHz range.

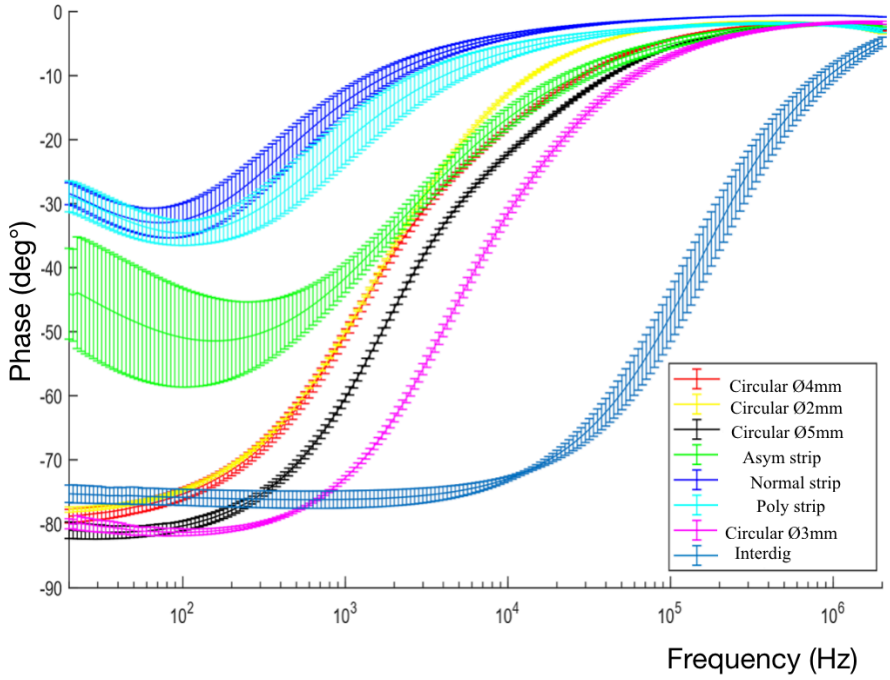

Fig. 109: Phase values of electrodes on a saline solution obtained with sine waves (amplitude 50mV) in 20Hz-2MHz range.

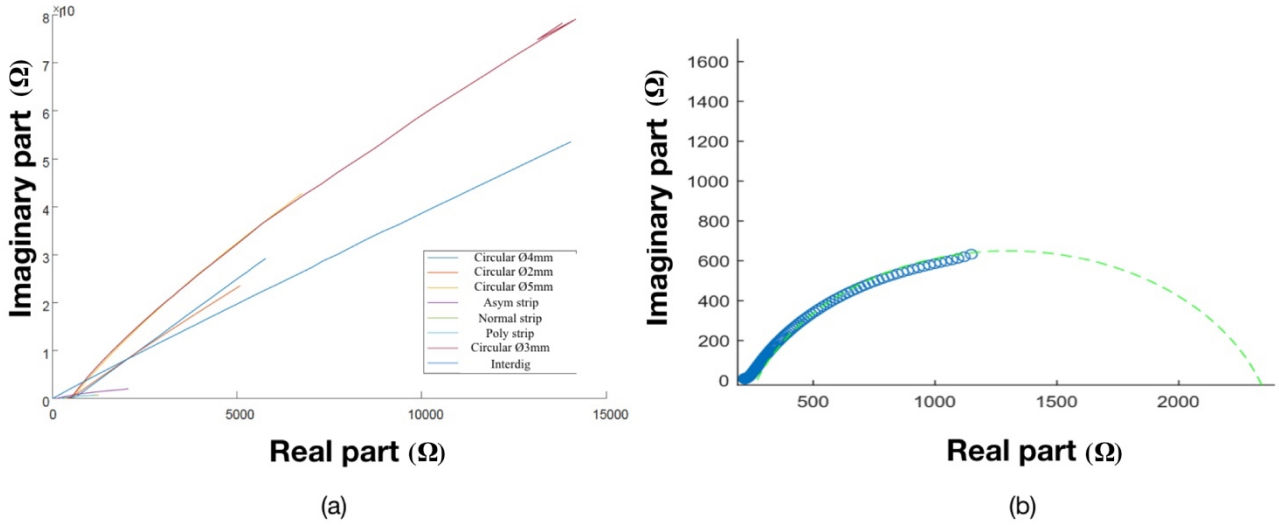

Fig. 110: Cole-Cole plot for all samples (a) and zoom at high frequencies (b) for Poly strip electrode.

Since these wearable electrodes could be also applied for monitoring the sweat transpired from the skin, further tests are performed dipping the electrodes into the solution reproducing the artificial sweat. Following the European standard EN1811:2012 and neglecting urea and lactate components, artificial sweat can be reproduced using potassium chloride (NaCl), sodium chloride (KCl) and deionized water. Five samples were made with different concentrations of solvent and solute (Fig. 111) which correspond to a different conductivity of the sample. The behaviour of the electrodes under testing these solutions shows a clear identification of the different samples where the absolute value decreases with the increasing of the molar concentration (Fig. 111). The same conclusions can be drawn also for the phase. The following figure represents the behaviour for the circular electrode with 2mm diameter, but the same conclusion can be observed for the other samples.

Another interesting test, common in the scientific community to assess long-term characterization of the electrodes, is to leave them immersed in a saline solution and to analyse the impedance trend during time up to 5 days. The results obtained testing our samples in the saline solution (0.9% NaCl) are reported for the circular sample (2mm) producing the best result. From Fig. 112 we can see that the absolute value in time tends to decrease but we consider the mismatch reasonable since no precautions for thermal insultations have been taken.

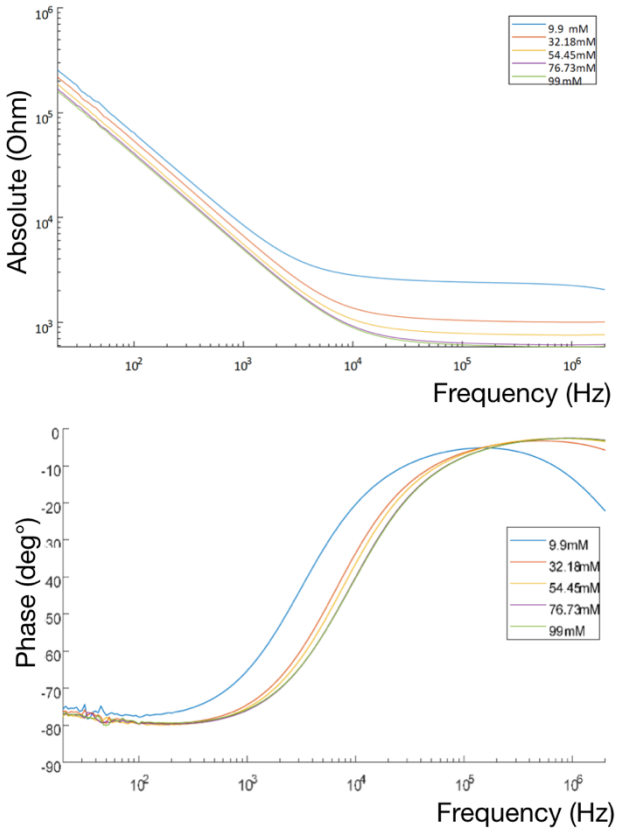

Sample	Solution Vol (mL)	Solute Vol (mL)	Solvent Vol (mL)	Molar Concentration (mM)
1	50	5	45	9.9
2	50	16.25	33.75	32.18
3	50	27.50	22.50	54.45
4	50	38.75	11.25	76.73
5	50	50	0	99

Fig. 111: Absolute and Phase of circular electrode (2mm) in contact with sweat solution samples.

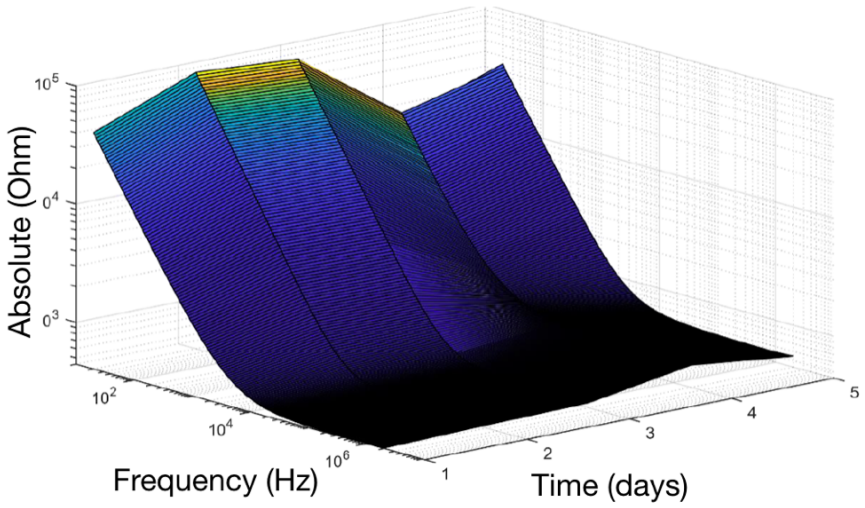

Fig. 112: Long-term characterization of circular electrode with 2mm diameter.

4.7 Examples of target application

In the perspective of wearable applications, the IS systems shown above can be useful in investigating some properties of the skin or to check the electrode/skin interface in portable systems [105]. Commercial devices based on impedance spectroscopy are developed to extract information about the skin hydration level [17] or sweat ion and metabolites concentration[19] mainly during fitness activity where real-time monitoring and wearability are mandatory. In medical word, the IS technique can be employed to appreciate differences between healthy and damaged tissues also due to the presence of cancer cells. Following the Schwan study [15] in fact, is possible to investigate the anomalies in cell morphology by selecting a specific frequency range (1 kHz – 100 MHz) as described in Section 1.1.

Considering the skin as the tissue under test, Aberg et al. [11] choose the range between 1 kHz and 1 MHz to detect the presence of a specific cancer skin in nevi known as basal cell carcinoma (BCC). The differences in impedance for both absolute value and phase amount to various orders of magnitude as shown in Fig. 113.

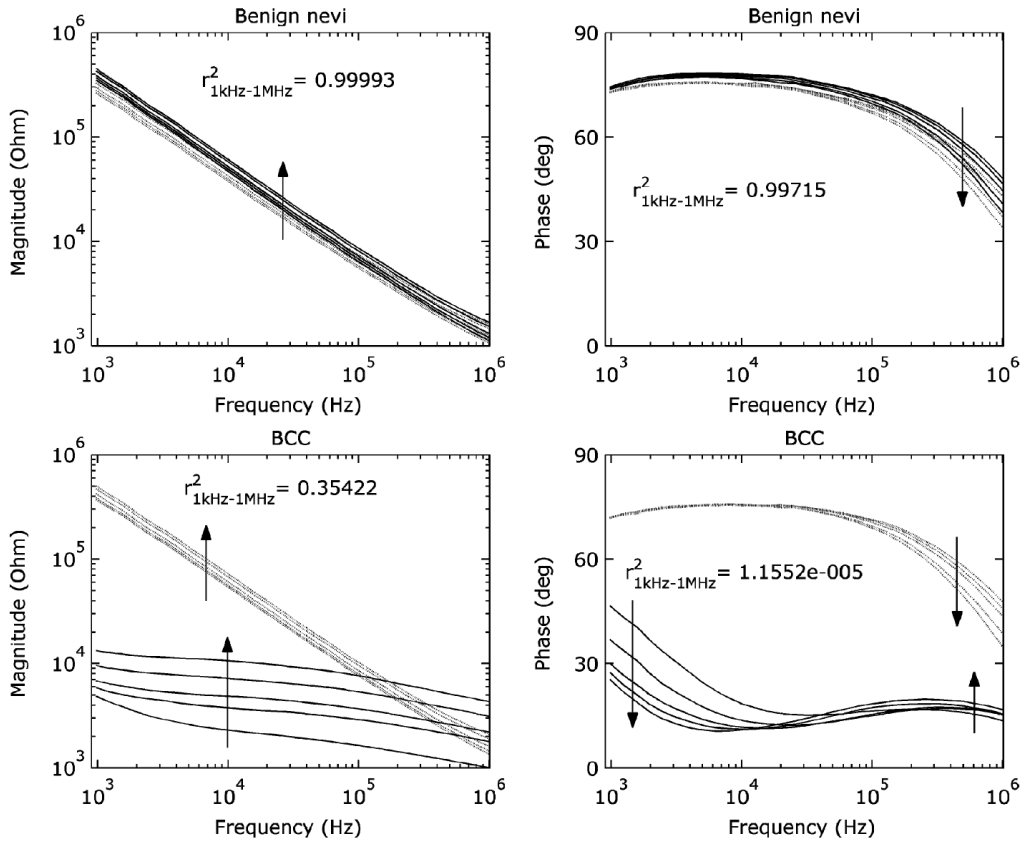

Fig. 113: Impedance spectra for benign nevi and BCC [15].

The systems developed with GAP8 can be therefore good candidates to detect the presence of such cancer skin since they benefit from high accuracy and wide range of frequencies for example employing MLS of 16,384 samples. The wearable systems proposed can be interesting during the monitoring of these suspicion nevi before the diagnosis or in the follow-up action specially after the surgical removal of the cancer when the possibility of relapse is high.

4.8 Project relevance for thesis topic

The described project is proposed as a new technique implemented in an ultra-low-power architecture where strategies are applied to reduce the algorithm complexity. Therefore, the new direction for the IS topic focuses on the research of techniques for reducing the power consumptions of the system, involving the research of a suitable excitation, impedance processing and the implementation on platform. The contribution of the signal is due to the binary nature of the PRBS which allows to exploit all the potentialities of the digital architecture. The two elaborations proposed, based on the FHT and FFT, still offer a further way for optimizing the power resources which are already reduced if the GAPUINO platform is employed. The results obtained by this implementation are excellent reconstructions both in time and frequency domain (Fig. 101 and Fig. 102). However, the amazing achievement is given by the reconstruction of an impedance spectrum of 16,384 frequency points with high accuracy ($\%err_\zeta$ equal to 3.3%) while the GAP8, embedded in the board, consumes only 1.4 mW.

All these efforts converge into the design of a wearable sensor, still under development. In this application, the higher consumptions are mainly related to the analog blocks, such as I/V converter and the ADC which, anyway, can be chosen with the right power performances as shown. Towards the wearable implementation, also miniaturized and flexible electrodes are studied, in order to complete the system description. In conclusion, possible target applications are described for the wearable system developed. In addition to common applications for fitness purposes, the IS can be employed for skin cancer detection making the developed system a wearable sensor with diagnostic purposes.

Conclusions

This thesis outlines the need of the emerging sensors to revisit the impedance spectroscopy technique in order to extract accurate measurements together with low power consumptions. The focus was the study and the design of three IS-based devices which, respectively, indicate new strategies to:

- reach high accurate measurements;
- draw an augmented information on impedance spectrum;
- implement IS systems with reduced power consumptions.

These directions can be combined together to boost the performance of IS-based sensors becoming very promising in a lot of applications, especially in the biomedical field.

A miniaturized vector analyser interfaced with multiple impedance-based sensors (temperature, conductivity, heart valve tracking) is the offered solution to achieve very accurate impedances up to 0.15 % as a non-linearity error for the absolute value and 0.07 ° (excitation at 1 kHz) for the phase. The system is a coupling between a microcontroller and an academical ASIC, whose accuracy is around 166 ppm. A statistical characterization has been conducted on the developed vector analyser showing that the high accuracy, mainly due to the ASIC architecture, is almost preserved by some implementation strategies applied to the entire system. Furthermore, the final resolution of the vector analyser is estimated at 13.8 bits higher than similar commercial devices.

Meanwhile, two soil moisture sensors have been manufactured and combined with powerful statistical tools for improving the prediction of the water content among different types of soil. Both sensors share the same architecture which relies on a mismatch between transmitting and receiving electromagnetic excitations on a soil. The integration of linear and non-linear models (PCA, PLS, N-PLS, K-OPLS) enable us to augment the information desired spread into a collection of spectrum points. The comparison between the observed moisture content and predicted ones successfully reaches an R^2 value of 0.991 and an RMSE equal to 0.9 % , when an N-PLS model, combining together the absolute and phase values, is applied for the LECA sample. The moisture sensors developed represent an innovation also for the portability of the systems which can be employed in precision agriculture as sensor nodes.

A further study was conducted to research and implement IS techniques at low power consumptions, paving the way for emerging applications in the IoT context, such as smart devices. An almost digital approach, based on a PRBS excitation has been included in an ultra-low power platform for being integrated in a wearable device, still under development. Some strategies applied on the algorithm implementation produces a power consumption of about 1.4 mW to cover a dense spectrum of 16,384 frequency points. In the near future, this device will be applied for non-invasive impedance measurements on skin in order to deduct the health status of a subject.

Further developments among IS systems, will involve the applications of all these directions in the design of a new smart sensors, where the power strategies will extend their lifetime and the augmented information, together with accuracy, will make them well-suitable for a lot of applications.

Bibliography

[1] W. Nerst, Methode zur bestimmung von dielektrizitatskonstanten, Zeitschrijtfur, 14 (1894), 622-663.

[2] E.P. Randviir and C.E. Banks, Electrochemical impedance spectroscopy: an overview of bioanalytical applications, Analytical Methods, 5(5) (2013), 1098-1115.

[3] T. Fusayama, T. Katayori and S. Nomoto, Corrosion of gold and amalgam placed in contact with each other, Journal of Dental Research, 42(5) (1963), 1183-1197.

[4] D. Xue, Z. Tan, M.J. Schulz, W.J. Vanooij, J. Sankar, Y. Yun and Z. Dong, Corrosion studies of modified organosilane coated magnesium–yttrium alloy in different environments, Materials Science and Engineering: C, 32(5) (2012), 1230-1236.

[5] P. Yang, Q. Zheng, H. Xu, J. Liu and L. Jin, L., A Highly Sensitive Electrochemical Impedance Spectroscopy Immunosensor for Determination of 1-Pyrenebutyric Acid Based on the Bifunctionality of Nafion/Gold Nanoparticles Composite Electrode, Chinese Journal of Chemistry, 30 (5) (2012), 1155-1162.

[6] L. Wang, J. Zhao, X. He, J. Gao, J. Li, C. Wan and C. Jiang, Electrochemical impedance spectroscopy (EIS) study of LiNi1/3Co1/3Mn1/3O2 for Li-ion batteries, Int. J. Electrochem. Sci, 7(1) (2012), 345-353.

[7] L. Hlavata, K. Benikova, V. Vyskocil and J. Labuda, Evaluation of damage to DNA induced by UV-C radiation and chemical agents using electrochemical biosensor based on low molecular weight DNA and screen-printed carbon electrode, Electrochimica Acta, 71 (2012), 134-139.

[8]. N. S. Mathebula, J. Pillay, G. Toschi, J.A. Verschoor and K. Ozoemena, Recognition of anti-mycolic acid antibody at self-assembled mycolic acid antigens on a gold electrode: a potential impedimetric immunosensing platform for active tuberculosis, Chemical Communications 23 (2009), 3345-3347.

[9] R. Singh, Z. Matharu, A.K. Srivastava, S. Sood, R.K. Gupta, and B.D. Malhotra, Nanostructured platform for the detection of Neisseria gonorrhoeae using electrochemical impedance spectroscopy and differential pulse voltammetry, Microchimica Acta, 177(1-2).

[10] J.P. Metters, R.O. Kadara and C. Banks, New directions in screen printed electroanalytical sensors: an overview of recent developments, Analyst, 136(6) (2011), 1067-1076.

[11] P. Aberg, I. Nicander, J. Hansson, P. Geladi, U. Holmgren and S. Ollmar, Skin cancer identification using multifrequency electrical impedance-a potential screening tool, IEEE transactions on biomedical engineering, 51(12) (2004), 2097-2102.

[12] R.J Halter, A. Schned, J. Heaney, A. Hartov, S. Schutz and K.D. Paulsen, Electrical impedance spectroscopy of benign and malignant prostatic tissues, The Journal of urology, 179(4) (2008), 1580-1586.

[13] J.E. Da Silva, J.M. De Sá and J. Jossinet, Classification of breast tissue by electrical impedance spectroscopy, Medical and Biological Engineering and Computing, 38(1) (2000), 26-30.

[14] V. Cherepenin, A. Karpov, A. Korjenevsky, V. Kornienko, A. Mazaletskaya, D. Mazourov and D. Meister, A 3D electrical impedance tomography (EIT) system for breast cancer detection, Physiological measurement, 22(1) (2001), 9.

[15] H.P. Schwan, Electrical properties of tissue and cell suspensions, Advances in biological and medical physics, 5 (1957), 147-209.

[16] W.J. Hannan, S.J Cowen, K.C.H Fearson, C.E. Plester, J.S. Falconer and R.A. Richardson, Evaluation of multifrequency bioimpedance analysis for the assessment of extracellular and total body water in surgical patients, Clin. Sci., 86 (1994), 479– 485.

[17] X. Huang, W.H. Yeo, Y. Liu and J. A. Rogers, Epidermal differential impedance sensor for conformal skin hydration monitoring, Biointerphases, 7(1-4) (2012), 52.

[18] M. Ulbrich, M. Czaplik, A. Pohl, M. Zink and S. Leonhardt, Estimation of blood alcohol content with bioimpedance spectroscopy, Int. Workshop on Impedance Spectroscopy, 138 (2013).

[19] W. Gao, S. Emaminejad, HYY. Nyein, et al., Fully integrated wearable sensor arrays for multiplexed in situ perspiration analysis, Nature, 529(7587) (2016), pp. 509-514.

[20] D. Sankhala, S. Muthukumar and S. Prasad, A Wearable Electrochemical Impedance Spectroscopy Device for Detection of Glucose in Sweat Using Zinc Oxide Based Flexible Biosensors, The electrochemical society 42 (2018), 2439-2439.

[21] H. Kõiv, M. Rist and M. Min, Development of bioimpedance sensing device for wearable monitoring of the aortic blood pressure curve, tm-Technisches Messen, 85(5) (2018), 366-377.

[22] S.L. Swisher et al., Impedance sensing device enables early detection of pressure ulcers in vivo, Nature communications, 6 (2015), ncomms7575.

[23] S. Rodriguez, S. Ollmar, M. Waqar and A. Rusu, A batteryless sensor ASIC for implantable bio-impedance applications, IEEE transactions on biomedical circuits and systems, 10(3) (2016), 533-544.

[24] B. Zhou, C. Bian, J. Tong, S. Xia, Fabrication of a Miniature Multi-Parameter Sensor Chip for Water Quality Assessment, Sensors (Basel) 17 (2017), 157.

[25] M. Carminati, P. Luzzatto-Fegiz, Conduino: Affordable and high-resolution multichannel water conductivity sensor using micro USB connectors, Sensors Actuators, B Chem. 251 (2017) 1034–1041.

[26] M.H. Banna, H. Najjaran, R. Sadiq, S.A. Imran, M.J. Rodriguez, M. Hoorfar, Miniaturized water quality monitoring pH and conductivity sensors, Sensors Actuators B Chem. 193 (2014) 434–441.

[27] A. Hyldgård, D. Mortensen, K. Birkelund, O. Hansen, E.V. Thomsen, Autonomous multi-sensor micro-system for measurement of ocean water salinity, Sensors Actuators A Phys. 147 (2008) 474–484.

[28] F.R. Harker and S.K. Forbes, Ripening and development of chilling injury in persimmon fruit: an electrical impedance study, New Zeal. J. Crop Hort., 25 (1997), 149–157.

[29] L. Ragni, E. Iaccheri, C. Cevoli, A. Berardinelli, A. Bendini and T.Gallina Toschi, A capacitive technique to assess water content in extra virgin olive oils, J. Food Eng., 116 (2013), 246–252.

[30] M.F. Mabrook, A.M. Darbyshire and M.C. Petty, Quality control of dairy products using single frequency admittance measurements. Measurement Science and Technology, 17(2) (2005), 275.

[31] R. Masot et al, Design of a low-cost non-destructive system for punctual measurements of salt levels in food products using impedance spectroscopy, Sensors and Actuators A: Physical, 158(2), 217-223.

[32] R. Kumar, R.J. Weber and G. Pandey, U.S. Patent Application No. 10/073,074 (2018).

[33] D.M. Pozar, Microwave engineering, John Wiley & Sons (2009).

[34] J.R. Macdonald and W.B. Johnson, Fundamentals of Impedance Spectroscopy, in: Impedance Spectroscopy (eds E. Barsoukov and J. R. Macdonald), 2005.

[35] E.T. McAdams, A. Lackermeier, J.A. McLaughlin, D. Macken and J. Jossinet, The linear and non-linear electrical properties of the electrode-electrolyte interface, Biosensors and Bioelectronics, 10(1-2) (1995), 67-74.

[36] A. B. Carlson, Communication system, Tata McGraw-Hill Education, 2010.

[37] I.F. Akyildiz, W. Su, Y. Sankarasubramaniam and E. Cayirci, Wireless sensor networks: a survey, Computer networks, 38(4) (2002), 393-422.

[38] M. Crescentini, M. Bennati and M. Tartagni, A High Resolution Interface for Kelvin Impedance Sensing. J. Solid-State Circuits, 49(10) (2014), 2199-2212.

[39] S. Pavan, R. Schreier and G.C. Temes, Understanding delta-sigma data converters, John Wiley & Sons (2017).

[40] ISX-3mini-Sciospec, http://www.sciospec.de/product/isx-3mini/, 2018 (accessed 24 October 2018).

[41] SinePhase, https://sinephase.com/impedance-analyzer-model-16777k-lcr-meter7, 2018 (accessed 24 October 2018).

[42] Aceabio, https://www.aceabio.com/products/icelligence, 2018 (accessed 24 October 2018).

[43] S. Brosel-Oliu, N. Uria, N. Abramova, and B. Andrey. Impedimetric sensors for bacteria detection, Biosensor-Micro and Nano Application, (2015).

[44] E. Marcelli, University of Bologna, 'Heart valve prosthesis with integrated circuit for measuring intravalvular electrical impedance, and system for monitoring functionality of the prosthesis', WO2015/158789A1 (PCT/EP2015/058201), 2014.

[45] Soil Survey Staff, Soil survey manual, Soil Conservation Service U.S.Department of Agriculture Handbook, 18, 1993.

[46] M. Bittelli, Measuring soil water content: a review, Horttechnology 21 (2011)293–300.

[47] S.L. S.U., D.N. Singh, M. Shojaei Baghini,;1 A critical review of soil moisturemeasurement, Measurement 54 (2014) 92-105.

[48] G. Luciani, A. Berardinelli, M. Crescentini, A. Romani, M. Tartagni and L. Ragni, Non-invasive soil moisture sensing based on open-ended waveguide and multivariate analysis, Sensors and Actuators A: Physical 265 (2017) 236-245.

[49] D.S. Chanasyk, M.A. Naeth, Field measurement of soil moisture using neutronprobe, Can. J. Soil Sci. 76 (1996) 317–323.

[50] F.S. Zazueta, J. Xin, Soil Moisture Sensors, Florida Cooperative ExtensionService, Bulletin 292, Inst. Food and Agricultural Sciences, University ofFlorida, Gainesville, 1994.

[51] A. Chanzy, A. Tarussov, A. Judge, F. Bonn, Soil water content determinationusing a digital ground-penetrating radar, Soil Sci. Soc. Am. J. 60 (1996)1318–1326.

[52] V.S. Palaparthy, M.S. Baghini, D.N. Singh, Review of polymer-based sensors foragriculture-related applications, Emerg. Mater. Res. 2 (2013) 166–180, EMR4.

[53] S. Sreedeep, A.C. Reshma, D.N. Singh, Measuring soil electrical resistivity usinga resistivity box and a resistivity probe, ASTM, International, WestConshohocken, PA, 2004, pp. 19428–22959.

[54] K. Noborio, K.J. McInnes, J.L. Heilman, Measurement of soil water content,heat capacity, and thermal conductivity with a single TDR probe, Soil Sci 161(1996) 22–28.

[55] R.A. Viscarra Rossel, D.J.J. Walvoort, A.B. McBratney, L.J. Janik, J.O. Skjemstad,Visible, near infrared, mid infrared or combined diffuse reflectancespectroscopy for simultaneous assessment of various soil properties,Geoderma 131 (2006) 59–75.

[56] A. Morellos, X.-E. Pantazi, D. Moshou, T. Alexandridis, R. Whetton, G. Tziotzios,J. Wiebensohn, R. Bill, A.M. Mouazen, Machine learning based prediction ofsoil total nitrogen, organic carbon and moisture content by using VIS-NIRspectroscopy, Biosyst. Eng. 152 (2016) 104–116.

[57] F. Demontoux, S. Razafindratsima, S. Bircher, G. Ruffié, F. Bonnaudin, F. Jonard,J.P. Wigneron, M. Sbartaï, Y. Kerr, Efficiency of end effect probes for in-situpermittivity measurements in the 0.5-6 GHz frequency range and theirapplication for organic soil horizons study, Sensors and Actuators journal: A.Physical 254 (2017) 78–88.

[58] F. Demontoux, B. Le Crom, G. Ruffié, J.P. Wigneron, J.P. Grant, V.L. Mironov, H.Lawrence, Electromagnetic characterization of soil-litter media: applicationto the simulation of the microwave emissivity of the ground surface in forests,The European Physical Journal-Applied Physics 44 (3) (2008) 303–315.

[59] G.C. Topp, S. Zegelin, I. White, Impact of real and imaginary components ofrelative permittivity on time domain reflectometry measurements in soil, SoilSci. Soc. Am. J. 64 (2000) 1244–1252.

[60] N. Romano, Soil moisture at local scale: measurements and simulations, J.Hydrol. 516 (2014) 6–20.

[61] J. Cihlar, F.T. Ulaby, Dielectric properties of soils as a function of moisturecontent, Kansas Univ. Center for Research, Inc, 1974, NASA-CR-141868.

[62] K. Noborio, Measurement of soil water content and electrical conductivity bytime domain reflectometry: a review, Comput. Electron. Agric. 31 (2001), 213–237.

[63] D.A. Robinson, S.B. Jones, J.M. Wraith, D. Or, S.P. Friedman, A review ofadvances in dielectric and electrical conductivity measurement in soils usingtime domain reflectometry, Vadose Zone J. 2 (2003), 444–475.

[64] Patent n. International application n. PCT/IB2015/050246, pubblication n. WO/2015/107455 A1, Analyzer of materials by micorwave spectroscopy.

[65] http://www.analog.com/media/en/technical-documentation/data-sheets/AD8302.pdf. [Online]

[66] R. Bro and A. K. Smilde, Principal component analysis, Analytical Methods, 2014, 6(9), 2812-2831.

[67] S. Wold, K. Esbensen and P. Geladi, Principal component analysis, Chemometrics and intelligent laboratory systems, 2.1-3 (1987): 37-52.

[68] A. A. Christy, S. Kasemsumran, Y. Du and Y. OZAKI, The detection and quantification of adulteration in olive oil by near-infrared spectroscopy and chemometrics. Analytical Sciences, 20(6) (2004), 935-940.

[69] A. Berardinelli, C. Cevoli, F.A. Silaghi, A. Fabbri, L. Ragni, A. Giunchi and D. Bassi, FT-NIR Spectroscopy for the Quality Characterization of Apricots (Prunus Armeniaca L.). Journal of food science, 75(7) (2010), E462-E468.

[70] S. Wold, M. Sjöström, L. Eriksson, PLS-regression: a basic tool ofchemometrics, Chemometr. Intell. Lab. Syst 58 (2) (2001), 109–130.

[71] R. Bro, Multiway calibration. Multi-linear PLS, J.Chemom. 10 (1996), 47–61.

[72] S. Wold, N. Kettaneh-Wold and B. Skagerberg, Non-linear PLS Modelling. Chemometrics and Int. Lab. Syst., 7 (1989), 53-65.

[73] G. Baffi, E.B. Martin and A. J. Morris, Non-linear projection to latent structures revisited: the quadratic PLS algorithm. Computers & Chemical Engineering, 23(3) (1999), 395-411.

[74] I.E. Frank, A Non-linear PLS Model, Chemometrics and Int. Lab. Syst., 8(1990),109-119.

[75] S. Wold, Non-linear Partial Least Squares Modelling II. Spline Inner Function, Chemometrics and Int. Lab. Syst., 14 (1992), 71-84.

[76] G. Cybenko, Approximation by Superpositions of a Sigmoidal Function, SIAM J. Sci. Stat. Comput. 5 (1989), 175-191.

[77] M. Wang, G.Yan and Z. Fei, Kernel PLS based prediction model construction and simulation on theoretical cases, Neurocomputing, 165 (2015), 389-394.

[78] J. Trygg and S. Wold, Orthogonal projections to latent structures (O-PLS), J. Chemometrics, 16 (2002), 119-128.

[79] M. Bylesjö, M. Rantalainen, J.K. Nicholson, E. Holmes and J. Trygg, K-OPLS package: kernel-based orthogonal projections to latent structures for prediction and interpretation in feature space, BMC bioinformatics, 9(1) (2008), 106.

[80] C.A. Andersson, R. Bro, The N-way Toolbox for MATLAB, Chemometr. Intell.Lab. Syst. 52 (2000) 1-4.

[81] A. Berardinelli, G. Luciani, M. Crescentini, A. Romani, M. Tartagni and L. Ragni, Application of non-linear statistical tools to a novel microwave dipole antenna moisture soil sensor, Sensors and Actuators A: Physical, 282 (2018), 1-8.

[82] D. V. Sarwate and M. B. Pursley, "Crosscorrelation properties of pseudorandom and related sequences", Proceedings of the IEEE, 68(5), 593-619, 1980.

[83] S. Gawad, T. Sun, N. G. Green and H. Morgan, "Impedance spectroscopy using maximum length sequences: Application to single cell analysis", Rev. Sci. Instr., vol. 78(5) (2007), 054301.

[84] M. Vilkko and T. Roinila, "Designing maximum length sequence signal for frequency response measurement of switched mode converters," Nordic Workshop on Power and Industrial Electronics (NORPIE/2008), Espoo, Finland. Helsinki University of Technology, 2008.

[85] M. Cohn and A. Lempel, On fast M-sequence transforms, IEEE Transactions on Information Theory, 23(1) (1977), 135-137.

[86] J. Borish and J.B. Angell, An efficient algorithm for measuring the impulse response using pseudorandom noise, Journal of the Audio Engineering Society, 31(7/8) (1983), 478-488.

[87] D.F. Elliott and K.R. Rao, Fast transforms algorithms, analyses, applications, Elsevier, 1983.

[88] T.D. Chiueh and P.Y. Tsai, OFDM baseband receiver design for wireless communications, John Wiley & Sons, 2008.

[89] K.R. Rao, D.N. Kim and J.J. Hwang, Fast Fourier transform-algorithms and applications, Springer Science & Business Media, 2011.

[90] H. Xiao, A. Pan, Y. Chen and X. Zeng, Low-cost reconfigurable VLSI architecture for fast fourier transform, IEEE Transactions on Consumer Electronics, 54(4) (2008).

[91] J. W. Cooley and J.W. Tukey, An algorithm for the machine calculation of complex Fourier series, Mathematics of computation, 19(90) (1965), 297-301.

[92] D.L. Jones, Radix-4 FFT Algorithms, Connexions module: m12027, 2006.

[93] D. Rossi et al., PULP: A parallel ultra low power platform for next generation IoT applications, Hot Chips 27 Symposium (HCS), IEEE 2015.

[94] F. Conti et al, An IoT endpoint system-on-chip for secure and energy-efficient near-sensor analytics, IEEE Transactions on Circuits and Systems I, 64.9 (2017), 2481-2494.

[95] E. Flamand et al, GAP-8: A RISC-V SoC for AI at the Edge of the IoT, 2018 IEEE 29th International Conference on Application-specific Systems, Architectures and Processors (ASAP). IEEE, 2018.

[96] M. Drutarovsky and D. Kocur, Optimization of fast hadamard deconvolution implementation for ARM CPU based M-sequence UWB radar sensor node, Progress in Electromagnetics Research Symposium-Fall (PIERS-FALL), (2017), 1288-1294.

[97] C. Gabrielli, Identification of electrochemical processes by frequency response analysis, Solartron Instrumentation Group, 1980.

[98] G. Bonmassar, S. Iwaki, G. Goldmakher, L.M. Angelone, J.W Belliveauand M.H. Lev, On the measurement of electrical impedance spectroscopy (EIS) of the human head, International journal of bioelectromagnetism, 12(1) (2010), 32.

[99] M. Grossi and B. Riccò, Electrical impedance spectroscopy (EIS) for biological analysis and food characterization: a review, Journal of Sensors and Sensor Systems, 6 (2016), 303-325.

[100] A. Tetyuev, O. Kanoun and H.R. Trankler, Soil type characterization for moisture measurement by impedance spectroscopy, Instrumentation and Measurement Technology Conference Proceedings of the IEEE (2006), 735-740.

[101] R. Kumar, R.J. Weber and G. Pandey, U.S. Patent Application No. 10/073,074 (2018).

[102] M. Bariya, H.Y. Nyein and A. Javey, Wearable sweat sensors, Nature Electronics, 1(3) (2018), 160.

[103] F.A. Firestone, A new analogy between mechanical and electrical systems, The Journal of the Acoustical Society of America, 4(3) (1933), 249-267.

[104] F. Maloberti, Data Converters. Dordrecht, The Netherlands: Springer, (2007).

[105] Cometa Systems, https://www.cometasystems.com/technologies, 2018 (accessed 6 February 2018)